

# **A Predictive Thermal Model of Heat Transfer in a Fiber Optic Bundle for a Hybrid Solar Lighting System**

by

Michael Cheadle

A thesis submitted in partial fulfillment of  
the requirements for the degree of

Master of Science  
(Mechanical Engineering)

at the

UNIVERSITY OF WISCONSIN-MADISON

2005



Approved by

---

Professor Gregory F. Nellis

---

Date



# Abstract

Hybrid lighting systems distribute natural sunlight to luminaires in office or other retail buildings in order to provide natural lighting that can impact employee productivity, morale, and even sales. In some situations, these systems may also result in a significant reduction in energy consumption by reducing both the lighting energy and the cooling load that is associated with conventional lighting systems. A key component of a hybrid lighting system is the fiber optic bundle (FOB) that transmits the light from the collector to the luminaire. The FOB consists of many small plastic optical fibers in a close-packed array. The thermal failure of these FOBs when exposed to concentrated sunlight has motivated the development of a thermal model that can be used to understand the behavior of these systems. Thermal management is necessary due to the concentrated incident solar radiation on the face of the fiber optic bundle and the low melting point temperature of the plastic optical fiber.

A predictive thermal model of heat transfer in a fiber optic bundle for a hybrid solar lighting system has been developed in order to better understand and manage the thermal loading associated with the concentrated solar radiation on the face of the FOB. Experiments were carried out on an instrumented FOB section exposed to illumination energy in a controlled environment. The experimental results provide information regarding the characteristics of the thermal loads that result from the radiation that is incident on the pores between the fibers as well as the effective, anisotropic thermal conductivity associated with the complex structure that makes up the FOB. It was found that the radiation incident on the FOB face contributed to the thermal loading in two ways: radiation incident on the face of the plastic fibers contributed a low level of volumetric generation within the FOB related to the transmission loss while

radiation incident on the air gaps between plastic fibers contributed a volumetric generation concentrated near the face of the FOB.

The experimental results were used to specify the thermal loads and equivalent parameters required for a more detailed, multidimensional finite element model (FEM) of the FOB and its support structure. This FEM is used to understand the transient behavior of the FOB and evaluate alternative thermal management strategies.



## Acknowledgements

To my advisors Greg Nellis, Sandy Klein and Bill Beckman, thank you for your continued support on this project. The creative and challenging working environment you created for me was tremendously appreciated.

Thanks also to Dan Hoch, Duncan Earl and Scott Sanders for their technical assistance.

The research in this thesis would not have been possible without the support of the Hybrid Solar Lighting partnership. In particular I would like to thank the University of Nevada Reno, Oak Ridge National Laboratory and The United States Department of Energy for their technical and financial assistance.

Finally, thanks to my loving family for their enduring support.

# Table of Contents

<b>Abstract.....</b>	<b>i</b>
<b>Acknowledgements.....</b>	<b>iv</b>
<b>Table of Contents .....</b>	<b>v</b>
<b>List of Figures.....</b>	<b>vii</b>
<b>List of Tables .....</b>	<b>ix</b>
<b>Nomenclature.....</b>	<b>x</b>

## Chapter 1

<b>Introduction to Hybrid Solar Lighting.....</b>	<b>1</b>
1.1 Hybrid Solar Lighting Overview .....	1
1.1.1 Components of the Hybrid Solar Lighting System.....	1
1.1.2 Motivations for HSL Systems.....	2
1.2 Literature Review of Hybrid Solar Lighting.....	5
1.3 Goals and Motivation for Current Research .....	5
1.4 Previous Fiber Optic Bundle Model .....	7
1.5 Conclusion .....	9

## Chapter 2

<b>One-Dimensional Model .....</b>	<b>10</b>
2.2 Fiber Optic Bundle Geometry.....	10
2.2.1 Fiber materials and properties.....	10
2.2.2 Fiber optic bundle and packing factor .....	11
2.4 Analytical Derivation of 1-D Model.....	17
2.5.1 Calculating Porosity.....	24
2.5.2 Effective Axial Conductivity .....	27
2.5.3 Effective Heat Transfer Coefficients .....	28
2.5.4 Source Heat Flux.....	30
2.6 Parametric Studies .....	47
2.7 Conclusions.....	51

## Chapter 3

<b>Experimental Setup.....</b>	<b>52</b>
3.2 Experimental Setup at Oak Ridge National Laboratory .....	52
3.2.1 Experimental design.....	52
3.3 Experimental Setup at the University of Wisconsin-Madison.....	60

## Chapter 4

<b>Two-Dimensional Model.....</b>	<b>73</b>
4.2 Additions and Modifications to the 1-D Analytical Model .....	74
4.2.1 Porosity as a function of radial position for the experimental FOB .....	74
4.2.2 Radially dependent heat generation for the experimental FOB .....	76
4.2.3 Radially dependent equivalent conductivities for the experimental FOB .....	78
4.3 ANSYS Results for Experimental FOB.....	79
4.4 ANSYS Results for On-Sun FOB.....	82
4.5 Conclusions.....	89

## Chapter 5

<b>Thermally Managed Fiber Optic Bundle Configurations .....</b>	<b>90</b>
5.2 Thermal Management Strategies .....	90
5.2.1 Design considerations .....	90
5.2.2 Single copper rod .....	91
5.2.3 Aluminum filled pores .....	93
5.3 Experimental FOB with Copper Wire in Pores .....	95
5.4 Conclusions.....	99

## Chapter 6

<b>Recommendations and Conclusions .....</b>	<b>100</b>
6.1 Recommendations for future work .....	100
6.2 Summary .....	101

## References .....

## Appendix .....

EES Code .....	105
Calculation of Effective Axial Conductivity .....	105
Calculation of Effective Radial Conductivity.....	105
Calculation of Front, Rear Face and Edge Heat Transfer Coefficients .....	106
Calculation of the Characteristic Length Associated with the Pores .....	108
1-D Model Temperature Predictions within the Experimental FOB .....	109
MATLAB Code .....	110
Calculation of Porosity and Heat Generation .....	110
ANSYS Code .....	112
2-D Model Temperature Predictions within the Experimental FOB .....	112
2-D Model Temperature Predictions within the On-Sun FOB .....	117
2-D Model Temperature Predictions within the Copper Rod FOB .....	127
2-D Model Temperature Predictions within the Aluminum Filled FOB .....	136

# List of Figures

## Chapter 1

<b>Fig. 1.1</b> Schematic of an HSL system.....	2
<b>Fig. 1.2</b> Collector within an HSL system .....	2
<b>Fig. 1.3</b> Delivered commercial energy consumption.....	4
<b>Fig. 1.4</b> Electrical energy consumption in commercial buildings .....	4

## Chapter 2

<b>Fig. 2.1</b> End of a plastic fiber optic cable .....	11
<b>Fig. 2.2</b> Cylindrical array of optical fibers packed together to form a FOB.....	12
<b>Fig. 2.3</b> Packing factor for an ideal FOB.....	13
<b>Fig. 2.4</b> Cylindrical fiber optic rods ideally packed into a cylindrical collet .....	13
<b>Fig. 2.5</b> The face of an experimental FOB .....	14
<b>Fig. 2.6</b> Radiation incident on the FOB face .....	16
<b>Fig. 2.7</b> One dimensional, axisymmetric FOB. ....	17
<b>Fig. 2.8</b> Differential control volume for 1-D model .....	20
<b>Fig. 2.9</b> Processed image of FOB face delineating the pores from the fibers .....	25
<b>Fig. 2.10</b> Resistance network for calculation of effective edge coefficient.....	29
<b>Fig. 2.11</b> Calorimetric power measurement for precision resistor .....	32
<b>Fig. 2.12</b> Calorimetric power measurement versus electrically measured power .....	32
<b>Fig. 2.13</b> Calorimetric power measurement for light source prior to alignment .....	34
<b>Fig. 2.14</b> Calorimetric power measurement for light source after alignment.....	35
<b>Fig. 2.15</b> A unit cell of core, cladding, and filling.....	37
<b>Fig. 2.16</b> Energy balance for a differential cross-section of equivalent FOB medium .....	37
<b>Fig. 2.17</b> The ratio of light travel through the cladding to axial travel through unit cell .....	39
<b>Fig. 2.18</b> Fraction of radiant energy vs. $\varphi$ . ....	40
<b>Fig. 2.19</b> The product $\beta f$ as a function of incidence angle, $\varphi$ . ....	41
<b>Fig. 2.20</b> Illustration of reflection at air-cladding interface.....	42
<b>Fig. 2.21</b> The fraction of transmitted energy ( $1-\rho$ ) as a function of the incidence angle, $\varphi$ . ....	43
<b>Fig. 2.22</b> Fraction of incident radiation as a function of incidence angle .....	44
<b>Fig. 2.23</b> Ratio of axial travel to cladding travel versus incidence angle.....	45
<b>Fig. 2.24</b> $\beta$ multiplied by the fraction of radiation transmitted into the cladding, ( $1-\rho$ ), versus incidence angle.....	46
<b>Fig. 2.25</b> Temperature distribution in FOB for nominal conditions and values of $\dot{q}_{inc}'' = \pm 20\%$ ...	48
<b>Fig. 2.26</b> Temperature distribution in FOB for nominal conditions and values of $h_{ff} = \pm 50\%$ . ...	49
<b>Fig. 2.27</b> Temperature distribution in FOB for nominal conditions and values of $h_{edge} = \pm 30\%$ . ...	50
<b>Fig. 2.28</b> Temperature distribution in FOB for nominal conditions and values of $L_{ch,\alpha} = \pm 50\%$ . ...	51

## Chapter 3

<b>Fig. 3.1</b> Laboratory setup at ORNL to simulate on-sun conditions.....	53
<b>Fig. 3.2</b> Spectral power distribution of the Cogent light source.....	54
<b>Fig. 3.3</b> Images of polished FOBs built at ORNL .....	55
<b>Fig. 3.4</b> Images of experimental FOBs built at ORNL.....	56

<b>Fig. 3.5</b> Images of FOBs with acrylic and aluminum collets .....	<b>56</b>
<b>Fig. 3.6</b> Thermographic image of FOB with aluminum collet .....	<b>58</b>
<b>Fig. 3.7</b> Temperature rise from ambient as a function of time for FOB with aluminum collet....	<b>58</b>
<b>Fig. 3.8</b> Heating sequence for the aluminum-collet FOB .....	<b>59</b>
<b>Fig. 3.9</b> Collet and thermocouple orientation for experimental setup #1 .....	<b>62</b>
<b>Fig. 3.11</b> Spectral power distribution of the 500W mercury arc lamp .....	<b>63</b>
<b>Fig. 3.12</b> Schematic of experimental setup.....	<b>64</b>
<b>Fig. 3.13</b> Temperature measurements recorded at the surface and inside the FOB .....	<b>65</b>
<b>Fig. 3.14</b> Thermocouple locations within the FOB .....	<b>66</b>
<b>Fig. 3.15</b> Thermocouples attached to fiber optic cables .....	<b>67</b>
<b>Fig. 3.16</b> Temperature rise from ambient as a function of dimensionless axial position for different radial locations within the experimental FOB .....	<b>68</b>
<b>Fig. 3.17</b> Front face of the experimental FOB.....	<b>69</b>
<b>Fig. 3.18</b> 1-D model fit to experimental data.....	<b>70</b>

## Chapter 4

<b>Fig. 4.1</b> Images of the experimental FOB front face delineating the gaps from the fibers .....	<b>75</b>
<b>Fig. 4.2</b> Arbitrary annulus of the face of the experimental FOB at position $\bar{r}$ of width $\Delta r$ .....	<b>75</b>
<b>Fig. 4.3</b> Porosity as a function of dimensionless radius for the experimental FOB .....	<b>76</b>
<b>Fig. 4.4</b> Unit cell geometry for the calculation of effective thermal conductivity .....	<b>78</b>
<b>Fig. 4.5</b> Axial and radial conductivity as a function of dimensionless radius for the 2-D model	<b>79</b>
<b>Fig. 4.6</b> Schematic of the 2-D, axisymmetric model of the experimental FOB .....	<b>80</b>
<b>Fig. 4.7</b> 2-D model steady state temperature predictions for the experimental FOB .....	<b>81</b>
<b>Fig. 4.8</b> Measured and predicted temperature in the experimental FOB.....	<b>82</b>
<b>Fig. 4.9</b> Image of a thermally fused FOB with 126 fibers delineating the gaps from the fibers..	<b>83</b>
<b>Fig. 4.10</b> Porosity as function of dimensionless radius for the experimental and on-sun FOBs..	<b>84</b>
<b>Fig. 4.11</b> Schematic of the on-sun FOB and assembly showing .....	<b>85</b>
<b>Fig. 4.12</b> HSL assembly and its associated components .....	<b>86</b>
<b>Fig. 4.13</b> Spectral power distribution for direct normal solar radiation .....	<b>87</b>
<b>Fig. 4.14</b> 2-D model steady state temperature predictions for the on-sun FOB .....	<b>88</b>

## Chapter 5

<b>Fig. 5.1</b> 2-D model steady state temperature predictions for the FOB with a single copper rod at its center .....	<b>92</b>
<b>Fig. 5.2</b> Experimental FOB with aluminum filled approximately 15 cm into the pores .....	<b>93</b>
<b>Fig. 5.3</b> 2-D model steady state temperature predictions for the FOB with aluminum filled pores. .....	<b>94</b>
<b>Fig. 5.4</b> Digital image of the experimental FOB with copper wire .....	<b>95</b>
<b>Fig. 5.5</b> 2-D model steady state temperature predictions for the experimental FOB with copper wire .....	<b>96</b>
<b>Fig. 5.6</b> Temperature rise from ambient as a function of dimensionless axial position within the experimental FOB for a non-thermally managed FOB and a thermally managed FOB .....	<b>97</b>
<b>Fig. 5.7</b> Relative temperature rise for the thermally managed vs. non-thermally managed FOB .... .....	<b>98</b>

## List of Tables

<b>Tab. 2.1</b> Optical fiber properties .....	<b>11</b>
<b>Tab. 2.2</b> Comparison of physical and image-based measurements.....	<b>26</b>
<b>Tab. 2.3</b> Parallel conductivity for air-filled FOB .....	<b>27</b>
<b>Tab. 2.4</b> Values of $\beta_{eff}$ and $\beta\rho_{eff}$ for different distributions of incident radiation.....	<b>46</b>
<b>Tab. 2.5</b> Description and value of the parameters used for study .....	<b>47</b>

# Nomenclature

$A$	area (m <sup>2</sup> )
$C$	concentration ratio
$C_{1,2,3,4,5}$	constants used in analytical solution
$d$	diameter (m)
$f$	fraction of radiant energy
$\dot{g}'''$	volumetric generation (W/m <sup>3</sup> )
$h$	heat transfer coefficient (W/m <sup>2</sup> -K)
$\bar{h}$	average heat transfer coefficient (W/m <sup>2</sup> -K)
$h_{fg}$	latent heat of vaporization (J/kg)
$k$	conductivity (W/m-K)
$L$	length of FOB (m)
$L_{ch}$	characteristic length (m)
$m$	fin constant for FOB (1/m)
$M$	mass (kg)
$N$	number of optical fibers in FOB
$NA$	numerical aperture of optical fiber
$n$	index of refraction
$p$	perimeter (m)
$P$	power (W)
$\dot{q}$	heat transfer rate
$\dot{q}''$	heat flux (W/m <sup>2</sup> )
$r$	radius (m)
$\bar{r}$	dimensionless radius
$R$	thermal resistance (K/W)
$s$	path length through cladding (m)
$t$	time (s)
$T$	temperature (°C)
$x$	axial location (m)
$\bar{x}$	dimensionless axial location

## Greek symbols

$\alpha$	absorption coefficient (1/m, %/m, dB/m)
$\beta$	ratio of path length through cladding to unit length
$\delta$	thickness (m)
$\varepsilon$	emissivity
$\phi$	fractional area of FOB face
$\varphi$	angle
$\kappa$	conversion factor (m/pixels)
$\rho$	reflectivity
$\sigma$	Stefan-Boltzmann constant

$\theta$  temperature difference with respect to air (K)

### Subscripts

$\perp$	perpendicular
$\parallel$	parallel
%	measurement in percent
<i>a</i>	ambient air
$\alpha$	related to light that strikes the pores
<i>bundle</i>	FOB
<i>clad</i>	cladding of optical fiber
<i>conv</i>	convection
<i>core</i>	core of optical fiber
<i>dB</i>	measurement in dB
<i>edge</i>	edge of FOB
<i>eff</i>	effective
<i>face</i>	face of FOB
<i>fibers</i>	all fibers in FOB
<i>fill</i>	filling material of FOB
<i>ff</i>	front face of FOB
<i>h</i>	homogeneous
<i>hcp</i>	hexagonal close packed
<i>inc</i>	incident
<i>ins</i>	insulation
<i>light on</i>	light source on
<i>light off</i>	light source off
<i>ntm</i>	non-thermally managed
<i>o</i>	unit length
<i>oper</i>	operating condition
<i>p</i>	particular
<i>pf</i>	packing factor
<i>pore</i>	pores of FOB
<i>primary</i>	primary mirror
<i>rad</i>	radiation
<i>refl</i>	reflected radiation
<i>rf</i>	rear face of FOB
<i>s</i>	surface
<i>source</i>	light source
$\tau$	related to light transmitted through the core
<i>tm</i>	thermally managed
<i>tot</i>	total
<i>x</i>	in axial direction





## Chapter 1

# Introduction to Hybrid Solar Lighting

## 1.1 Hybrid Solar Lighting Overview

### 1.1.1 Components of the Hybrid Solar Lighting System

Hybrid solar lighting (HSL) systems are designed to collect visible solar radiation for use as indoor lighting. An HSL system, Fig. 1.1, consists of three major components: 1) a sunlight collector assembly, which collects, filters and concentrates solar radiation, 2) a light distribution system, which distributes the concentrated solar radiation into the building via hybrid luminaires, and 3) a light transmission system, which transmits the collected solar radiation from the collector to the luminaires via a plastic fiber optic bundle (FOB). The solar spectrum can be broken into three major components: 3% ultraviolet, 41% visible and 56% infrared. The purpose of the collector, Fig. 1.2, is to concentrate and filter direct normal solar radiation. The components of the collector that accomplish these tasks are the primary mirror, the cold mirror and the hot mirror. The function of the primary mirror is to collect a substantial portion of beam normal solar radiation over all wavelengths by tracking the sun as it moves across the sky and to reflect this radiation onto the cold mirror. The infrared radiation that is reflected to the cold mirror is transmitted through it and therefore eliminated. The visible and ultraviolet portions of the spectrum are reflected from the cold mirror onto the hot mirror. The hot mirror transmits only the visible portion of the radiation; the incident ultraviolet radiation as well as any residual infrared radiation is absorbed or reflected. The visible radiation that is transmitted through the

hot mirror is delivered to the face of the FOB. The FOB carries the useful, visible light through the roof of the building to the hybrid luminaires.

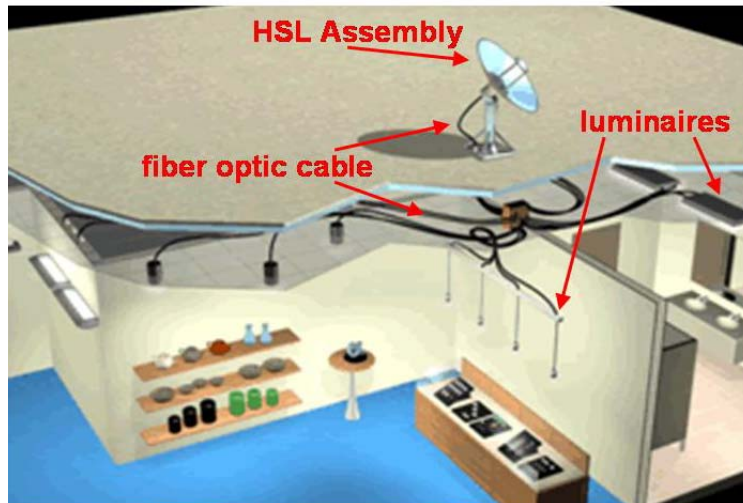


**Figure 1.1:** Schematic of an HSL system showing its three major components. Adapted from (Oak Ridge National Lab, 2005).

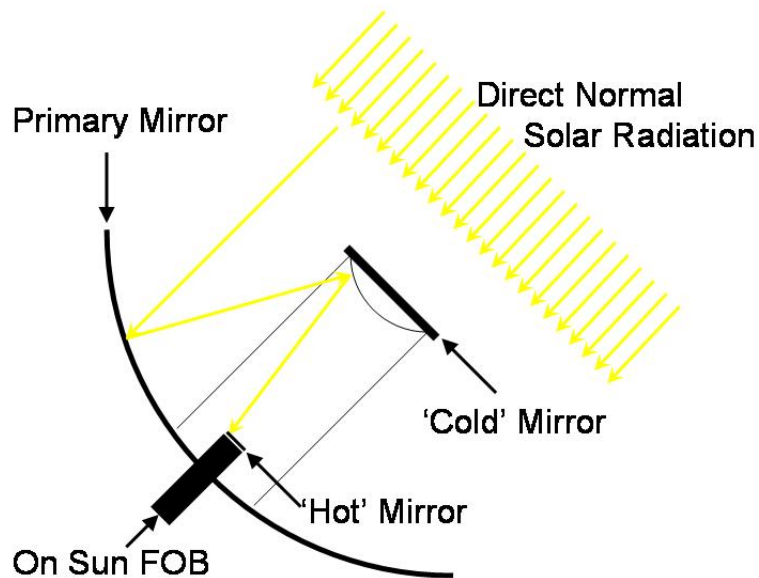


**Figure 1.2:** Collector within an HSL system.

### 1.1.2 Motivations for HSL Systems

The primary motivation for HSL systems is its potential to significantly reduce energy consumption relative to conventional lighting systems. HSL systems reduce energy consumption

directly by reducing the lighting energy requirement (some fraction of the lighting requirement can be obtained at no electrical cost using the HSL) and indirectly by reducing the cooling load associated with the lighting system. Cooling loads in buildings are reduced due to the increased luminous efficacy of an HSL system as compared to conventional incandescent or fluorescent lighting. Efficacy is defined as the amount of luminous power in a given amount of radiative power and is commonly measured in lumens/Watt. The lumen is a unit of luminous power, which is a measure of human sensitivity to the brightness of a light source (e.g. the more luminous a source, the brighter it appears to an observer). For common visual tasks, a luminous flux in the range of 300 to 750 lumens/m<sup>2</sup> is recommended by the IES Handbook (IESNA, 2000). Typical efficacy values for incandescent and fluorescent lighting are 15 lumens/Watt and 80 lumens/Watt respectively (Schlegel, 2003). In contrast, HSL has an efficacy of approximately 200 lumens/Watt (Schlegel, 2003). The increased efficacy of HSL, therefore, reduces the thermal heating for a given lighting requirement (by as more than 50% when the HSL is the only source of light) and its associated cooling load.

Figures 1.3 and 1.4 illustrate the motivation for the development of the HSL technology. Figure 1.3 breaks down the delivered energy usage in commercial buildings by end use. The three bars for each end usage category correspond to actual data from 2003 and projected data for 2010 and 2025. Both cooling and lighting are relatively large end usages of energy in commercial buildings. Figure 1.4 breaks down the electrical energy usage in commercial buildings by end use in the year 1999. Note that the lighting represents nearly one quarter of the end usage of electrical energy in commercial buildings.

### Commercial Energy Usage

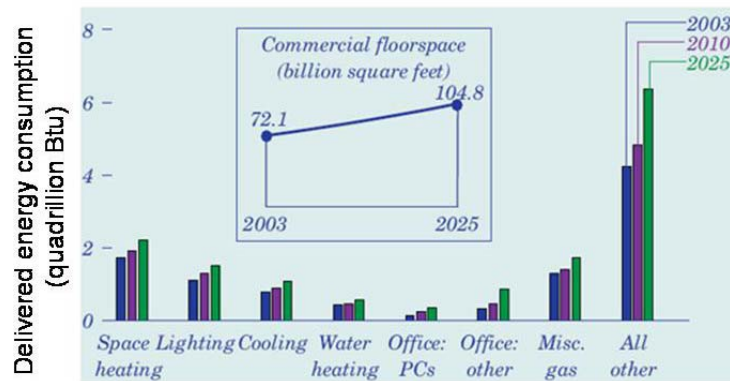


**Figure 1.3:** Delivered commercial energy consumption in quadrillion Btu as a function of end usage. Note that lighting and cooling are relatively large end usages (Department of Energy, 2005).

### Electrical Energy Usage in Commercial Buildings

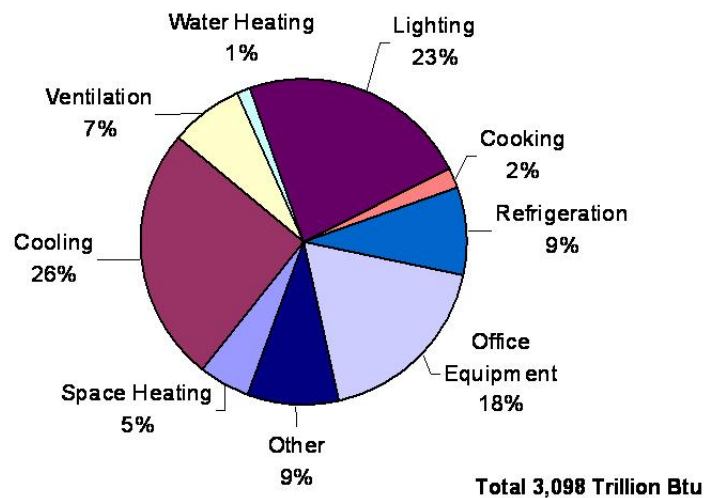


**Figure 1.4:** Electrical energy consumption in commercial buildings as a function of end usage for 1999. Note that lighting and cooling are the primary end usages for electricity in commercial buildings. (Department of Energy, 2005).

## **1.2 Literature Review of Hybrid Solar Lighting**

Research on HSL can be broken down into two categories: research related to the performance of the system as a whole and research related to the performance of individual components within the system. Early articles on the overall design and performance of an HSL system include Muhs (2000a) and Muhs (2000b). A cost analysis based on TRNSYS (Klein et al., 2000) model simulations of the system are presented by Schlegel (2003) and Schlegel et al. (2004). Color rendering and correlated color temperature calculations for the system using TRNSYS are detailed in Burkholder (2004). Performance estimates of an installed HSL system are presented by Muhs et al. (2003).

The original design of the HSL system utilized the infrared radiation passing through the ‘cold’ mirror by converting it to electrical energy using a photovoltaic array sensitive to infrared radiation. Fraas et al. (2001) and Frass et al. (2002) describe some of the research done with these PV components. Earl et al. (2003) describes the design of hybrid luminaires used to distribution of sunlight. Maxey et al. (2003) describes the techniques used to couple the fiber optic cables used in the transmission of sunlight. Tekelioglu and Wood (2003) describe the thermal management of the fiber optic cables; this study is discussed in more detail in the subsequent sections.

## **1.3 Goals and Motivation for Current Research**

A key component of the HSL system is the fiber optic system that is used to transmit the light from the collector to the luminaire. Previous designs of the HSL system utilized eight, large diameter plastic optical fibers to transmit the visible light from the collectors; however, this

system suffered from thermal management issues due to residual infrared radiation at the face of the optical fibers (Tekelioglu and Wood, 2003). In the current HSL system, the eight individual plastic fibers have been replaced with a fiber optic bundle (FOB) of smaller diameter fibers that are each surrounded by a thin layer of fluorinated polymer cladding and packed in a hexagonal close-packed array. This close-packed array is defined by its porosity, which is the ratio of the open area of the FOB to the total area of the FOB. The porosity of the FOB face is an important characteristic because any concentrated radiation that does not fall directly upon the optical fibers will not be transmitted to the luminaires and instead contributes to the thermal loading on the FOB. The optical fibers are designed so that any radiation that strikes the face of a fiber within the design range of incident angles is “trapped” by total internal reflection. However, radiation that strikes the open area surrounding the fibers will never enter the fibers and will instead be absorbed in the cladding very close to the FOB face. Therefore, the FOB thermal loads can be divided into two components. First, there is radiation that is incident on the face of the plastic fibers and therefore contributes a low level of volumetric generation within the FOB related to transmission loss. Second, and more importantly, radiation incident on the pores between optical fibers contributes a high level of volumetric generation that is concentrated near the face of the FOB. The level of heat flux on the face of the FOB that is expected during on-sun operation is 100’s of  $\text{kW/m}^2$  (see Chapter 4 for the on-sun heat flux calculation) and therefore it is necessary to understand and manage the thermal loads that result in order to control the temperature within the FOB; this is the primary concern of this thesis.

The first step towards achieving this goal is the development of a predictive thermal model of the FOB. A one-dimensional (1-D) model was developed by assuming that the temperature

gradients radially within the FOB are negligible. An experiment was fabricated using a precisely instrumented FOB section that is exposed to artificial illumination in a controlled environment. The FOB section was insulated so that it approached the 1-D limit. The resulting experimental data provide information regarding the characteristics of the thermal load associated with the radiation that is incident on the air gaps between the fibers and validate the 1-D model. The thermal loads are used to develop a more detailed, two-dimensional (2-D) finite element (FE) model of the FOB and its support structure. The 2-D FE model is used to evaluate alternative thermal management strategies for the FOB within an HSL system.

## **1.4 Previous Fiber Optic Bundle Model**

Previous research on heat transfer within FOBs is very limited. Tekelioglu and Wood (2003) conducted some FE temperature analyses on plastic optical fibers used in an older design of the HSL system. In that design, 8 plastic optical fibers were design to transmit the collected solar radiation to the hybrid luminaires. The filtering process, however, did not filter infrared radiation as it does in the current system. This resulted in an infrared heat flux of approximately  $80,000 \text{ W/m}^2$  at the face of the fiber optic cable. Several thermal management designs were considered, including forced convection, a quartz rod at the fiber tip, and an infrared filter before the fiber tip. It was concluded that an infrared filter with a quartz rod at the fiber tip was the most effective in reducing the temperature rise at the tip of the fiber optic cable.

One of the most pertinent articles concerns the production of coherent fiber optic bundles (Aleksic and Jancic, 1996). In order to better understand the sintering process required to form the coherent FOB, the authors develop a model for the temperature distribution within a

cylindrical FOB. The complex internal geometry of core cladding and air gap of the cylindrical FOB is not considered explicitly in the model; instead, the FOB is considered to be a homogenous medium with an effective thermal diffusivity in the radial and axial directions. The governing equation is derived for the FOB and a solution is obtained using a finite difference numerical method. The predicted temperature distribution is a function of the thermal diffusivities in the axial and radial directions, axial position, radial position, and time. The boundary conditions for the model are constant temperatures at the edges of the FOB, consistent with thermal loadings due to the manufacturing process as opposed to thermal loading due to incident radiation. The effective thermal diffusivities were not estimated analytically; instead, values for these quantities were determined by fitting model data with data taken for an experimental FOB.

The model for an HSL FOB presented in the following chapters is similar to the model presented by (Aleksic and Jancic, 1996); however, it is expanded in several important ways. The HSL FOB model provided by this work considers heat generation in operation that is related to light absorption within the FOB. The HSL FOB model explicitly considers the composite internal geometry within the FOB in order to calculate the effective radial and axial conductivity. The boundary conditions include radiation and convection at the edges of the FOB. Most importantly, the 2-D finite element model presented in Chapter 4 provides a powerful and flexible tool for the design and development of a thermally managed FOB, as discussed in Chapter 5.

## 1.5 Conclusion

An HSL system is designed to collect direct normal, visible solar radiation in order to displace electric lighting in commercial buildings. Not only does the system save electricity by displacing electric lighting, it also saves electricity by reducing the cooling costs by decreasing the cooling load deposited by conventional lighting; this indirect savings is realized by the increased efficacy of the delivered light.

Previous research into HSL systems has concerned the overall performance of the system and its individual components. A key component of the HSL system is the FOB, which is the focus of this research. The motivation for researching the FOB is related to observed thermal failures of the FOB when exposed to concentrated sunlight. This research describes the development of a predictive thermal model of an FOB for an HSL system. The model is verified experimentally against temperature measurements obtained in the lab under controlled conditions. The model is then used to evaluate alternative thermal management strategies.

## Chapter 2

# One-Dimensional Model

### 2.1 Introduction

The fiber optic bundle (FOB) geometry described in this section serves as a basis for a theoretical one-dimensional (1-D) model as well as a blueprint for the construction of an experimental FOB that was instrumented and tested under controlled laboratory conditions. This chapter therefore begins with a description of the basic FOB geometry and the associated heat loads and heat transfer parameters. The chapter continues with the derivation of an analytical 1-D model and provides estimates of the loads and parameters associated with the model. The chapter concludes with a sensitivity analysis on the parameters that define the FOB. The 1-D model is used in conjunction with the experimental results detailed in Chapter 3 in order to infer the characteristic length associated with light absorption in the pores of the FOB.

### 2.2 Fiber Optic Bundle Geometry

#### 2.2.1 Fiber materials and properties

The FOB is constructed of several plastic optical fibers, each on the order of meters in length. The fibers are CK-120 fibers manufactured by the Mitsubishi Rayon Corporation. The core of the fiber is polymethylmethacrylate (PMMA) and the cladding material is made from a fluorinated polymer (Fig.2.1).

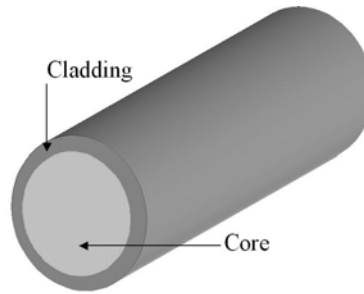


**Figure 2.1:** End of a plastic fiber optic cable (not to scale).

Table 2.1 summarizes the relevant fiber optic properties including core diameter and tolerance, transmission loss, refractive indices, and the storage and operating temperature; these were all obtained from the manufacturer specification sheet (Mitsubishi, 2001). The thermal conductivity of the core and cladding are also shown in Table 2.1; these values are taken from Osswald (1998). The fluorinated polymer that constitutes the cladding was not specified; therefore the cladding is assumed to be ethylene tetrafluoroethylene because the value of the refractive index given in Osswald agrees with the refractive index provided by the manufacturer.

**Table 2.1:** Optical fiber properties.

Description	Symbol	Value
Diameter of fiber core	$d_{core}$	$2.95 \pm 0.18$ mm
Fiber transmission loss	$\alpha_{dB}$ $\alpha\%$	0.2 dB/m 4.5 %/m
Core index of refraction	$n_{core}$	1.49
Cladding index of refraction	$n_{clad}$	1.40
Numerical aperture	$NA$	0.5
Operating temperature range	$T_{oper}$	$-55^{\circ}\text{C} < T_{oper} < 70^{\circ}\text{C}$
Core conductivity	$k_{core}$	0.18 W/m-K
Cladding conductivity	$k_{clad}$	0.23 W/m-K

### 2.2.2 Fiber optic bundle and packing factor

To construct a FOB, individual optical fibers are packed into a cylindrical array as shown in Fig.

2.2.

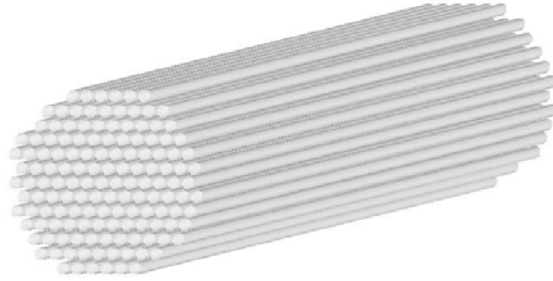


**Figure 2.2:** Cylindrical array of optical fibers packed together to form a FOB.

The arrangement of fibers within the FOB is quantified by the packing factor ( $\phi_{pf}$ ). The packing factor is defined in Eq. (2.1) as the ratio of the area of the FOB face occupied by the optical fibers ( $A_{fibers}$ ) to the total area of the FOB face ( $A_{bundle}$ ).

$$\phi_{pf} = \frac{A_{fibers}}{A_{bundle}} \quad (2.1)$$

Figure 2.3 illustrates the packing factor as a function of the ratio of the bundle diameter to the fiber diameter assuming a perfect hexagonal close-packed array. The ‘spikes’ in the packing factor are due to the sudden increase in  $A_{fibers}$  that occurs when the bundle diameter becomes large enough to insert additional fiber optic cables around its perimeter. An illustration of this behavior is shown in Fig. 2.4. Figure 2.5 is a photograph of the face of the experimental FOB and shows that there may be significant differences in  $\phi_{pf}$  at various locations, with some locations approaching the ideal packing geometry illustrated in Fig. 2.4 while other locations are more loosely packed. In general, the packing factor at the center of the FOB is greater than the packing factor at the bundle edge.

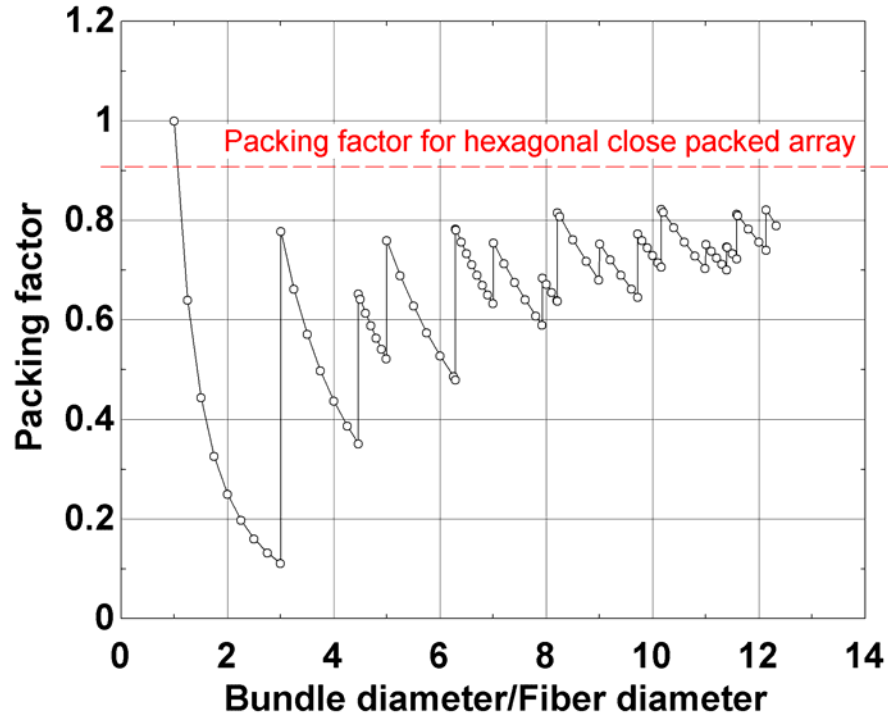


**Figure 2.3:** Packing factor for an ideal FOB as a function of the ratio of the bundle to fiber diameter. As the bundle diameter increases, the packing factor decreases until more fiber optic cables can be inserted into the bundle diameter resulting in the spikes shown in the figure. The optimal packing with cylindrical fibers would be hexagonal closed packing. This theoretical maximum,  $\phi_{pf,hcp} = 0.907$ , is shown as a dashed line.

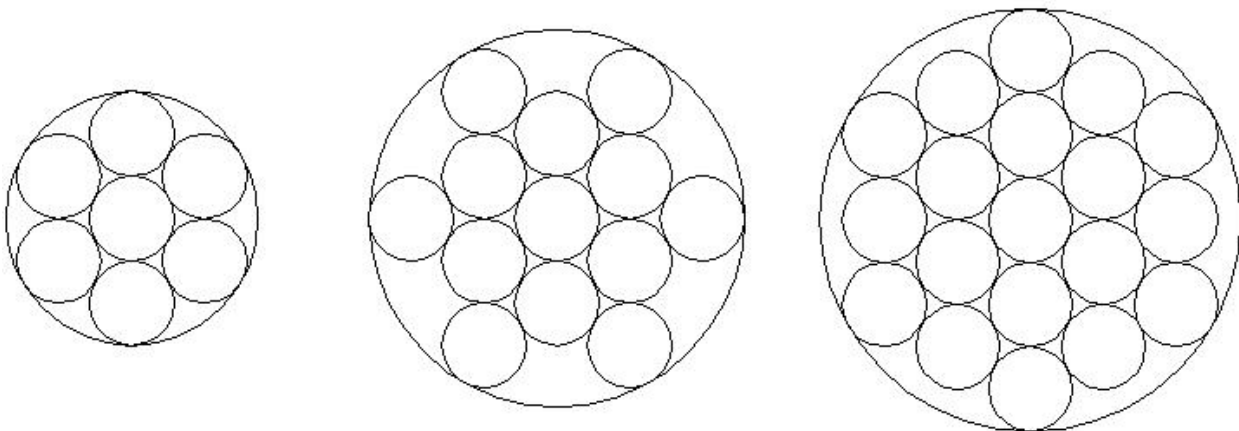


**Figure 2.4:** Cylindrical fiber optic rods ideally packed into a cylindrical collet (front view). Symmetric hexagonal close packing is assumed as the only configuration for the cables. The bundle diameter is increased until additional fibers can be inserted.



**Figure 2.5:** The face of an experimental FOB. The area outlined with a solid box shows a region with a relatively high packing factor compared to the area outlined with a dashed box, which has a relatively low packing factor.

The composite structure of the FOB consists of three materials: the PMMA core, the fluorinated polymer cladding and another material that fills the remaining space between the optical fibers. In most cases, the filler material will be air; however, other materials are considered during the evaluation of thermal management strategies. The fraction of the FOB face that is core ( $\phi_{core}$ ), filling material ( $\phi_{fill}$ ), and cladding ( $\phi_{clad}$ ) are defined in Eqs. (2.2) through (2.4).

$$\phi_{core} = \frac{A_{core}}{A_{bundle}} \quad (2.2)$$

$$\phi_{fill} = \frac{A_{fill}}{A_{bundle}} \quad (2.3)$$

$$\phi_{clad} = \frac{A_{clad}}{A_{bundle}} \quad (2.4)$$

where  $A_{core}$ ,  $A_{fill}$ , and  $A_{clad}$ , are the areas of the FOB face occupied by the core, the filling material, and the cladding, respectively. The packing factor, then, is simply the fraction of the FOB face that is both core and cladding, Eq. (2.5).

$$\phi_{pf} = \phi_{core} + \phi_{clad} \quad (2.5)$$

In future calculations the porosity ( $\phi_{pore}$ ), defined as the fraction of the FOB face that is both cladding and filling material (not core), will be important. This fraction is defined in Eq. (2.6),

$$\phi_{pore} = \frac{A_{pore}}{A_{bundle}} \quad (2.6)$$

where  $A_{pore}$  is the area of the FOB face occupied by the filling material and the cladding. It also follows that the fractions for all materials of the FOB should sum to 1, Eq. (2.7).

$$\phi_{core} + \phi_{fill} + \phi_{clad} = 1 \quad \text{or} \quad \phi_{core} + \phi_{pore} = 1 \quad (2.7)$$

## 2.3 Fiber Optic Bundle Loads and Parameters

The porosity of the FOB face is significant because it is directly related to the thermal load on the FOB. Radiation that is incident on the FOB face, Fig. 2.6, either passes through the PMMA fibers and subsequently moves relatively easily through the FOB due to total internal reflection or is incident on the pores (the cladding and filler material) and subsequently is absorbed by the FOB over a volume that is very close to the FOB face.

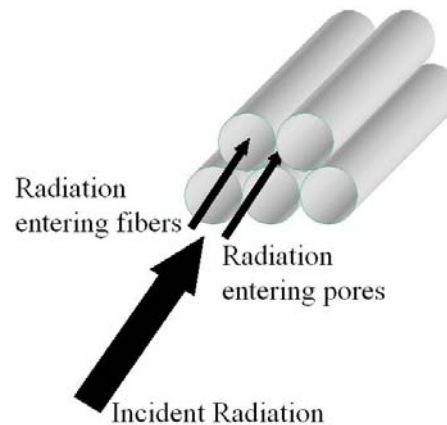


**Figure 2.6:** Radiation incident on the FOB face either enters the fibers and moves through the core via total internal reflection or enters the pores in the FOB face and is subsequently absorbed quickly.

As the radiation passes through the FOB, either through the fibers or through the pores, a portion is absorbed and generates a thermal load that manifests itself as a volumetric generation rate within the FOB. The radiation traveling through the fibers contributes a nearly constant and relatively low level of volumetric generation whereas the radiation traveling through the pores contributes to a higher level of volumetric generation that is concentrated near the FOB face. This difference in heat generation arises from the fact that the light passing through the pores is forced through an optical path that is relatively absorbent, primarily due to the high absorptivity of the cladding whereas the light passing through the fibers does not have to pass through the cladding due to total internal reflection.

The packing factor also affects the effective thermal conductivity of the FOB as well as the heat transfer coefficients from the FOB faces; however, these are secondary effects when compared to the effect of the packing factor on volumetric heat generation. The axial conductivity of the FOB is modeled as an equivalent medium based on the composite structure of the FOB, which in turn depends on the packing factor as well as the material properties of which it is composed.

The heat transfer coefficients at the faces of the FOB are affected by the packing factor because it affects the amount of surface area from which heat can be convected and radiated.

Insulation was wrapped around the experimental FOB in order to ensure 1-D behavior (i.e., to reduce temperature gradients in the radial direction) and also to facilitate the construction of the FOB. However, the 1-D model does consider the thermal resistance associated with conduction through the insulation and convection and radiation from the insulation surface; the insulation is not perfect and so a significant amount of heat is lost from its outer surface. However, the insulation is sufficient so that radial temperature gradients within the FOB are small relative to axial temperature gradients which is the key assumption used to develop the 1-D model.

## 2.4 Analytical Derivation of 1-D Model

The derivation of the 1-D analytical model of the FOB is illustrated in Figure 2.7.

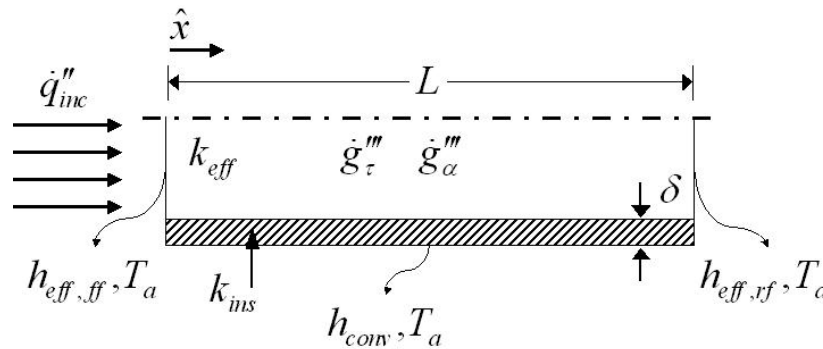


**Figure 2.7:** One dimensional, axisymmetric FOB.

The generation terms in Figure 2.7,  $\dot{g}'_{\tau}$  and  $\dot{g}'_{\alpha}$ , are related to the absorption of illumination energy as it passes through the FOB. The term  $\dot{g}'_{\tau}$  refers to the absorption of energy that is associated with the light that is transmitted through the fiber cores whereas  $\dot{g}'_{\alpha}$  refers to the

absorption of energy that is associated with the radiation in the pores which passes through a complex path that includes a combination of fill material, cladding and core.

It is assumed that the rate at which energy is absorbed within the FOB is proportional to the local intensity of radiation. The Bouguer-Lambert law (Siegel and Howell, 2002) gives the fractional change in the rate of energy transferred through an absorbing medium ( $\dot{q}$ ), Eq. (2.8).

$$\frac{d\dot{q}}{\dot{q}} = -\frac{1}{L_{ch}} dx \quad (2.8)$$

where  $L_{ch}$  is the characteristic length of the absorbing medium and  $x$  is the distance from the face of the FOB. The solution to Eq. (2.8) implies that the volumetric heating associated with the light absorption must be exponentially distributed with position according to the characteristic absorption length. For example, the volumetric heating due to the radiation in the pores can be expressed as:

$$\dot{g}''_{\alpha} = C_1 \exp\left(-\frac{x}{L_{ch,\alpha}}\right) \quad (2.9)$$

where  $C_1$  is a constant and  $L_{ch,\alpha}$  is the characteristic length associated with the average optical path traveled by radiation that is incident on the pores. It is possible to relate  $C_1$  to the incident energy flux ( $\dot{q}''_{inc}$ ) by requiring that all of the energy that is incident on the pores must eventually be absorbed in the limit of an infinitely long bundle:

$$\dot{q}''_{inc} \phi_{pore} = \int_0^{\infty} \dot{g}''_{\alpha}(x) dx \quad (2.10)$$

or

$$\dot{q}''_{inc} \phi_{pore} = \int_0^{\infty} C_1 \exp\left(-\frac{x}{L_{ch,\alpha}}\right) dx \quad (2.11)$$

where  $A_{pore}$  is the area associated with the pores on the bundle face. Carrying out the integration leads to:

$$\dot{q}_{inc}'' \phi_{pore} = L_{ch,\alpha} C_1 \quad (2.12)$$

Solving for  $C_1$  leads to:

$$C_1 = \frac{\phi_{pore} \dot{q}_{inc}''}{L_{ch,\alpha}} \quad (2.13)$$

Therefore, the volumetric heating due to energy in the pores can be written as:

$$\dot{g}_\alpha''' = \frac{\dot{q}_{eff,\alpha}''}{L_{ch,\alpha}} \exp\left(-\frac{x}{L_{ch,\alpha}}\right) \quad (2.14)$$

where

$$\dot{q}_{eff,\alpha}'' = \phi_{pore} \dot{q}_{inc}'' \quad (2.15)$$

A similar derivation results in the expression for the volumetric heating due to the absorption of radiation transmitted through the fiber cores ( $\dot{g}_\tau'''$ ).

$$\dot{g}_\tau''' = \frac{\dot{q}_{eff,\tau}''}{L_{ch,\tau}} \exp\left(-\frac{x}{L_{ch,\tau}}\right) \quad (2.16)$$

where

$$\dot{q}_{eff,\tau}'' = \phi_{core} \dot{q}_{inc}'' \quad (2.17)$$

and  $L_{ch,\tau}$  is the characteristic length for absorption of radiation that is passing through the fiber cores. Note that the optical fibers are designed to transmit light very effectively and therefore it is expected that  $L_{ch,\tau}$  will be much larger than  $L_{ch,\alpha}$ .

The governing equation for the FOB is obtained by considering an energy balance applied to a differential control volume, shown in Figure 2.8:

$$\dot{q}_x + \dot{g}_\tau + \dot{g}_\alpha = \dot{q}_x + \frac{d\dot{q}_x}{dx} dx + \dot{q}_{edge} \quad (2.18)$$

where  $\dot{q}_x$  is the conductive heat transfer through the composite matrix composed of core, filling, and cladding at location  $x$ ,  $\dot{g}_\tau$  and  $\dot{g}_\alpha$  are the heating within the control volume related to the absorption of radiation transmitted through the fiber cores and the pores, respectively, and  $\dot{q}_{edge}$  is the heat transferred from the edge of the FOB through insulation and via natural convection and radiation from the edge of the insulation.

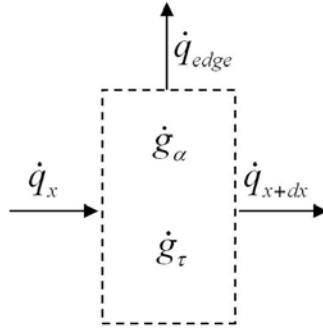


**Figure 2.8:** Differential control volume for 1-D model.

Substituting Fourier's law, written in terms of an effective conductivity, and the volumetric heat generation terms, previously derived, into Eq. (2.18) leads to:

$$\begin{aligned} \frac{\dot{q}_{eff,\tau}''}{L_{ch,\tau}} \exp\left(-\frac{x}{L_{ch,\tau}}\right) \pi r_{bundle}^2 dx + \frac{\dot{q}_{eff,\alpha}''}{L_{ch,\alpha}} \exp\left(-\frac{x}{L_{ch,\alpha}}\right) \pi r_{bundle}^2 dx = \\ \frac{d}{dx} \left[ -k_{eff} \pi r_{bundle}^2 \frac{dT}{dx} \right] dx + 2\pi r_{bundle} h_{eff,edge} (T - T_a) dx \end{aligned} \quad (2.19)$$

where  $r_{bundle}$  is the outer radius of the bundle,  $T_a$  is the temperature of the ambient air surrounding the bundle,  $k_{eff}$  is the effective thermal conductivity of the core, cladding, filling composite in the  $x$  direction and  $h_{eff,edge}$  is an effective heat transfer coefficient for the edge of the bundle. The technique used to calculate  $h_{eff,edge}$  is described in the following section.

Simplifying and rearranging Eq. (2.19) leads to:

$$\frac{d^2T}{dx^2} - \frac{p h_{eff,edge}}{k_{eff} A_{bundle}} (T - T_a) = -\frac{\dot{q}_{eff,\tau}''}{L_{ch,\tau} k_{eff}} \exp\left(-\frac{x}{L_{ch,\tau}}\right) - \frac{\dot{q}_{eff,\alpha}''}{L_{ch,\alpha} k_{eff}} \exp\left(-\frac{x}{L_{ch,\alpha}}\right) \quad (2.20)$$

where  $p$  is the perimeter of the FOB (without insulation) given by  $2\pi r$  and  $A_{bundle}$  is  $\pi r_{bundle}^2$ .

The boundary conditions for Eq. (2.20) are related to convection at the two bundle faces:

$$h_{eff,ff} (T_{x=0} - T_a) = k_{eff} \left. \frac{dT}{dx} \right|_{x=0} \quad (2.21)$$

and

$$h_{eff,rf} (T_{x=L} - T_a) = -k_{eff} \left. \frac{dT}{dx} \right|_{x=L} \quad (2.22)$$

where  $L$  is the length of the bundle and  $h_{eff,ff}$  and  $h_{eff,rf}$  are the heat transfer coefficients characterizing convection from the exposed front and rear faces of the FOB, respectively.

Equations (2.20) through (2.22) are recast in terms of  $\theta$ , the temperature difference relative to the air temperature:

$$\theta = T - T_a \quad (2.23)$$

$$\frac{d^2\theta}{dx^2} - \frac{p h_{eff,edge}}{k_{eff} A_{bundle}} \theta = -\frac{\dot{q}_{eff,\tau}''}{L_{ch,\tau} k_{eff}} \exp\left(-\frac{x}{L_{ch,\tau}}\right) - \frac{\dot{q}_{eff,\alpha}''}{L_{ch,\alpha} k_{eff}} \exp\left(-\frac{x}{L_{ch,\alpha}}\right) \quad (2.24)$$

$$h_{eff,ff} \theta_{x=0} = k_{eff} \left. \frac{d\theta}{dx} \right|_{x=0} \quad (2.25)$$

$$h_{eff,rf} \theta_{x=L} = -k_{eff} \left. \frac{d\theta}{dx} \right|_{x=L} \quad (2.26)$$

The homogeneous form of Eq. (2.24) is:

$$\frac{d^2\theta}{dx^2} - m^2\theta = 0 \quad (2.27)$$

where

$$m^2 = \frac{p h_{eff,edge}}{k_{eff} A_{bundle}} \quad (2.28)$$

Equation (2.24) has the homogeneous solution ( $\theta_h$ ):

$$\theta_h = C_2 \exp^{(mx)} + C_3 \exp^{(-mx)} \quad (2.29)$$

where  $C_2$  and  $C_3$  are undetermined coefficients. The particular solution to Eq. (2.24),  $\theta_p$ , has the form:

$$\theta_p = C_4 \exp\left(-\frac{x}{L_{ch,\tau}}\right) + C_5 \exp\left(-\frac{x}{L_{ch,\alpha}}\right) \quad (2.30)$$

where  $C_4$  and  $C_5$  are obtained by substituting Eq. (2.30) into Eq. (2.24):

$$\begin{aligned} & \frac{C_4}{L_{ch,\tau}^2} \exp\left(-\frac{x}{L_{ch,\tau}}\right) + \frac{C_5}{L_{ch,\alpha}^2} \exp\left(-\frac{x}{L_{ch,\alpha}}\right) - m^2 C_4 \exp\left(-\frac{x}{L_{ch,\tau}}\right) \\ & - m^2 C_5 \exp\left(-\frac{x}{L_{ch,\alpha}}\right) = -\frac{\dot{q}_{eff,\tau}''}{L_{ch,\tau} k_{eff}} \exp\left(-\frac{x}{L_{ch,\tau}}\right) - \frac{\dot{q}_{eff,\alpha}''}{L_{ch,\alpha} k_{eff}} \exp\left(-\frac{x}{L_{ch,\alpha}}\right) \end{aligned} \quad (2.31)$$

The constants in Eq. (2.31) are obtained by requiring that the coefficients multiplying exponentials with the same arguments must sum to zero, which leads to:

$$C_4 = \left[ \frac{\dot{q}_{eff,\tau}''}{L_{ch,\tau} k_{eff}} \right] \left[ m^2 - \frac{1}{L_{ch,\tau}^2} \right]^{-1} \quad (2.32)$$

and

$$C_5 = \left[ \frac{\dot{q}_{eff,\alpha}''}{L_{ch,\alpha} k_{eff}} \right] \left[ m^2 - \frac{1}{L_{ch,\alpha}^2} \right]^{-1} \quad (2.33)$$

The solution for the temperature distribution is the sum of the homogeneous and particular solutions:

$$\theta = C_2 \exp^{(mx)} + C_3 \exp^{(-mx)} + C_4 \exp\left(-\frac{x}{L_{ch,\tau}}\right) + C_5 \exp\left(-\frac{x}{L_{ch,\alpha}}\right) \quad (2.34)$$

Substituting Eq. (2.34) into the boundary conditions represented by Eq. (2.25) and Eq. (2.26) leads to:

$$h_{eff,ff} (C_2 + C_3 + C_4 + C_5) = k_{eff} \left( C_2 m - C_3 m - \frac{C_4}{L_{ch,\tau}} - \frac{C_5}{L_{ch,\alpha}} \right) \quad (2.35)$$

and

$$h_{eff,rf} \left( C_2 \exp^{(mL)} + C_3 \exp^{(-mL)} + C_4 \exp\left(-\frac{L}{L_{ch,\tau}}\right) + C_5 \exp\left(-\frac{L}{L_{ch,\alpha}}\right) \right) = -k_{eff} \left( C_2 m \exp^{(mL)} - C_3 m \exp^{(-mL)} - C_4 \frac{\exp\left(-\frac{L}{L_{ch,\tau}}\right)}{L_{ch,\tau}} - C_5 \frac{\exp\left(-\frac{L}{L_{ch,\alpha}}\right)}{L_{ch,\alpha}} \right) \quad (2.36)$$

which provide two equations that are used to determine the coefficients in the homogeneous solutions ( $C_2$  and  $C_3$ ). Equations (2.32) through (2.36) were implemented in both the Engineering Equation Solver (EES) software (Klein et al., 2005) and Excel in order to facilitate comparisons with the experimental results that are detailed in Chapter 3.

## 2.5 Evaluation of the 1-D Model Parameters

In order to implement the 1-D analytical solution derived above, it is necessary to evaluate the parameters that are involved in that solution. These include the porosity ( $\phi_{pore}$ ), the effective axial conductivity ( $k_{eff}$ ), the heat transfer coefficients from the FOB faces ( $h_{eff,ff}$  and  $h_{eff,rf}$ ) and edge ( $h_{eff,edge}$ ), the heat flux incident on the FOB face ( $\dot{q}''_{inc}$ ) and the characteristic lengths associated with heat generation within the FOB ( $L_{ch,\alpha}$  and  $L_{ch,\tau}$ ).

### 2.5.1 Calculating Porosity

In order to analytically calculate the porosity of the FOB it is necessary to know the number of optical fibers within the bundle, the radius of the FOB and the average radius of an optical fiber core. As stated earlier, the porosity of the FOB is the fraction of the area of the FOB face that is not occupied by the fiber core, Eq. (2.37).

$$\phi_{pore} = 1 - \phi_{core} \quad (2.37)$$

Eq. (2.37) can be rewritten as,

$$\phi_{pore} = 1 - \frac{N \pi r_{core}^2}{\pi r_{bundle}^2} \quad (2.38)$$

where  $N$  is the number of fibers in the FOB,  $r_{core}$  is the core radius of a single fiber, and  $r_{bundle}$  is the radius of the FOB. Precise measurement of either of the radii required by Eq. (2.38) is not straightforward. According to manufacturer's specifications (Tab. 2.1) the core diameter ( $d_{core}$ ) of a single optical fiber varies by  $\pm 0.18$  mm and Fig. 2.9 shows that the face of the experimental FOB does not have a truly circular perimeter. To circumvent these problems, both measurements are obtained using an image processed photograph of the core, shown in Fig. 2.9(b)

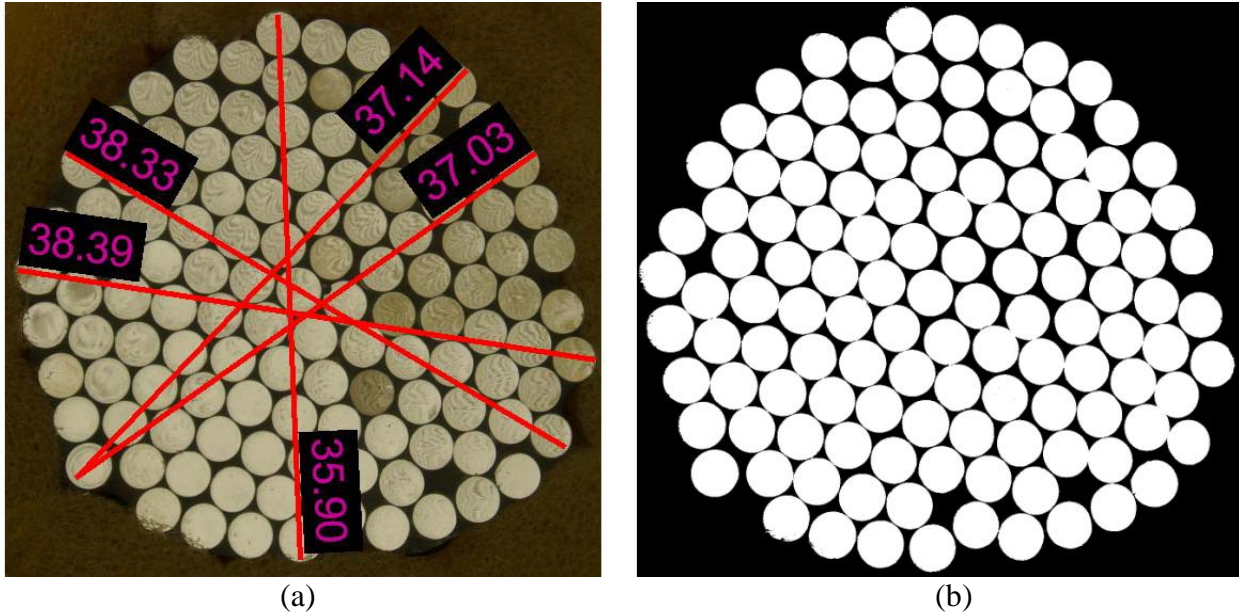


**Figure 2.9:** (a) Measurements of the experimental FOB taken with calipers. All measurements are in millimeters. (b) The same photograph as (a) after image processing has been used to clearly delineating the gaps of the FOB face from the fibers.

The average diameter (in pixels) for a single optical fiber within the experimental FOB is calculated from Fig. 2.9(b) by summing the radius of each fiber core and dividing by the total number of fibers,  $N = 120$ . The average diameter of a single fiber core is found to be 100 pixels. An effective radius ( $r_{eff}$ ) for the FOB is defined in Eq. (2.39), and calculated using the image processed photograph shown in Fig. 2.9(b).

$$A_{bundle} = \pi r_{eff}^2 \quad (2.39)$$

Eq. (2.39) shows that the effective radius depends on the area of the FOB; in order to calculate the area of the FOB using Fig. 2.9(b), an outer perimeter of the FOB is specified manually. All pixels within this perimeter are counted in order to determine the total FOB area, 1,241,998 pixels.

To make the bundle and fiber radii determined above in terms of pixels useful, it is necessary to conversion a factor, ( $\kappa$ ), between pixels to meters. The distances between several points around the outer edge of the FOB were measured in both pixel units (via image processing) and physical distance (using digital calipers). The conversion factor is calculated by minimizing the RMS error between the image-based measurements, which are converted to meters by  $\kappa$ , and the physical measurements. The specific physical measurements are shown in Fig. 2.9(a) and a comparison of the two measurement techniques is summarized in Table 2.2. The result is a conversion factor of  $\kappa = 0.0292$  mm/pixel, a core radius of  $r_{core} = 1.46$  mm, a FOB area of  $A_{bundle} = 1064$  mm<sup>2</sup>, and an effective radius of  $r_{eff} = 18.4$  mm.

**Table 2.2:** Comparison of physical and image-based measurements. The conversion factor for the image is 0.0292 mm/pixel. Note, all measurements agree to within 0.6% error.

Measurement	Location 1	Location 2	Distance (pixels)	Distance (mm) (using image)	Distance (mm) (using calipers)
1	(912,111)	(969,1343)	1233	36.0	35.9
2	(113,331)	(1243,981)	1304	38.1	38.3
3	(3,586)	(1300,792)	1313	38.4	38.4
4	(124,1054)	(1012,138)	1276	37.3	37.1
5	(124,1054)	(1159,321)	1268	37.1	37.0

With the information above, the analytical calculation of porosity, using Eq. (2.38), is  $\phi_{pore} = 0.245$ . It is also possible to utilize the processed image of Fig. 2.9(b) to calculate the porosity by counting the number of black and white pixels within the manually specified perimeter of the FOB. The porosity, based on this technique, is the ratio of the number of black pixels (i.e.,  $A_{pore}$ ) to the total number of pixels (i.e.  $A_{bundle}$ ). The result of this calculation agrees with the analytical calculation and is  $\phi_{pore} = 0.240$ .

## 2.5.2 Effective Axial Conductivity

The core, filling and cladding are treated as parallel resistances in order to calculate the effective conductivity in the axial direction:

$$\frac{L}{k_{eff} A_{bundle}} = \left[ \frac{k_{core} A_{core}}{L} + \frac{k_{fill} A_{fill}}{L} + \frac{k_{clad} A_{clad}}{L} \right]^{-1} \quad (2.40)$$

where  $k_{fill}$ , is the conductivity of the filler material. Rearranging and substituting Eqs. (2.2) through (2.4) into Eq. (2.40) leads to,

$$k_{eff} = \phi_{core} k_{core} + \phi_{fill} k_{fill} + \phi_{clad} k_{clad} \quad (2.41)$$

For the experimental FOB, the filler material is air with a thermal conductivity given in Table 2.3. The fraction of the FOB face that is core can be determined from the information described in the previous section. The amount of cladding in the FOB is directly proportional to the amount of core material. From the manufacturer specifications, the cladding is 0.05 mm thick. Therefore, for an effective core radius of 1.46 mm, and consequently a fiber radius of 1.51 mm, the ratio of cladding area to core area is 0.0344. The fraction of filling is calculated from Eq. (2.7). The resulting effective conductivity as well as the conductivities and area fractions of the composite materials are shown in Table 2.3.

**Table 2.3:** Parallel conductivity for air-filled FOB.

<b>Parallel Conductivity</b> $k_{eff}$ (W/m-K)	$k_{core}$ (W/m-K)	$k_{fill}$ (W/m-K)	$k_{clad}$ (W/m-K)	$\phi_{core}$	$\phi_{fill}$	$\phi_{clad}$
0.15	0.18	0.027	0.23	0.76	0.21	0.03

## 2.5.3 Effective Heat Transfer Coefficients

### 2.5.3.1 Front Face and Rear Face

The effective heat transfer coefficients associated with the faces of the FOB ( $h_{eff,ff}$  and  $h_{eff,rf}$ ) are calculated by considering both radiation and convection. The natural convection heat transfer coefficient is estimated using correlations attributed to Churchill and Chu in Incropera and DeWitt (2002) for a flat plate experiencing laminar free convection flow. A film temperature (the average of the face and ambient temperature) is used to evaluate the fluid properties. Because the faces of the FOB are circular, a characteristic length based on the area of the FOB is used, Eq. (2.42).

$$L_{ch} = \sqrt{A_{bundle}} \quad (2.42)$$

The effective convection coefficient due to radiation ( $h_{rad}$ ) was estimated from Eq. (2.43) using temperatures measured experimentally and an emissivity of 0.8.

$$h_{rad} = \varepsilon \sigma (T_s + T_a)(T_s^2 + T_a^2) \quad (2.43)$$

where  $\varepsilon$  is the emissivity of the surface,  $\sigma$  is Stefan-Boltzmann's constant, and  $T_s$  and  $T_a$  are the temperature of the surface and surroundings, respectively. The resulting effective heat transfer coefficient for either FOB face ( $h_{eff,face}$ ) is the sum of the radiative and convective terms, reduced by the packing factor, Eq. (2.44).

$$h_{eff,face} = \phi_{pf} (h_{rad} + h_{conv}) \quad (2.44)$$

### 2.5.3.2 Outer Edge

The effective heat transfer coefficient characterizing heat transfer from the outer edge of the FOB ( $h_{eff,edge}$ ) is obtained using the equivalent resistance network shown in Figure 2.10, where

$R_{ins}$  is the thermal resistance due to conduction through the insulation and  $R_{rad}$  and  $R_{conv}$ , are the thermal resistances due to radiation and convection from the outer edge of the insulation.

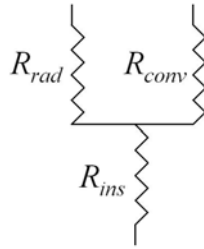


**Figure 2.10:** Resistance network for calculation of  $h_{eff,edge}$ .

The effective heat transfer coefficient for the edge of the FOB is defined as,

$$h_{eff,edge} = \frac{1}{R_{eff,edge} A_{edge}} \quad (2.45)$$

where  $A_{edge}$  is the surface area of the FOB (without insulation) and:

$$R_{eff,edge} = R_{ins} + \left[ \frac{1}{R_{rad}} + \frac{1}{R_{conv}} \right]^{-1} \quad (2.46)$$

$R_{ins}$  is a cylindrical conduction resistance defined by:

$$R_{ins} = \frac{\ln\left(\frac{r_{ins}}{r_{bundle}}\right)}{2\pi L k_{ins}} \quad (2.47)$$

where  $r_{ins}$ ,  $k_{ins}$  and  $L$  are the outer radius, conductivity and thickness of the insulation, respectively.  $R_{rad}$  is a radiation resistance defined by:

$$R_{rad} = \frac{1}{h_{rad} A_{ins}} \quad (2.48)$$

where  $A_{ins}$  is the surface area of the insulation and  $h_{rad}$  is defined in Eq.(2.43).

$R_{conv}$  is a convection resistance defined by:

$$R_{conv} = \frac{1}{\bar{h}_{ins} A_{ins}} \quad (2.49)$$

where  $\bar{h}_{ins}$  is an average heat transfer coefficient estimated using correlations attributed to Churchill and Chu in Incropera and DeWitt (2002) for a cylinder experiencing laminar free convection flow. A film temperature based on an average temperature along the length of the FOB is used to evaluate fluid properties.

#### 2.5.4 Source Heat Flux

In order to accurately measure the heat flux that is incident on the face of the FOB,  $\dot{q}_{inc}''$ , a calorimetric experiment was designed in which an Oriel 87436, 500W mercury lamp is directed into a dewar of liquid nitrogen. The power associated with the light source is absorbed by the nitrogen which affects the boil off rate. Therefore, it is possible to determine the power by measuring the rate of mass loss from the dewar at ambient conditions and comparing this with the rate of mass loss from the same dewar when it is exposed to the energy from the light source. The difference between these rates of mass loss is proportional to the power absorbed by the liquid nitrogen due to the light source ( $P_{source}$ ); the constant of proportionality is the heat of vaporization of liquid nitrogen ( $h_{fg}$ ):

$$P_{source} = h_{fg} \left[ \left( \frac{dM}{dt} \right)_{\text{light on}} - \left( \frac{dM}{dt} \right)_{\text{light off}} \right] \quad (2.50)$$

where  $M$  is the mass of the dewar and liquid nitrogen and  $t$  is time. For the experimental results described below, measurement error varied from 5%-14% and is based on the ratio of the resolution of the scale to the total mass loss for a particular experiment.

The experimental technique is validated by replacing the light source with an electrical heater that is immersed in the dewar and can be used to provide a known (via simple electrical measurements of voltage and resistance) power output. A precision resistor was placed into the liquid nitrogen bath; the resistance of the heater was measured to be  $10.02 \Omega$  while placed in the liquid nitrogen bath using a 4-wire technique. The rate of mass loss under non-energized conditions was measured by placing the dewar onto a digital scale and manually recording mass and time information for several minutes. Subsequently, a measured voltage was applied to the resistor and the rate of mass loss under this “energized” condition was recorded using the same procedure. The process was repeated for several values of power input. The results of this experiment are shown in Figure 2.11 in terms of the dimensionless dewar mass as a function of time, where dimensionless dewar mass is the mass of the dewar and liquid nitrogen normalized by the initial mass of the dewar and liquid nitrogen. Figure 2.12 illustrates the measured power computed using Eq. (2.50) as a function of supplied power (determined from electrical measurements of voltage and resistance). Note that these data should fall on a line with an intercept of 0.0 and a slope of 1.0; however the measured and supplied power do not correlate perfectly due to experimental error. Examination of Fig. 2.12 reveals that the uncertainty in the calorimetric measurements is nominally 0.75 W.

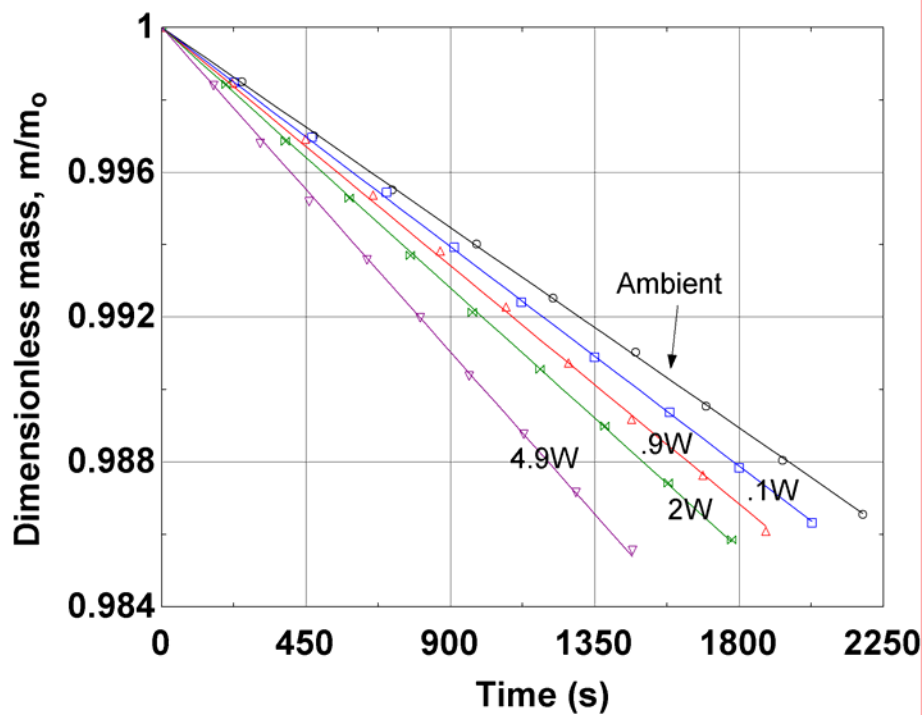


**Figure 2.11:** Dimensionless mass as a function of time for varying power inputs. The error for these data is 11%.

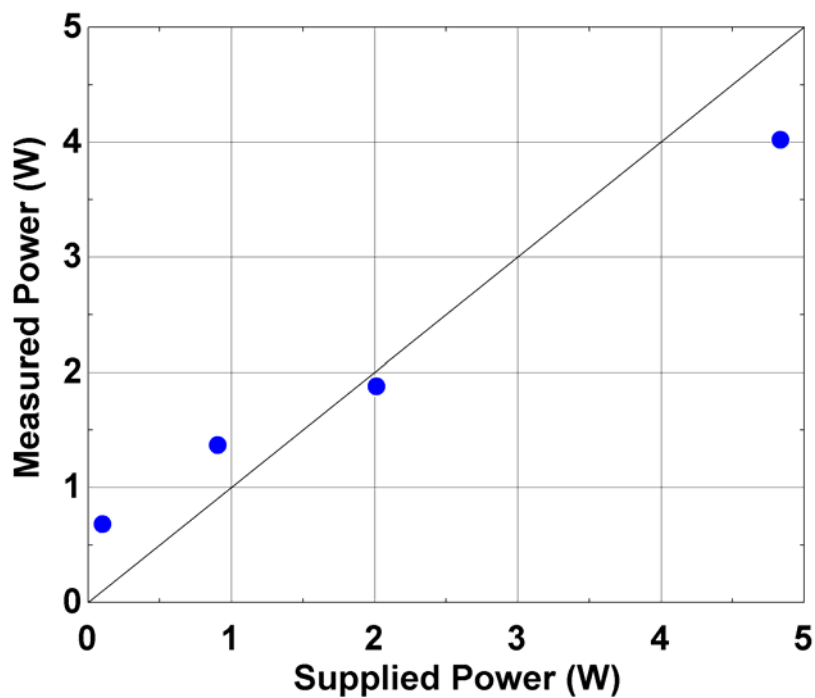


**Figure 2.12:** Calorimetric power measurement as a function of the electrically measured power. The data should be linear with a slope of 1.0 as shown with the solid line.

The data for the calorimetric experiment collected with the source activated and deactivated are shown in Fig. 2.13, together with best fit lines through these data. The change in the rate of mass loss between these conditions is nominally  $5.41\text{e-}7$  kg/s which corresponds to only 0.11 W of power carried by the source; this translates into an incident heat flux on the bundle of only  $100$   $\text{W/m}^2$  which is significantly less than the expected power of  $380$   $\text{W/m}^2$  based on specifications from the manufacturer (Oriol, 2004). Note that 0.11 W is on the same order as the previously identified uncertainty in the calorimetric measurement. However, even given the relatively large relative uncertainty in the calorimetric measurements, this low level of source power is significant and surprising. The energy output of the light source was subsequently also measured using a Newport 818T-150 detector and 1835-C power meter. These measurements are consistent with the calorimetric measurements (to within the experimental uncertainty) and indicated a nominal power of 0.19W.

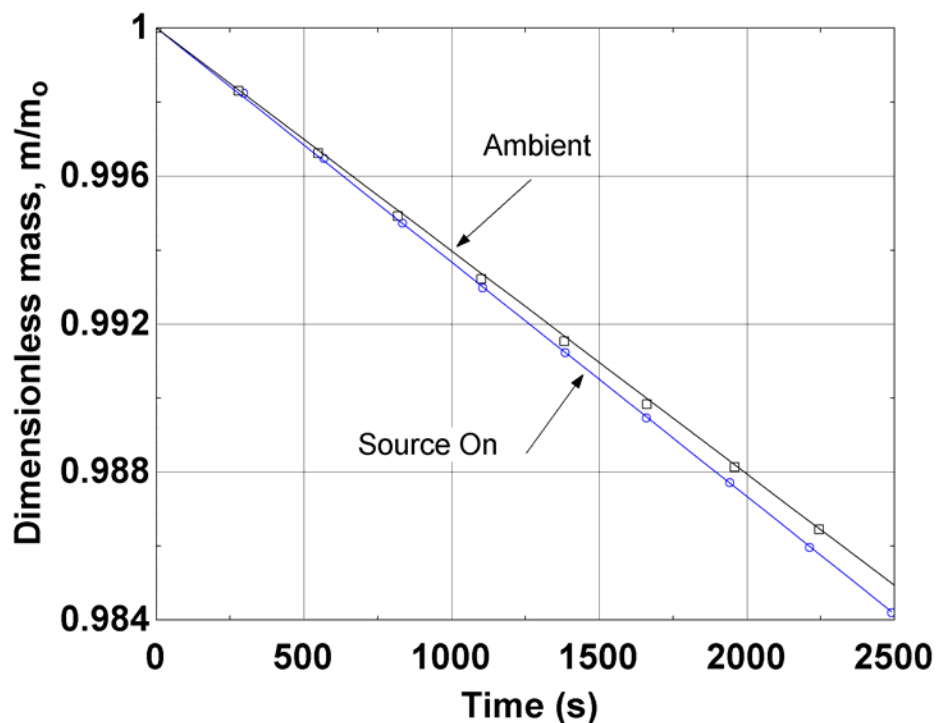


**Figure 2.13:** Dimensionless mass as function of time for the calorimetric measurement of the light source power prior to aligning the light source. Ambient refers to data taken at ambient conditions. Source On refers to data taken with the Oriel source activated and focused into the dewar. Error for ambient data is 5% and error for Source On data is 11%.

This experiment led to a diagnosis of the light source and it was eventually found that the light source was misaligned, thereby decreasing its nominal power output. The source has since been adjusted and the experiments were repeated; the results indicate a much higher intensity radiation. The data from the experiment carried out after alignment are plotted in Fig. 2.14 along with linear curve fits and the corresponding equations. The change in the rate of mass loss associated with Fig. 2.14 is  $1.64 \times 10^{-5}$  kg/s, which corresponds to a power of 3.3 W and a heat flux on the FOB face of  $3,100 \text{ W/m}^2$ . The source power was measured with the Newport detector to be  $2,960 \text{ W/m}^2$  at the FOB face. The consistency of these measurements, obtained from very

different instruments, suggests that  $3,000 \text{ W/m}^2$  is an accurate value of the incident flux and can be used with confidence for model validation and estimation of the thermal loading parameters.

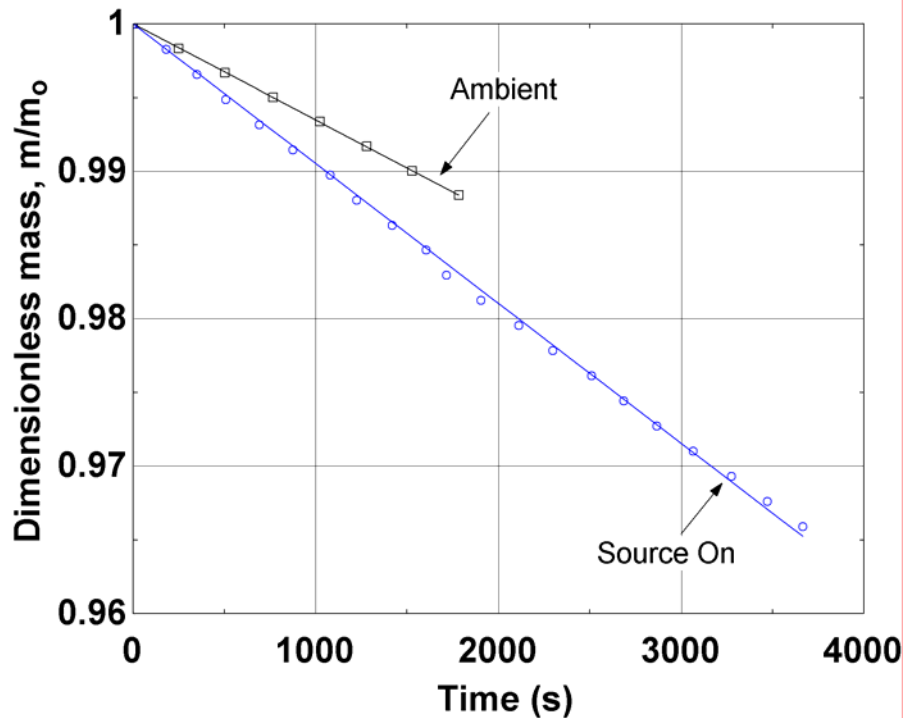


**Figure 2.14:** Dimensionless mass as function of time for calorimetric measurements taken with the aligned (high intensity) Oriel source. Ambient refers to data taken at ambient conditions. Source On refers to data taken with the Oriel source activated and focused into the dewar. Error for ambient data is 14% and error for Source On data is 5%.

### 2.5.5 Analytical Model for $L_{ch,\alpha}$

In this section, a very simplified geometry is used to obtain an analytical model that describes the thermal loading on the FOB due to radiation entering the pores. The actual geometry of the FOB (core, filling, and cladding) is very complex and three-dimensional (3-D); here, it is modeled by an equivalent, two-dimensional (2-D) medium. For this model it is assumed that the only absorbing medium in the composite structure is the cladding which is essentially true given the highly transparent nature of the filler (air) and the core (PMMA). As stated earlier, the fractional

change in energy through an absorbing medium (i.e. cladding) is given by the Bouguer-Lambert law, Eq. (2.51),

$$\frac{d\dot{q}}{\dot{q}} = -\alpha_{clad} ds \quad (2.51)$$

where  $\alpha_{clad}$ , a material property, is the absorption coefficient of the cladding and  $ds$  is a differential path length through the cladding. Integrating Eq. (2.51) yields,

$$\dot{q} = \phi_{pore} \dot{q}_{inc} e^{-\alpha_{clad} s} \quad (2.52)$$

where the product  $\phi_{pore} \dot{q}_{inc}$  is the energy incident on the pores of the FOB face and  $s$  is the path length through the cladding. The path that the light takes through the cladding must be related to the distance from the FOB face so that the thermal load can be expressed as a function of  $x$  in the 1-D model. The path length through the cladding is related to the net travel of the light in the axial direction of the equivalent medium,  $x$ , by Eq. (2.53):

$$s = \beta x \quad (2.53)$$

where  $\beta$  in this equation is defined as,

$$\beta \equiv \frac{s_{clad}}{x_o} \quad (2.54)$$

where  $s_{clad}$  is the path length through the cladding and  $x_o$  is a unit length in the  $x$  direction for a unit cell of the radiation trajectory. Figure 2.15 illustrates the trajectory of the radiation conceptually.

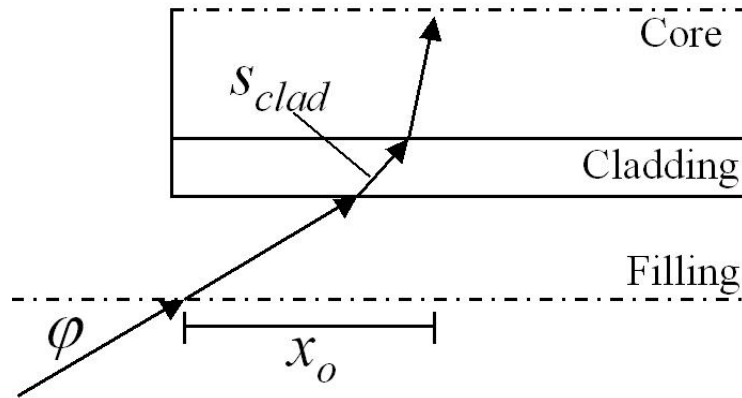


**Figure 2.15:** A unit cell of core, cladding, and filling. The light ray illustrates a typical path of light through the unit cell. The dotted lines represent perfectly reflecting boundary conditions used to take advantage of the assumed symmetry of the problem.

Substituting Eq. (2.53) into Eq. (2.52) yields,

$$\dot{q} = \phi_{pore} \dot{q}_{inc} e^{-\alpha_{clad} \beta x} \quad (2.55)$$

Equation (2.55) defines the energy transmitted through the FOB as a function of axial direction,  $x$ ; as this energy is absorbed it is deposited in the FOB as a volumetric heat generation. Figure 2.16 illustrates an energy balance for a differential cross-section of equivalent FOB medium.

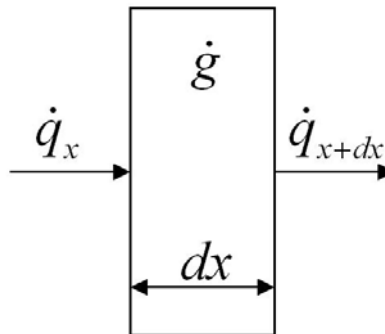


**Figure 2.16:** Energy balance for a differential cross-section of equivalent FOB medium:  $\dot{g}$  is the generation inside the medium due to absorption of  $\dot{q}_x$  by the cladding.

The energy balance associated with Fig. 2.16 is:

$$\dot{q}_x - \dot{q}_{x+dx} = \dot{g} \quad (2.56)$$

In terms of heat flux ( $\dot{q}''$ ) and volumetric heat generation ( $\dot{g}'''$ )

$$\dot{q}_x'' A_{bundle} - \dot{q}_{x+dx}'' A_{bundle} = \dot{g}''' A_{bundle} dx \quad (2.57)$$

Expanding terms using a Taylor series,

$$\dot{q}_x'' A_{bundle} - \left( \dot{q}_x'' + \frac{d\dot{q}''}{dx} dx \right) A_{bundle} = \dot{g}''' A_{bundle} dx \quad (2.58)$$

Canceling terms and dividing through by  $A_{bundle} dx$ ,

$$\dot{g}''' = -\frac{d\dot{q}''}{dx} \quad (2.59)$$

Taking the derivative of Eq. (2.55) and substituting into Eq. (2.59) gives an expression for the heat generation as a function of length in the equivalent medium.

$$\dot{g}''' = \alpha_{clad} \beta \phi_{pore} \dot{q}_{inc}'' e^{-\alpha_{clad} \beta x} \quad (2.60)$$

Substituting Eq. (2.15) into Eq. (2.60) yields,

$$\dot{g}''' = \alpha_{clad} \beta \dot{q}_{eff,\alpha}'' e^{-\alpha_{clad} \beta x} \quad (2.61)$$

Comparing Eq. (2.61) to Eq. (2.14) leads to Eq. (2.62),

$$L_{ch,\alpha} = \frac{1}{\alpha_{clad} \beta} \quad (2.62)$$

where  $L_{ch,\alpha}$ , as defined earlier, is the characteristic length due to the absorption of light entering the pores of the FOB face. In order to calculate  $L_{ch,\alpha}$ , the value of  $\alpha_{clad}$  was taken from Riedel and Castex (1999). The ratio  $\beta$ , however, depends on the angle of incidence of the radiation measured from normal ( $\varphi$ ). The incident light is distributed over a range of angles and therefore

an equivalent value,  $\beta_{eff}$ , is calculated by averaging over the angle distribution of the incident light.

Figure 2.17 shows how  $\beta$  varies with incidence angle,  $\varphi$ . Of particular interest is the region of  $\varphi$  from  $0^\circ$  to  $30^\circ$  as this corresponds to the likely range of incidence angles for both the experiment and a hybrid lighting system and therefore it is assumed that all of the incident radiation is within these limits. The precise distribution of radiation with incidence angle is not known; one possibility is a linear distribution, as shown in Fig. 2.18.

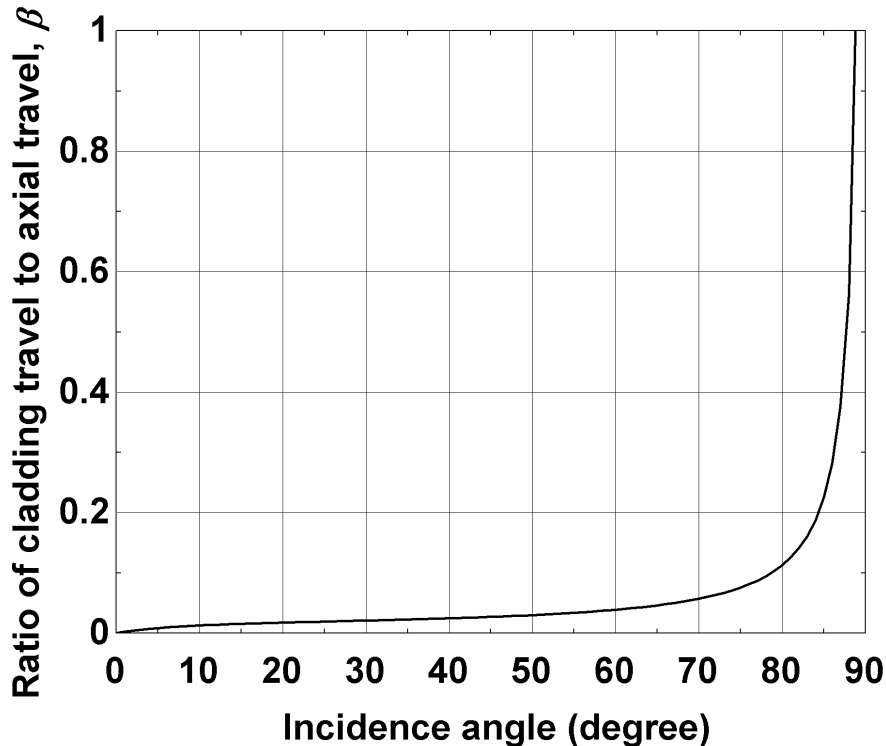


**Figure 2.17:** The ratio of the travel through the cladding to the axial travel of the light as a function of incidence angle.

Figure 2.19 shows the product of  $\beta$  and the fraction of the radiant energy ( $f$ ) based on the linear distribution shown in Fig. 2.18. An effective  $\beta$  can be calculated by integrating the  $\beta f$  curve:

$$\beta_{eff} = \int_{0^\circ}^{30^\circ} \beta f d\varphi \quad (2.63)$$

The  $\beta_{eff}$  associated with the linear distribution is found to be 0.0112; the characteristic length calculated from Eq. (2.62) is 5.96 cm.

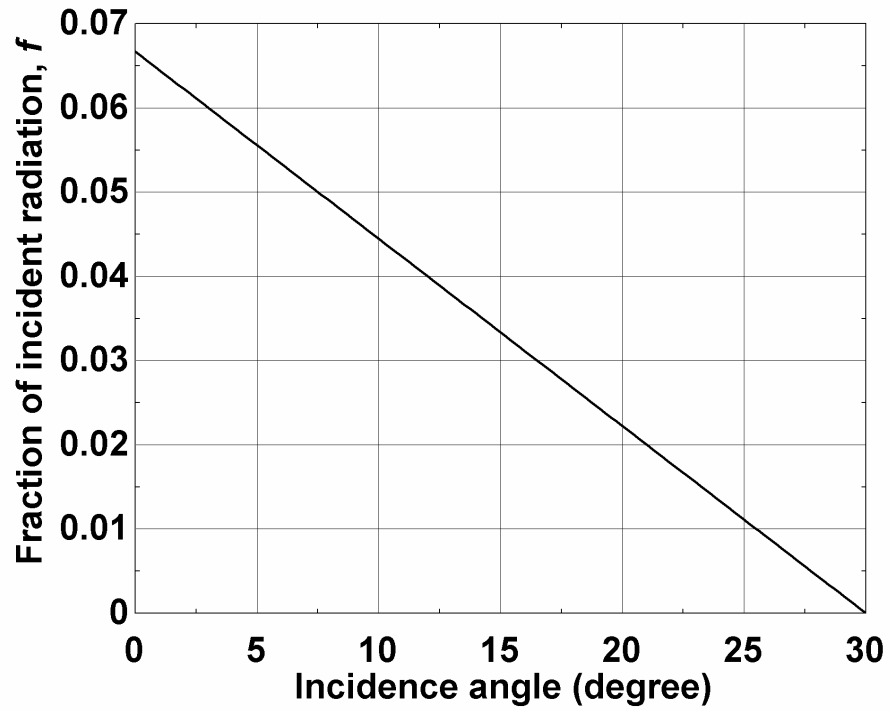


**Figure 2.18:** Fraction of radiant energy vs.  $\varphi$ .

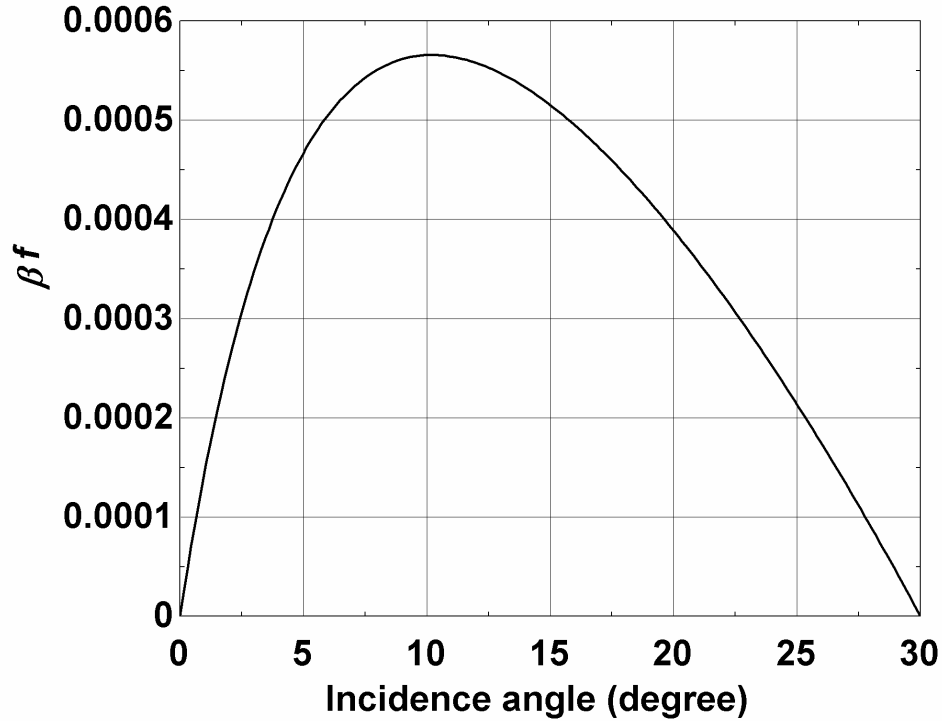


**Figure 2.19:** The product  $\beta f$  as a function of incidence angle,  $\varphi$ .

The model illustrated in Fig. 2.16 provides an upper bound on the heat generation within the FOB because it assumes that all of the radiation that is incident on the cladding surface is transmitted and none is reflected. Reflection can be incorporated into the model using the Fresnel relations, given as Eqs. (2.64), (2.65), and (2.66) by Duffie and Beckman (1991).

$$\rho_{\perp} = \frac{\sin^2(\varphi_2 - \varphi_1)}{\sin^2(\varphi_2 + \varphi_1)} \quad (2.64)$$

$$\rho_{\parallel} = \frac{\tan^2(\varphi_2 - \varphi_1)}{\tan^2(\varphi_2 + \varphi_1)} \quad (2.65)$$

$$\rho = \frac{1}{2}(\rho_{\perp} + \rho_{\parallel}) \quad (2.66)$$

Figure 2.20 illustrates how reflection can be incorporated into the model. Note that in Fig. 2.20, all of the reflected radiation is subsequently ignored and therefore this model provides a lower bound on the heat generation.

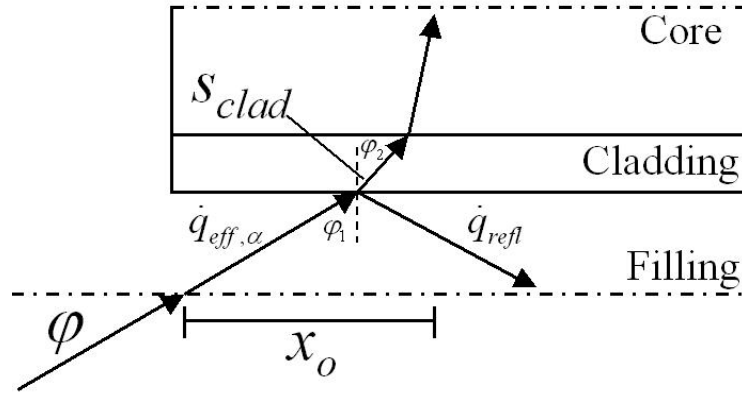


**Figure 2.20:** Illustration of reflection at air-cladding interface.

Incident energy,  $\dot{q}_{eff,\alpha}$ , is partially reflected,  $\dot{q}_{refl}$ , partially transmitted and partially absorbed.

The magnitude of the radiation transmitted through the filling-cladding interface is  $(1-\rho)\dot{q}_{eff,\alpha}$ .

By substituting this reduced value of  $\dot{q}$  into Eq. (2.52) and following the same derivation, an expression for heat generation in the FOB considering reflection (approximately) is obtained,

$$\dot{g}^m = \frac{\dot{q}_{eff,\alpha}''}{L_{ch,\alpha,\rho}} e^{-\frac{x}{L_{ch,\alpha,\rho}}} \quad (2.67)$$

where  $L_{ch,\alpha,\rho}$  is a the characteristic length taking into account reflection and is defined in Eq. (2.68).

$$L_{ch,\alpha} = \frac{1}{(1-\rho)\alpha_{clad}\beta} \quad (2.68)$$

Like  $\beta$ , the reflectivity  $\rho$  depends on the incidence angle  $\varphi$  and therefore an effective value is required for light that is distributed over a range of incidence angles. Figure 2.21 illustrates the the transmitted fraction of energy  $(1-\rho)$  varies with  $\varphi$ .

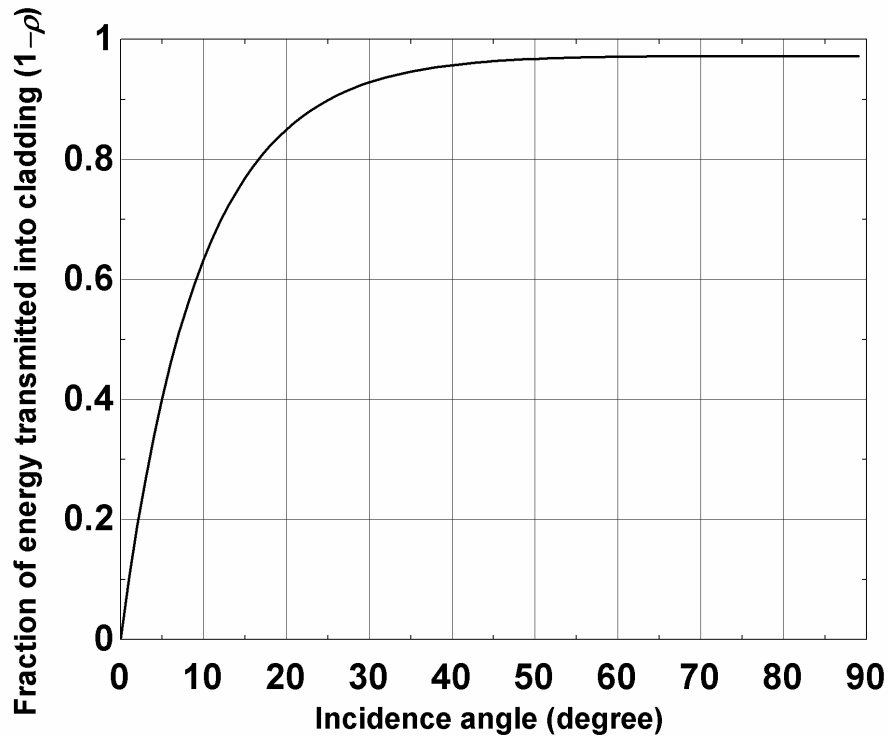
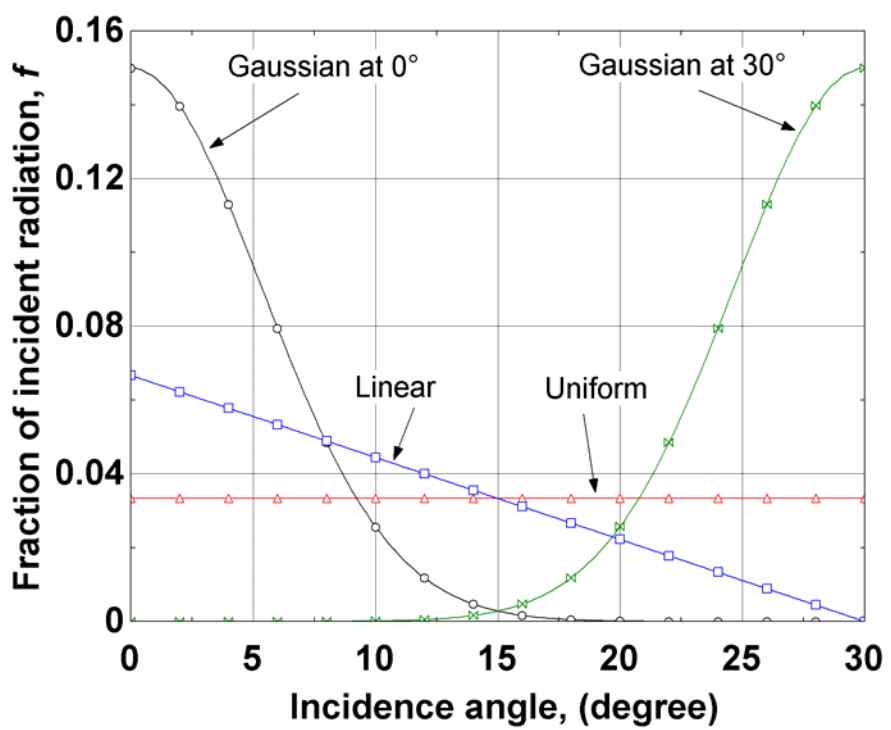


**Figure 2.21:** The fraction of transmitted energy ( $1-\rho$ ) as a function of the incidence angle,  $\varphi$ .

The equivalent ratio of the cladding path to the axial path considering the impact of reflectivity ( $\beta\rho_{eff}$ ) is 0.00742 for the linear distribution of incidence angle shown in Fig. 2.18. The characteristic length, including reflection is found to be 8.98 cm.

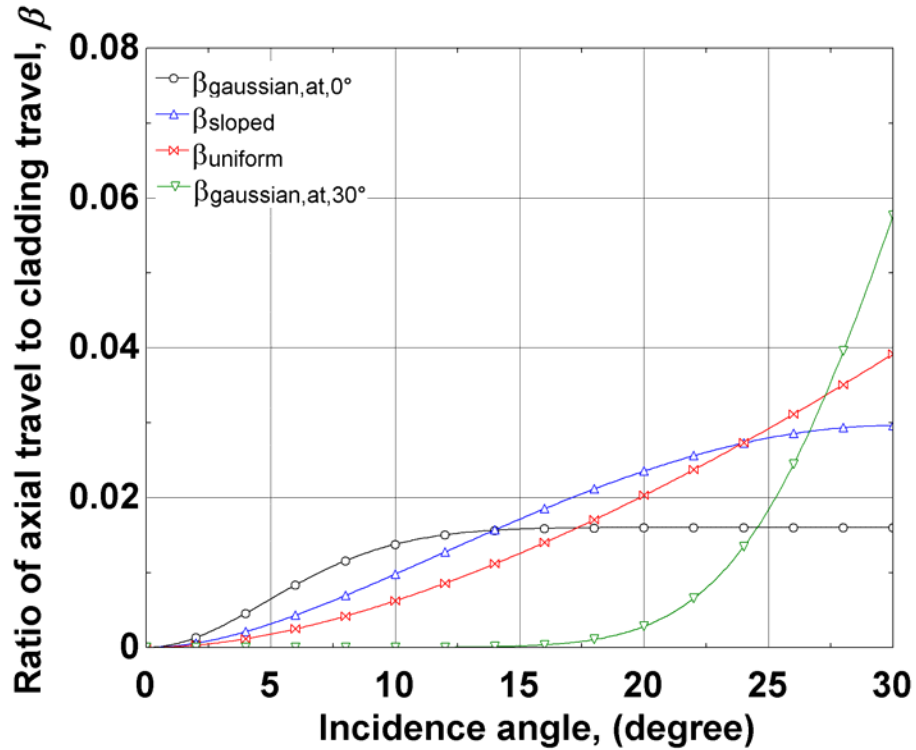
The actual angular distribution of the light used in the experiment is not known exactly. Therefore several different distributions were considered, in order to estimate the effect of the angular distribution on the heating effect within the FOB. These distributions are shown in Fig. 2.22 and include a Gaussian distribution that is centered about  $\varphi = 0^\circ$ , a linear distribution that becomes extinct at  $30^\circ$ , and a uniform distribution over all angles. A second Gaussian distributions centered about  $\varphi = 30^\circ$  was also considered; these two Gaussian curves were meant to represent the extremes that are possible while the linear and uniform distributions represent

intermediate cases. The integrated value for each curve from 0° to 30° is unity so that these functions can be applied directly to the thermal loading model in order to arrive at average values of the thermal loading coefficients.



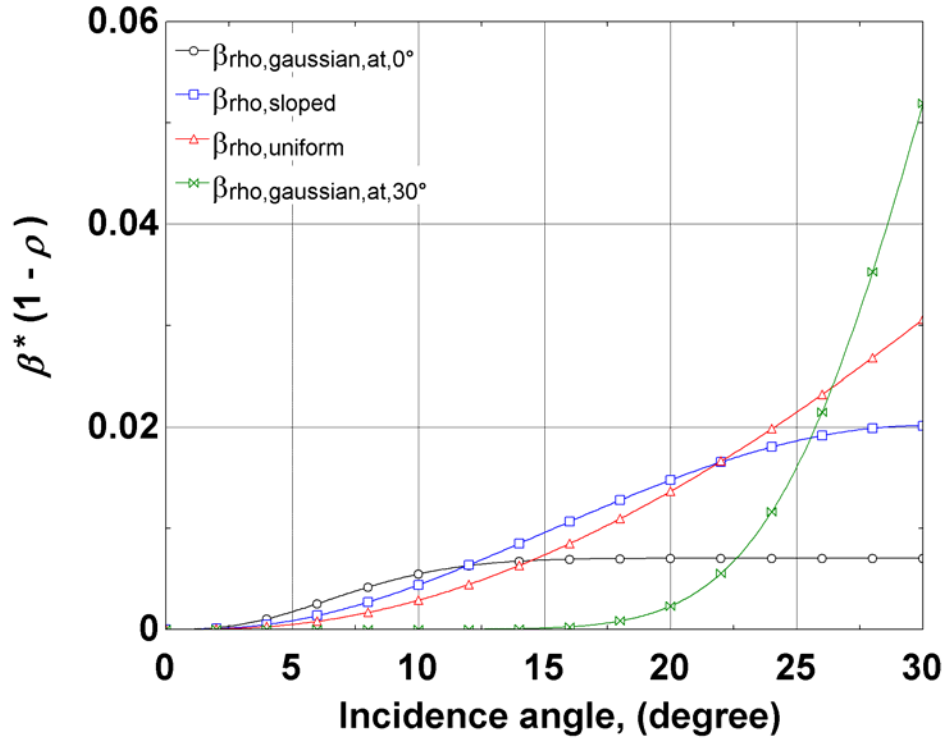
**Figure 2.22:** Fraction of incident radiation,  $f$ , as a function of incidence angle for several distributions of the incident radiation.

Figure 2.23 illustrates the value of  $\beta$ , the ratio of axial travel to the path length in the cladding, as a function of the incidence angle. The curves represent various effective  $\beta$  values ( $\beta_{eff}$ ) that have been weighted by the  $f$  functions shown in Figure 2.22 for the different distributions of incident radiation.



**Figure 2.23:** Ratio of axial travel to cladding travel,  $\beta$ , versus incidence angle. The curves plot the effective values of  $\beta$  for different distributions of incident radiation.

Figure 2.24 illustrate the value of  $\beta(1-\rho)$ , the product of the ratio of axial travel to cladding travel and the fraction of radiation transmitted into the cladding, as a function of incidence angle. The curves represent effective values of  $\beta(1-\rho)$  for the different distributions of incident radiation shown in Fig. 2.22. Integrated average values of  $\beta_{\text{eff}}$  and  $\beta \rho_{\text{eff}}$  for the distributions of Fig. 2.22 are given in Table 2.4. The purpose of considering non-reflecting and reflecting interfaces in the model (represented in Figs. 2.23 and 2.24, respectively) is to calculate upper and lower bounds on the amount of absorbed light within in the bundle. Each column of Table 2.4 represents a particular distribution and an upper and lower bound with regards to light absorption for that distribution.



**Figure 2.24:**  $\beta$  multiplied by the fraction of radiation transmitted into the cladding,  $(1-\rho)$ , versus incidence angle. The purple curve plots the nonweighted value of  $\beta(1-\rho)$  versus incidence angle. The remaining curves plot the effective values of  $\beta(1-\rho)$  for different distributions of incident radiation.

**Table 2.4:** Values of  $\beta_{eff}$  and  $\beta\rho_{eff}$  for different distributions of incident radiation. Also given are characteristic lengths for these values using an absorption coefficient of  $\alpha = 150/\text{mm}$ .

	Gaussian ( $0^\circ$ )	Sloped	Flat Line	Gaussian ( $30^\circ$ )
$\beta_{eff}$	0.00671	0.01119	0.0141	0.01945
$\beta\rho_{eff}$	0.00287	0.00742	0.01083	0.01754
$L_{ch,\beta_{eff}}$	99.3 mm	59.6 mm	47.3 mm	34.3 mm
$L_{ch,\beta\rho_{eff}}$	232.1 mm	89.8 mm	61.5 mm	38.0 mm

The results summarized in Table 2.4 can be used to estimate the characteristic length associated with the FOB pores. However, the 2-D model geometry is significantly simplified when compared to the actual 3-D geometry of the FOB. Also, the light distribution is unknown and the details of how the light actually travels through the FOB are not well-understood. A more

detailed 3-D model represents a complicated and time consuming exercise; the error associated with any results may still be significantly large due to the relatively poorly defined geometry of the FOB. Therefore, it was decided that the most effective means for estimating the characteristic length for the absorption of light within the powers was to infer the length using the 1-D model together with experimental data. These data and the resulting calculation are described in Chapter 3.

## 2.6 Parametric Studies

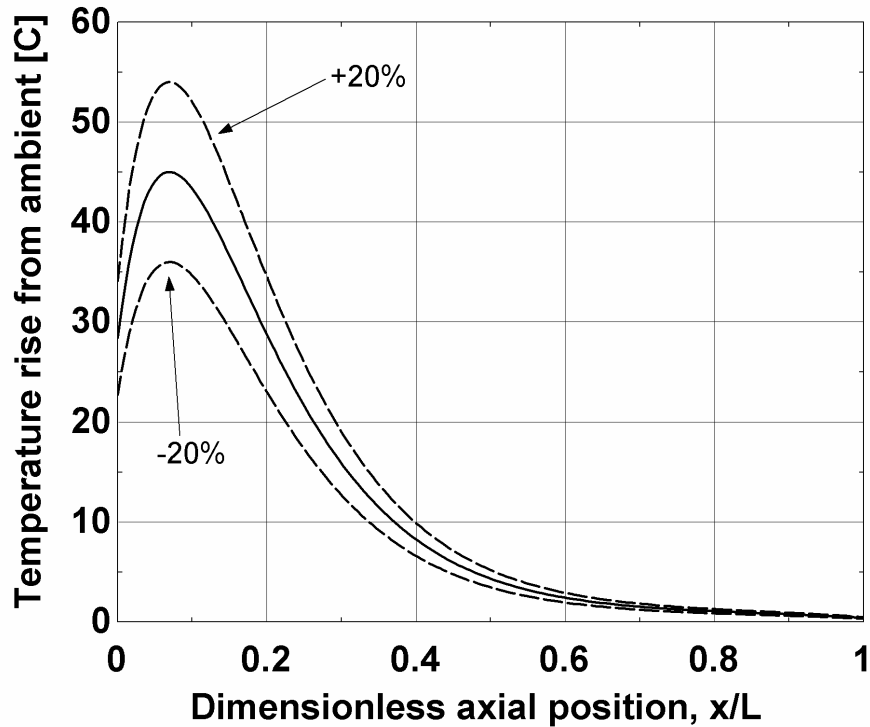
Figures 2.25 through 2.28 show the results of a parametric study using the EES 1-D model. The four parameters used for this study are the incident heat flux, the effective heat transfer coefficients on the front face and edge, as well as the characteristic length associated with the pores. Nominal values for these parameters are listed in Table 2.5.

**Table 2.5:** Description and value of the parameters used for study.

<b>Description</b>	<b>Parameter</b>	<b>Value</b>
Heat flux incident on FOB face	$\dot{q}_{inc}''$	3000 W/m <sup>2</sup>
Convection coefficient from front face of FOB	$h_{ff}$	10.5 W/m <sup>2</sup> -K
Convection coefficient from edge of FOB	$h_{edge}$	1.1 W/m <sup>2</sup> -K
Characteristic length associated with pores*	$L_{ch,\alpha}$	0.026 m

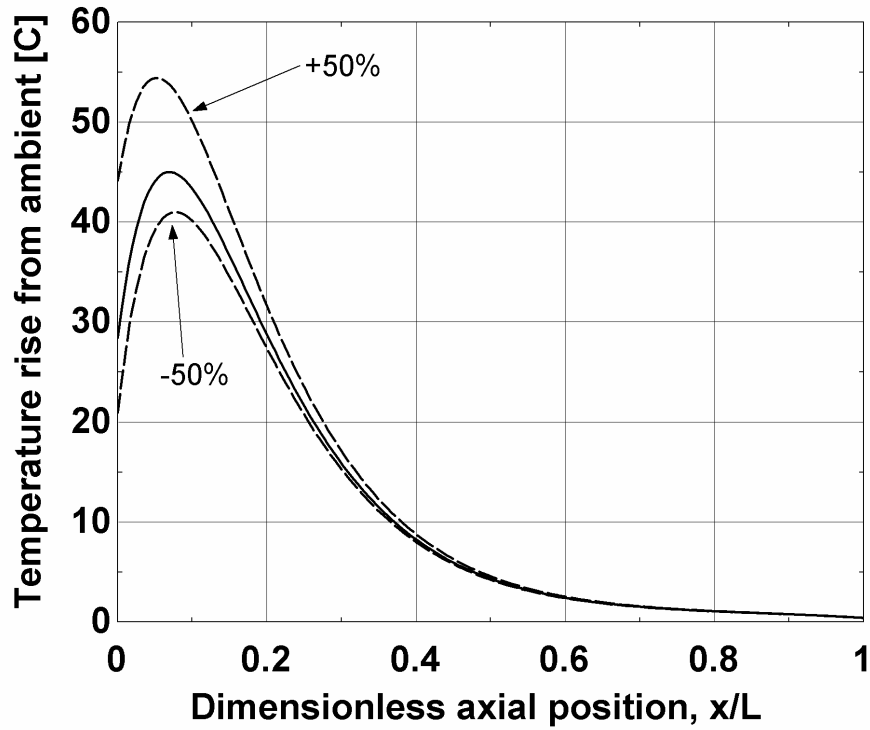
\*The calculation of this value is described in Chapter 3

Figure 2.25 shows the affect of a  $\pm 20\%$  change in the incident heat flux. The primary affect of varying the incident heat flux is a change in the magnitude of the peak temperature in the FOB. The overall shape of the curve remains the same.



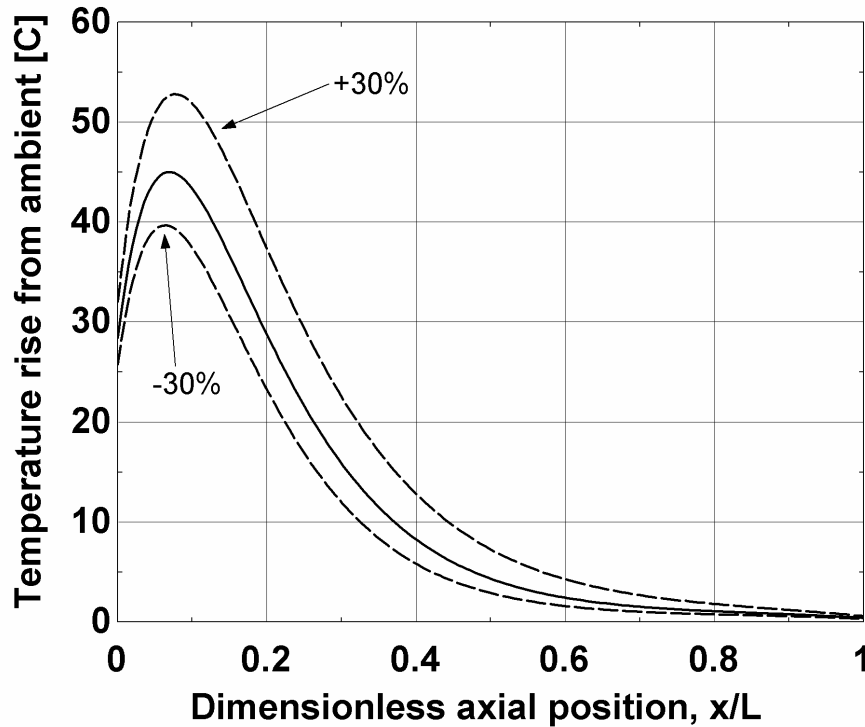
**Figure 2.25:** Temperature distribution in FOB for nominal conditions and values of  $\dot{q}_{inc}'' = \pm 20\%$ .

Figure 2.26 shows the affect of a  $\pm 50\%$  change in the heat transfer coefficient on the front face. Varying the front face heat transfer coefficient not only affects the magnitude of the peak temperature, but also the location of the peak temperature along the axis of the FOB. Note that a relatively large change in the heat transfer coefficient is needed to affect the temperature distribution significantly.



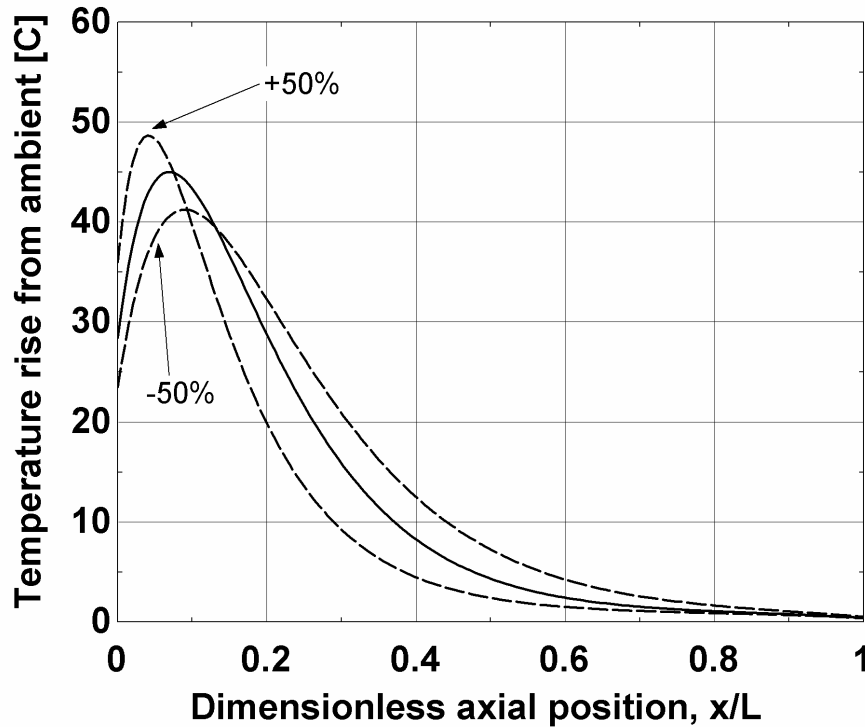
**Figure 2.26:** Temperature distribution in FOB for nominal conditions and values of  $h_{ff} = \pm 50\%$ .

Figure 2.27 shows the affect of a  $\pm 30\%$  change in the heat transfer coefficient on the edge of the FOB. As with the incident heat flux, the heat transfer coefficient at the edge affects only the magnitude of the peak temperature and does not change the location of the peak significantly.



**Figure 2.27:** Temperature distribution in FOB for nominal conditions and values of  $h_{edge} = \pm 30\%$ .

Figure 2.28 shows the affect of a  $\pm 50\%$  change in the characteristic length associated with the pores. Notice that varying the characteristic length associated with the pores affects both the magnitude of the peak temperature as well as the location of the peak temperature along the axis of the FOB.



**Figure 2.28:** Temperature distribution in FOB for nominal conditions and values of  $L_{ch,\alpha} = \pm 50\%$ .

## 2.7 Conclusions

The focus of this chapter was the development of a 1-D model of the FOB as well as a careful evaluation of the values that are required to simulate the experimental FOB. It was shown that the primary load on the FOB is related to the absorption of the radiation that is incident on the pores of the FOB. A simple model of this absorption process was developed and showed that the energy generation due to light absorption could be quantified with a characteristic length. A very simplified 2-D model of the pore structure was used to estimate the characteristic length; however, very restrictive assumptions were involved with the simplified model and therefore it was clear that a more accurate estimate of the characteristic length could be determined by comparing 1-D model results with experimental data. Chapter 3 details the experimental work and describes the calculation of this characteristic length.

## Chapter 3

# Experimental Setup

### 3.1 Introduction

The purpose of this chapter is to describe the experiments that were carried out on the fiber optic bundle (FOB). This research involved two experimental setups, one at Oak Ridge National Laboratory (ORNL) and the other at the University of Wisconsin-Madison. The initial experiments were carried out at ORNL and were in some ways unsuccessful as they did not contribute directly to the development of the final FOB model. However, these experiments did provide valuable insights that eventually resulted in more refined and successful experiments. The final section of the chapter utilizes the experimental results in conjunction with 1-D model in order to infer the characteristic length associated with the light absorption in the pores of the FOB and therefore provide a useful model of the thermal loading within the FOB.

### 3.2 Experimental Setup at Oak Ridge National Laboratory

#### 3.2.1 Experimental design

The motivation for studying the FOB is related to the observed thermal failure of these components when placed in on-sun operating conditions. Initial research into the thermal failure of the FOB took place at Oak Ridge National Laboratory and revealed that small amounts of debris in the interstitial regions of the FOB face were absorbing radiation and resulting in a thermal load within the FOB. By removing some of this debris, the FOB was able to remain on-

sun for extended periods of time (on the order of weeks) without melting. However, this work did not result in a clear understanding or model of the bundle heating process. Therefore, additional experiments were designed in order to expand upon this initial research with the objective of developing a predictive thermal model of the FOB. Figure 3.1 shows the laboratory setup that was used to simulate on-sun conditions at ORNL.

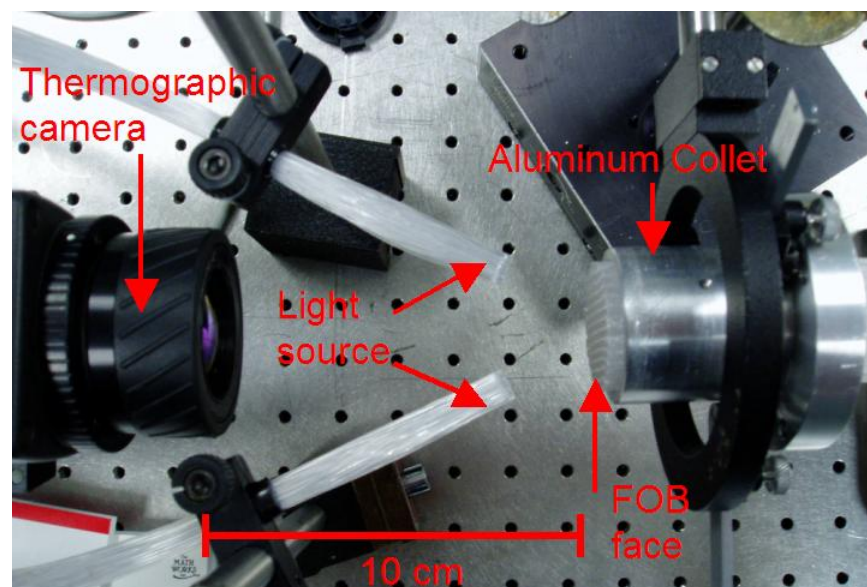


**Figure 3.1:** Laboratory setup at ORNL to simulate on-sun conditions.

The setup consisted of a Cogent light source, a Thermovision A20 thermographic camera made by FLIR Systems, and the FOB held in an aluminum collet. The light source was focused onto the face of the FOB by two bundles of small diameter fiber optic cable. The spectrum of the light source is shown in Fig. 3.2. The data for this source were taken at ORNL with an integrating sphere and spectrometer. The objective of the experimental was to measure the temperature distribution across the face of the FOB and collet using the thermographic camera under the thermal load provided by the Cogent light source for various FOB configurations (described below). The next section describes the experimental FOB's that were fabricated for these tests.

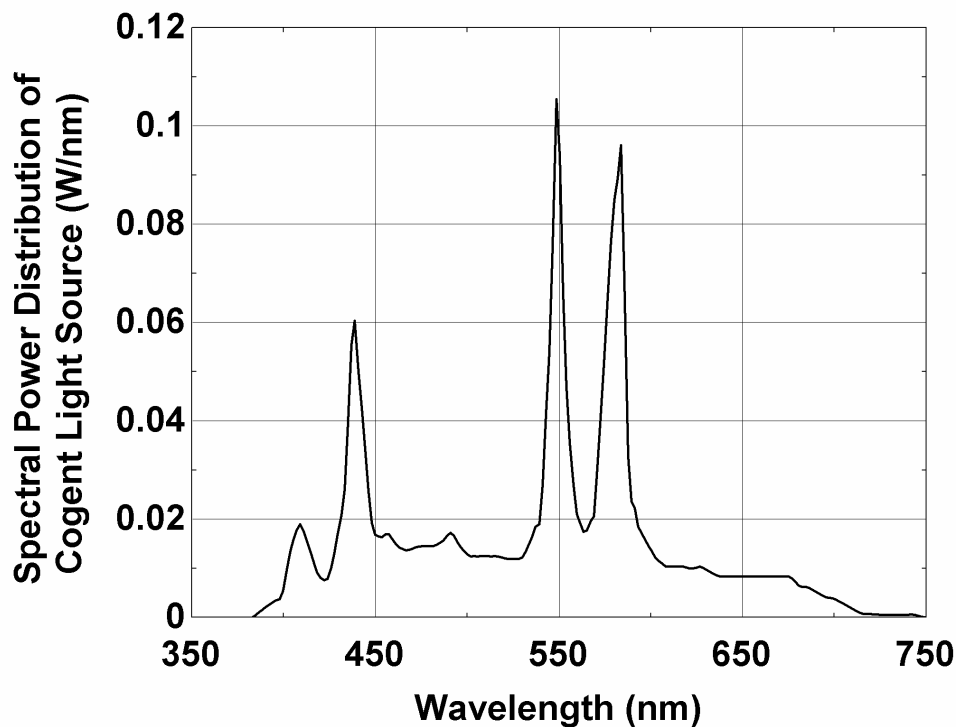


**Figure 3.2:** Spectral power distribution (SPD) of the Cogent light source. Integrated over all wavelengths, the light source yields a total heat flux at the FOB face of  $5609 \text{ W/m}^2$ . Data were taken at ORNL with an integrating sphere and spectrometer.

### 3.2.2 FOB construction

Fiber optic bundles for the experiment were constructed by recycling unused fibers from previous bundles. Two methods of bundle construction were used. The first method consisted of gathering a number of fibers together, fitting them snugly into a collet and then simultaneously polishing the exposed face of the resulting FOB. The second method consisted of polishing each fiber individually and then putting the fibers together and fitting them snugly into a collet. The number of fibers varied from  $N=120$  to  $N=127$  depending on the inner collet diameter. During the polishing process, some of the excised material from the cladding and fibers becomes trapped in the interstitial region between the fibers. As noted earlier, these contaminant particles, along with other forms of contamination, are believed to contribute to the

thermal load on the FOB by absorbing incident radiation. Photographs of FOB's that were polished using both methods are shown in Fig. 3.2.

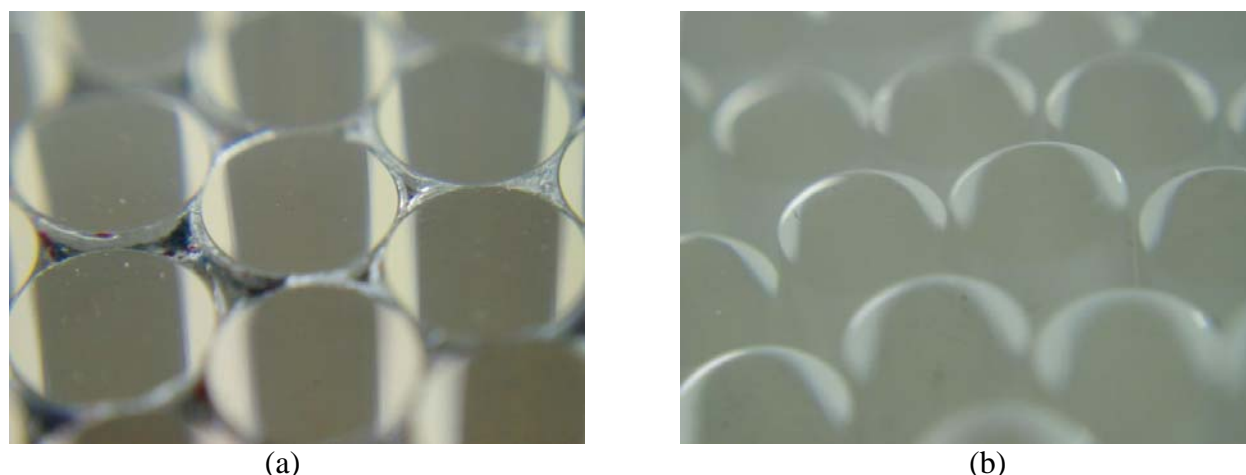


**Figure 3.3:** Photographs of (a) a FOB polished using method 1 (all fibers polished in a single, final operation) and (b) a FOB polished using method 2 (each fiber polished individually); note the hanging debris around the edges of the individual fibers that results from method 1 whereas there is no debris around the edge of the individual fibers for method 2.

Several different FOB configurations were built and tested at ORNL. The types of FOB's can be divided into two categories (as discussed above): FOB's whose fibers were collectively polished and FOB's whose fibers were individually polished. There were two different FOB's whose fibers were collectively polished: a FOB whose pores were partially filled with excised material from the polishing process and a FOB whose pores were filled with aluminum foil, Fig. 3.4. There were three different FOB's whose fibers were individually polished: a FOB with no collet, a FOB with an aluminum collet, and a FOB with an acrylic collet, Fig. 3.5. The FOB's were designed with the intent that these very different configurations would produce different temperature distributions at the front face of the FOB and this would provide some insight into the heating process. Because of various problems with these experiments, described below, only the results for the FOB with an aluminum collet are presented.

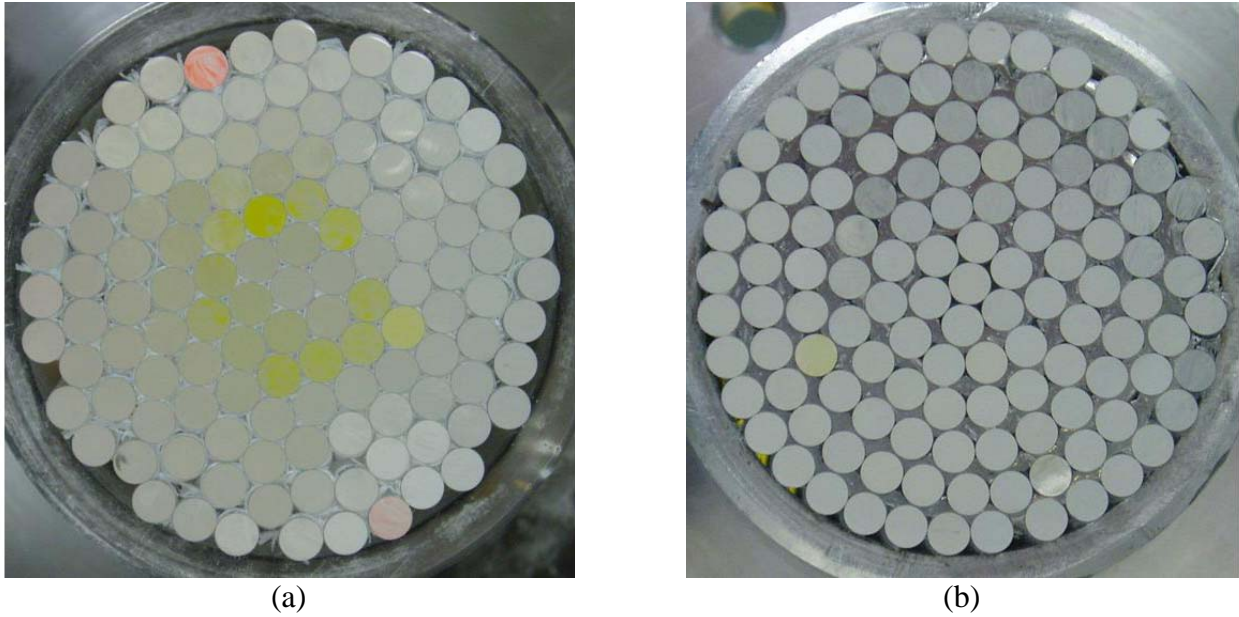


**Figure 3.4:** (a) Image of a FOB whose pores were partially filled with excised material from the polishing process and (b) image of a FOB whose pores were filled with aluminum foil. Note: the yellow and orange color appearing in some of the individual fiber optic cables of the bundle is light transmitted through the rear face, coming from the cable ties that are holding the FOB together.



**Figure 3.5:** (a) Image of an FOB with an acrylic collet and (b) image of an FOB with an aluminum collet. Note, the FOB with no collet is not shown.

### 3.2.3 Experimental measurements

Experimental data were taken in the following manner. The FOB with an aluminum collet was allowed to equilibrate to room temperature before being exposed to the Cogent light source for a period of 30 minutes (1800 s). The temperature rise on the FOB face was calculated over this time period by subtracting the temperature at time = 0 s (i.e., room temperature) from the temperature at time = 1800 s. The software provided for the thermographic camera has the ability to measure the temperature at an individual spot or to calculate an average temperature associated with a number of spots that are defined by an area. Single spot temperature data for this FOB were taken at the outer edge and center of the FOB, as illustrated in Fig. 3.6 which shows two images of the front face of the FOB. Figure 3.6(a) was taken with the thermographic camera while Fig. 3.6(b) was taken with a digital camera. The colors on the thermographic image correspond to measured temperatures (scale not shown). The FOB in Fig. 3.6(a) was at room temperature when the image was taken. The measured temperature as a function of time is shown in Fig. 3.7 at the two locations indicated in Fig. 3.6; Fig. 3.8 shows a sequence of thermographic images obtained during the experiment.

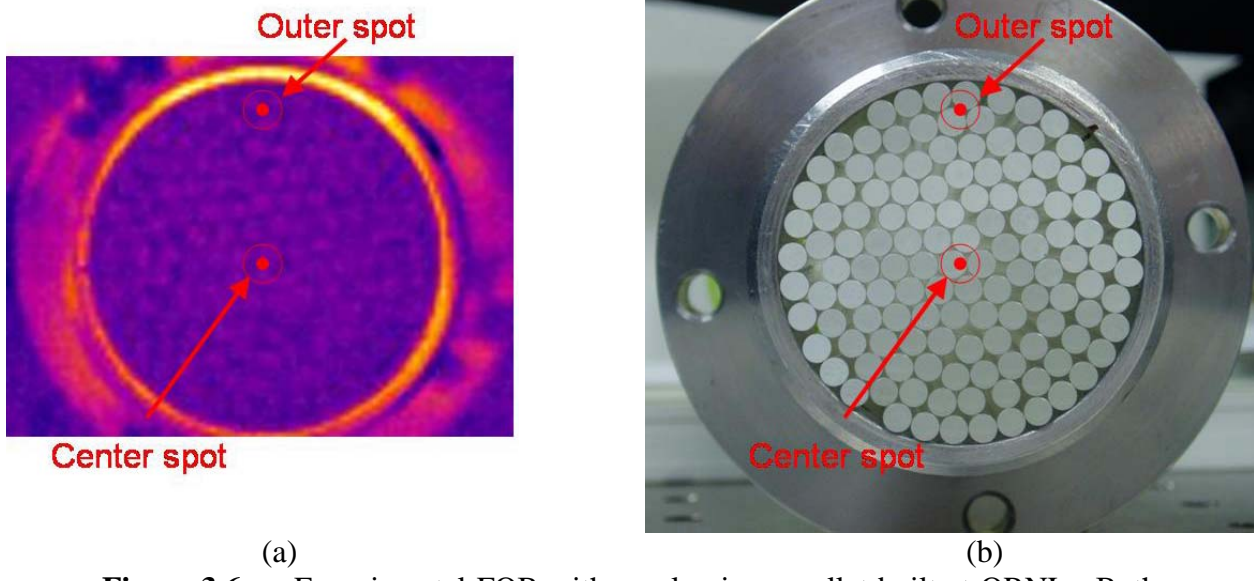


**Figure 3.6:** Experimental FOB with an aluminum collet built at ORNL. Both images show temperature measurement locations. The images are taken with (a) a thermographic camera and (b) a digital camera.

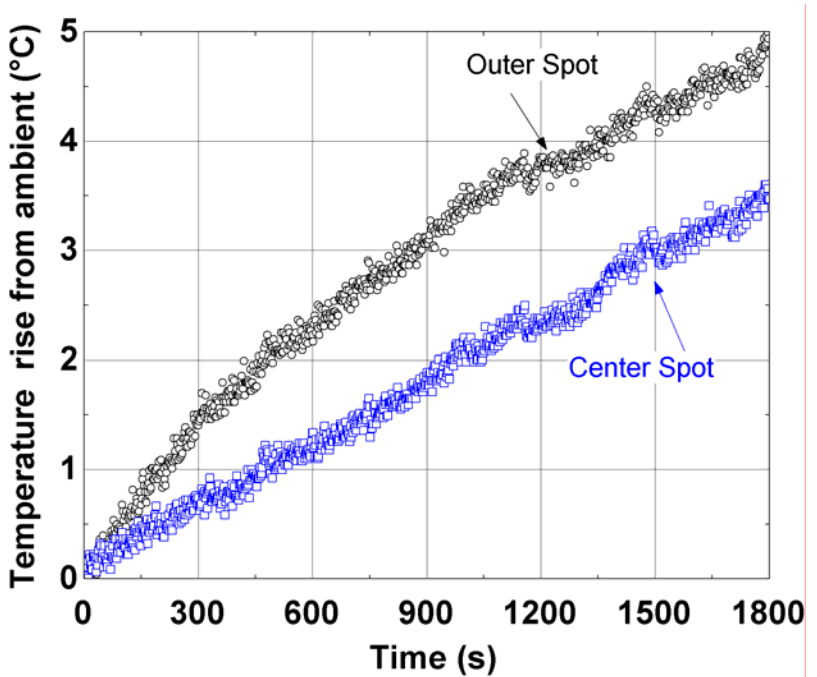


**Figure 3.7:** Temperature rise from ambient as a function of time for the ORNL experimental FOB shown in Fig. 3.4; this FOB has individually polished fibers and an aluminum collet.

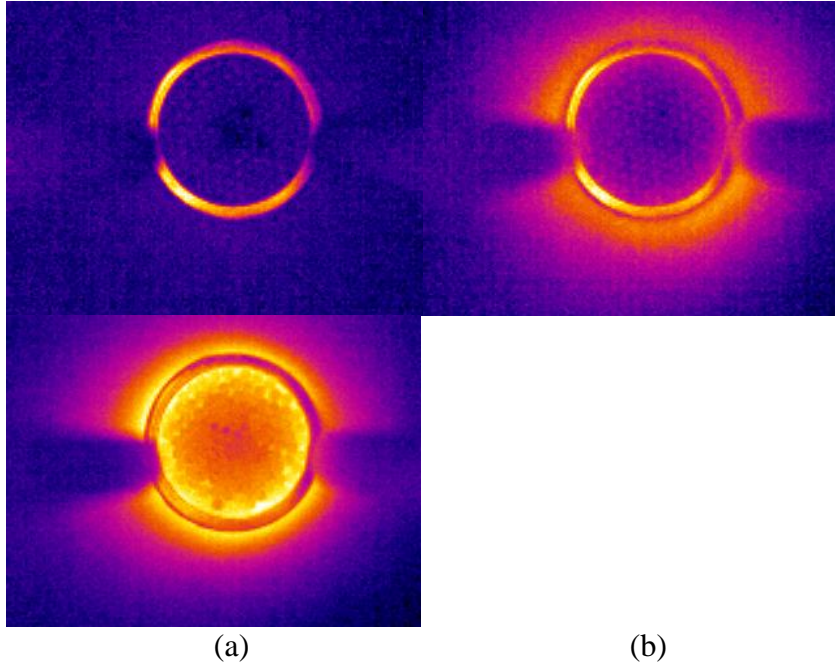


**Figure 3.8:** Heating sequence for the aluminum-collet FOB. The sequence is (a) before the light source is activated, (b) just after the light source is activated and (c) after approximately 15 minutes after the light source is activated.

The experiments revealed that the FOB with an aluminum collet experienced a higher temperature rise at its front face than the FOB with an acrylic collet, which experienced a higher temperature rise than the FOB with no collet; however, there were several problems with the experimental setup. First, the experiments did not reach steady state. Second, the thermographic camera could only measure temperatures at the surface of the FOB; there was no way of knowing the temperature distribution inside the FOB. In addition, the temperature measurements from the thermographic camera depend on the emissivity of the object being measured. In particular, the aluminum collet of the FOB reported consistently higher temperatures (approximately  $3^{\circ}\text{C}$ ) than the face of the FOB even when the entire FOB/collet assembly had equilibrated with room temperature, as can be seen in Fig. 3.6(a). Finally, the thermographic camera required an unobstructed view the front face of the FOB and therefore the light source

could not be directly focused on the face. This limitation can be seen in Fig. 3.1 where the fiber optic cables coming from the Cogent light source and delivering light to the face of the FOB are not perpendicular to the FOB face. As a result of this limitation, some of the incident light fell directly on the aluminum collet and this possibly contributed to another load on the FOB via light absorption on the collet. Because of these complications a new, more refined experimental design was implemented at the University of Wisconsin-Madison.

### **3.3 Experimental Setup at the University of Wisconsin-Madison**

#### **3.3.1 Purpose**

The primary purpose of conducting experimental work on the FOB was to aid in the development of a predictive thermal model. The dominant thermal load on the FOB was recognized to be heat generation due to light absorption within the FOB. Therefore the experimental setup was designed to measure the temperature distribution within the FOB so that the resultant experimental data could be compared with predictions from the 1-D model developed in Chapter 2. Ultimately, this comparison lead to an inferred measurement of the characteristic length associated with light absorption in the pores and therefore a useful model of the thermal loading on the FOB. There were two experiments setup at the University of Wisconsin-Madison. Both are described below.

#### **3.3.2 Experimental Setup #1**

The purpose of experimental setup #1 was to measure the temperature distribution within the FOB when exposed to a collimated, uniform intensity beam of light. The temperature

measurements were accomplished using type E thermocouples rather than via a thermographic camera (as was used at ORNL). Several, very fine gage (34 AWG) type E thermocouples were installed in a FOB built at ORNL (Fig. 3.9); one group of thermocouples, shown as grey points in Fig. 3.9, was placed at the face of the FOB at various radial positions while a second group, shown as black points in Fig. 3.9, was placed at a uniform depth, approximately 2.5 cm, within the FOB at similar radial locations to the surface group. The FOB was exposed to light provided by an Oriel 87436, 500W mercury lamp and data were recorded using a data acquisition system until a thermal steady state was observed. This experimental setup was designed to address the questions that arose from previous experiments at ORNL regarding the nature of the FOB heating. Of particular interest was the temperature distribution within the FOB as well as the steady state temperatures at various locations at the front face of the FOB.

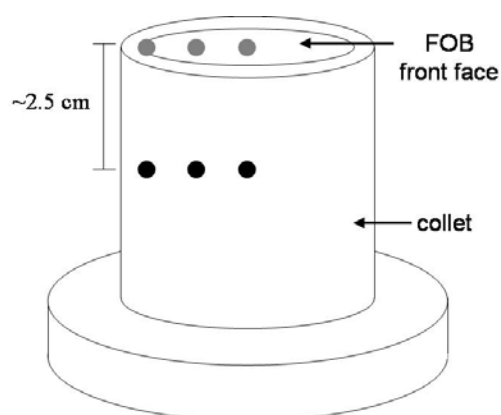


**Figure 3.9:** Collet and thermocouple orientation for experimental setup #1. Three thermocouples, shown in grey, are placed at the surface of the FOB with three more thermocouples, shown in black, placed at corresponding radial positions approximately 2.5 cm below the FOB surface.

The light source provided a collimated, uniform intensity beam as shown schematically in Figure 3.10.

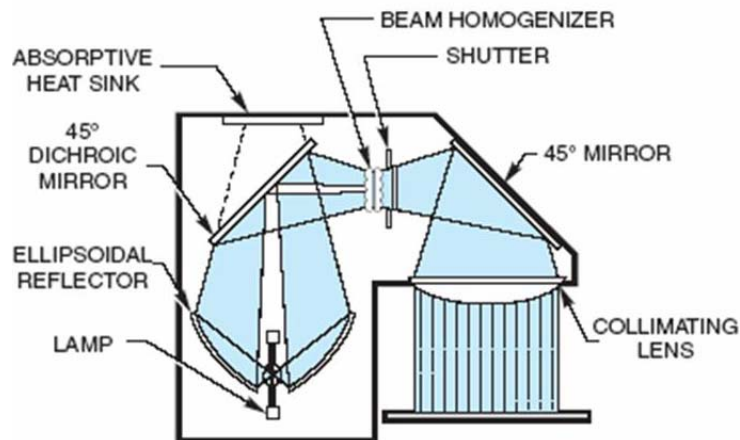


**Figure 3.10:** Schematic of the Oriel 500W mercury arc lamp (Oriel, 2004).

The light generated by the mercury arc lamp is first collected by an ellipsoidal mirror and then reflected by a 45° dichroic. The dichroic reflects in the wavelength region 350 - 450 nm. The light then passes through the beam homogenizer and is reflected by another 45° mirror. The spectral transmission of this mirror is high for all wavelengths. After this 45° mirror the light passes through the collimating lens to the working plane. The spot size of the beam at the working plane is a 6 inch (152 mm) square. The integrated intensity of the light at the working plane is designed to be 380 W/m<sup>2</sup>. A spectral graph of the light produced by the source is shown in Figure 3.11.

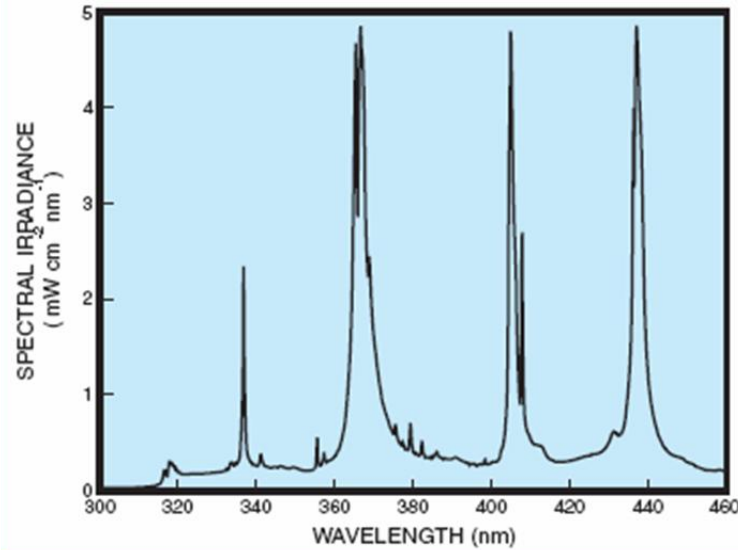


**Figure 3.11:** Spectral power distribution of the 500W mercury arc lamp (Oriel, 2004).

The light source provides a uniform intensity and well-collimated beam; however, the spot size is larger than the face of the FOB. Therefore, two Fresnel lenses are used to concentrate the energy and reduce the spot size so that its size coincides with the size of the FOB face. The first lens is placed just before the collimating lens in the housing of the arc lamp for ease of mounting. The second is placed after another 45° reflector, which aligns the beam so that it is parallel to the working plane. A schematic of the optical setup is shown in Fig. 3.12. After the second Fresnel lens, the light forms a circular spot with a diameter that is just slightly less than the inner diameter of the collet.

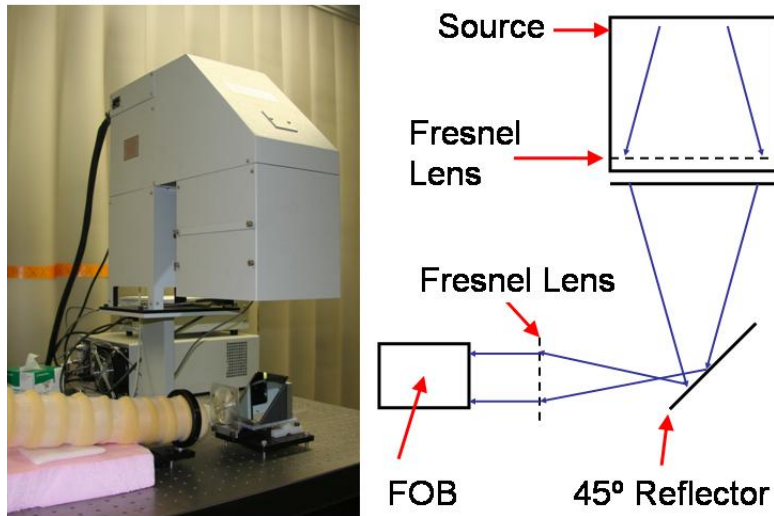


**Figure 3.12:** Schematic of experimental setup. The end result is a collimated, uniform intensity beam with a circular shape that is matched to the ID of the collet.

Measurements of the power of the source are described in the Chapter 2. For experimental setup #1 at Madison, the light was mis-aligned and therefore the source output corresponded to that shown in Fig. 2.13 which is considerably reduced from its design output. The reduced source output corresponds to approximately  $100 \text{ W/m}^2$  on the face of the FOB.

Figure 3.13 is a plot of the temperature recorded by all of the thermocouples when the face of the experimental FOB is exposed to the light source. The solid curves are data for the thermocouples at the face of the FOB. The dashed curves are data for the thermocouples at a distance 2.5 cm from the FOB face. The curves are further distinguished by their radial location, which is also indicated on the plot. The highest temperatures are recorded at the FOB center on the face and the temperatures tend to decrease in both the radial and axial directions.

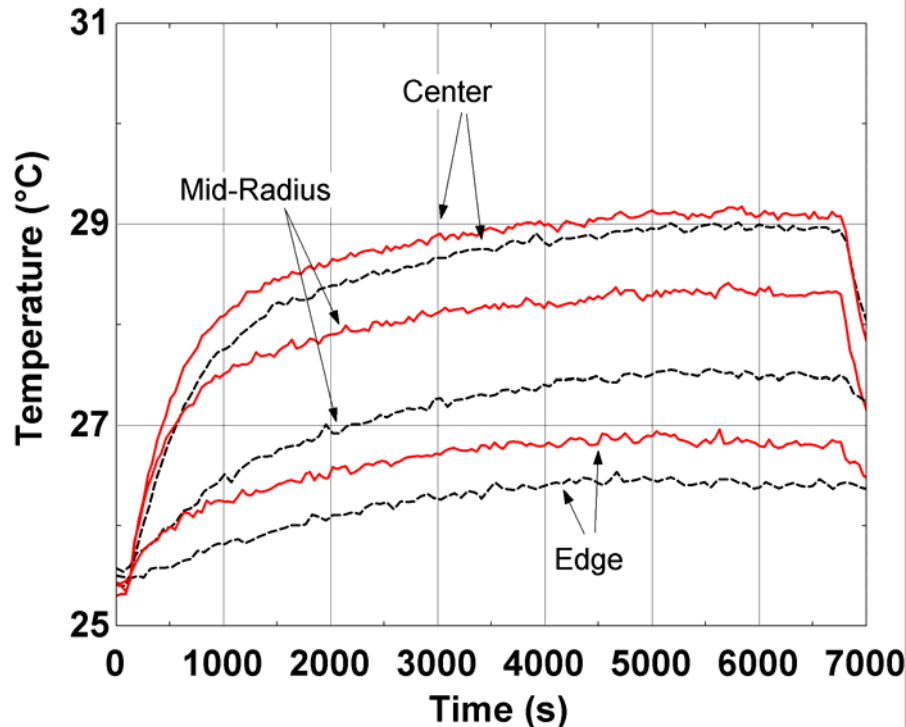


**Figure 3.13:** Temperature measurements recorded at the surface and inside the FOB. Note the highest temperature is recorded on the face of the FOB at the radial center. Temperatures decrease in both the radial and axial directions.

The results of this initial experiment met the goal of measuring the temperature distribution within the FOB; however, they indicate that the FOB has a very two-dimensional temperature distribution under the mounting conditions used for experimental setup #1. In order to facilitate the development of a 1-D analytical model, the experiment was modified in order to reduce the temperature gradients in the radial direction (i.e. from center to mid-radius to edge). In addition, the temperature distribution within the FOB measured for experimental setup #1 was not sufficiently spatially resolved in the axial direction (i.e. more thermocouples are needed for a more detailed profile that would provide a clearer picture of the thermal loading profile).

### 3.3.3 Experimental Setup #2

Two improvements were required relative to experimental setup #1: increase the spatial resolution of the measured temperature distribution in the axial direction and modify the external conditions so that the temperature distribution within the FOB was more 1-D. Measurements of the temperature distribution within the FOB for experimental setup #2 were accomplished by instrumenting the FOB with thermocouples that are precisely mounted at several axial locations along its length. The thermocouples were attached to two individual fibers in the FOB, one fiber at the center and the other at a mid-radius location that is approximately halfway between the center and the edge of the FOB; these two radial locations were chosen to quantify the one-dimensionality of the temperature distribution. Approximate thermocouple placement is illustrated in Fig. 3.14. The thermocouples have an increased spatial resolution near the front face of the FOB, the size of this region of increased resolution was based on previous estimations of the characteristic length associated with the pores (on the order of cm as discussed in Chapter 2). Photographs of the individual fibers with attached thermocouples are shown in Fig. 3.15. Note in Fig. 3.15 that only the first 6 thermocouples of a total of 13 are shown.

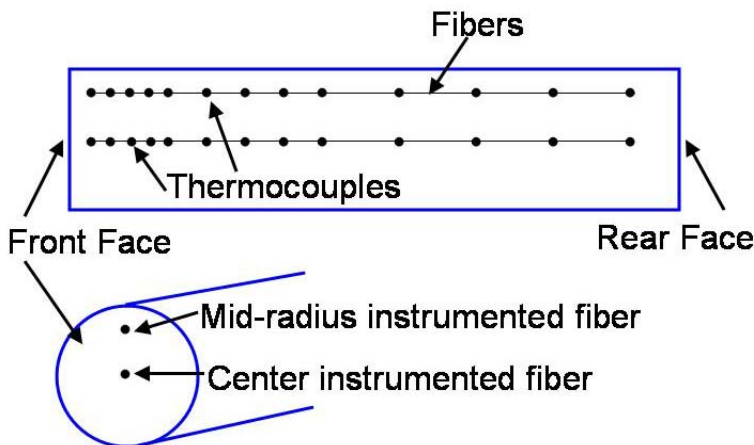


**Figure 3.14:** Thermocouple locations within the FOB. Note the increased spatial resolution near the front face.

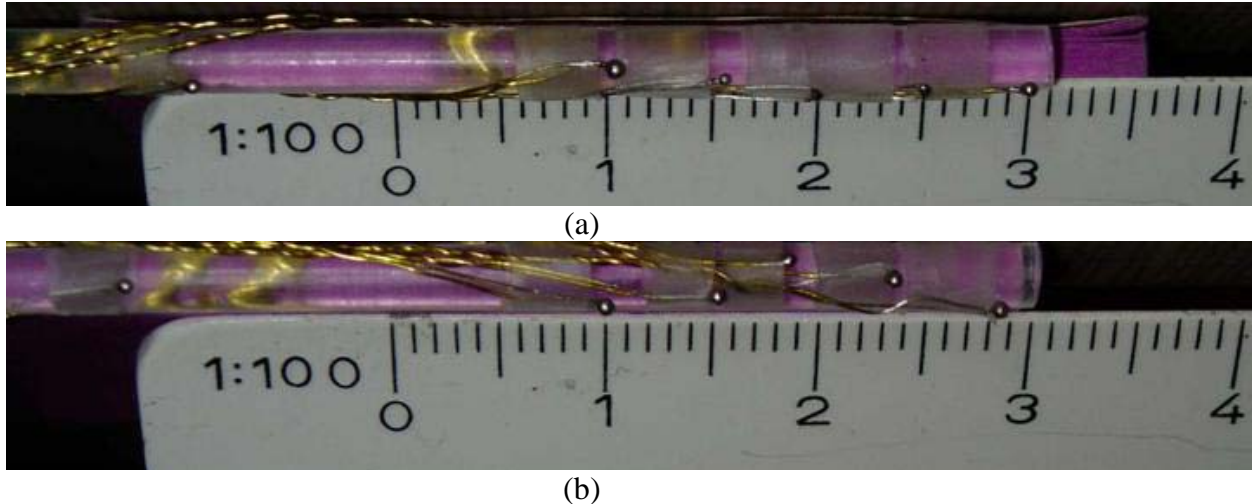


**Figure 3.15:** Thermocouples attached to fiber optic cables, (a) for a fiber at a mid-radial location and (b) for a fiber at the radial center of the FOB. Scale is in centimeters. Only 6 of 13 thermocouples are shown.

With the thermocouples installed, a very thin piece of reflective mylar was wrapped around the outer surface of the FOB in order to mimic the reflective properties of an aluminum collet. Finally, the outer surface of the FOB was wrapped with 2.3 cm of foam insulation in order to reduce the temperature gradients in the radial direction.

The light source and related optics for experimental setup #2 were nearly the same as experimental setup #1; the only difference was the output of the light source. It was determined that the source was mis-aligned and therefore not delivering its design power. The source was adjusted per manufacturer instructions and its output was increased to approximately  $3000 \text{ W/m}^2$  at the face of the FOB. The details of this adjustment process can be found in Chapter 2.

The increased illumination from the Oriel light source was then applied to the front face of the FOB. The measured temperatures for the two fibers at steady state are shown in Fig. 3.16. The increased resolution succeeded in capturing the thermal details near the front face of the FOB.

Note also that the temperature distribution is very nearly one-dimensional, which was the objective of adding the insulation. The higher temperatures recorded by the mid-radius fiber are most likely due to local variations in the porous structure of the FOB (see Fig. 3.17). Because the local porosity is greater at the mid-radius location as compared to the center, the local heat generation at this location will also be greater causing locally higher temperatures. This effect is not significant relative to the overall temperature rise.

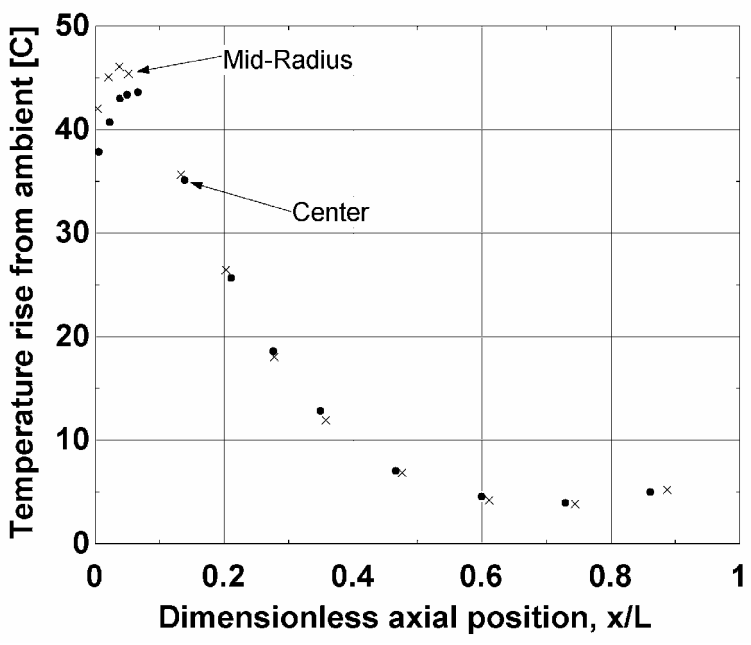


**Figure 3.16:** Temperature rise from ambient as a function of dimensionless axial position for different radial locations within the experimental FOB.

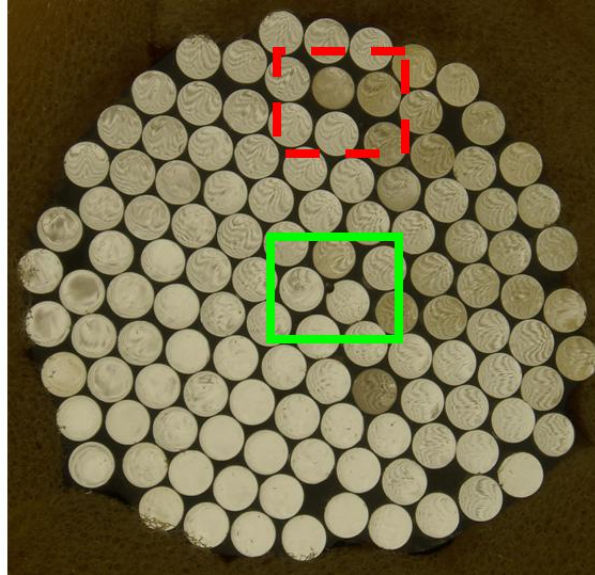


**Figure 3.17:** Front face of the experimental FOB. The solid square highlights the location of thermocouples at the center of the FOB. The dashed square highlights the location of thermocouples at the mid-radius of the FOB. Note that the porosity at the mid-radial location is greater than the porosity at the center.

The results of this experiment provide a basis for comparison with the predictions from the 1-D model described in Chapter 2. The result of this comparison is an estimate of the characteristic length associated with the pores and therefore a useful model of the thermal loading within the FOB.

### 3.4 Model and Experiment Comparison

Figure 3.18 shows the measured temperatures as a function of dimensionless axial position together with the 1-D model predictions. The dashed curves show 1-D model predictions adjusted up or down based on the uncertainty in the incident heat flux which was discussed in Chapter 2 (see Fig. 2.12). The 1-D model is fit to the experimental data in the following way. All parameters that describe the FOB are held constant except the characteristic length associated with absorption of the radiation in the pores,  $L_{ch,\alpha}$ , which is changed so that the axial location of

the peak temperature predicted by the 1-D model matches the experimentally observed location for the center fiber. Based on this technique, the characteristic length associated with the pores is 0.026 m.

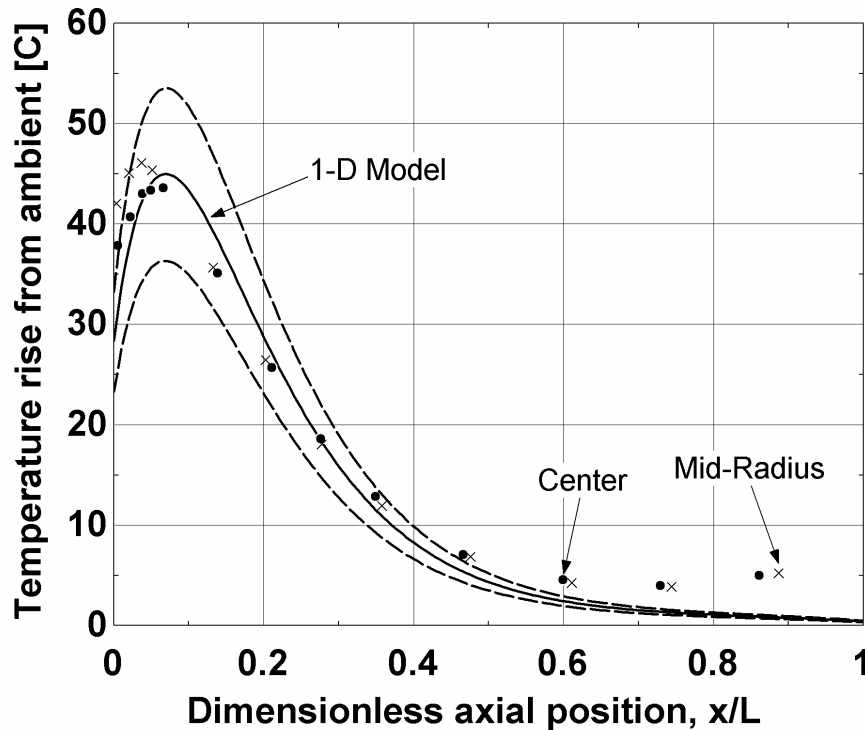


**Figure 3.18:** 1-D model fit to experimental data in order to determine the characteristic length associated with light absorption in the pores of the FOB. The points correspond to experimental data for both radial locations. The solid curve is the 1-D model prediction and the dashed curves are 1-D model predictions adjusted upwards or downwards based on the uncertainty in the measured incident heat flux.

As shown in Fig. 3.18, the model prediction does not agree at every measured location. Specifically, the model consistently under-predicts temperatures at the rear edge of the FOB (i.e., at  $x/L > 0.5$ ) but consistently over-predicts temperatures at the front edge of the FOB. This was particularly surprising near the rear of the FOB as the thermal situation in this region is relatively simple: radiation absorbed in the fibers causes a low level of volumetric energy generation that is rejected to ambient through the insulation via radiation and convection. It was expected that the

model would predict the temperature in this region very well and it was found that unreasonably low values of the heat transfer coefficient (or high values of the volumetric generation due to absorption in the fibers) were required to match the model with the measurements.

This bias error was eventually attributed to the thermocouple wire that runs along the axis of the FOB. Because the axial thermal resistance of the FOB is considerably lower than the thermal resistance associated with the thermocouple wire, the presence of the wire (even the very fine, 34 AWG wire used) introduces a relatively low resistance path and so a significant amount of heat is transferred in the wire. Because the wire is a path for heat transfer from the hot front face to the cooler rear face, there is a significant heat transfer into or out of the thermocouple junctions. Heat is transferred into the thermocouples at the front face and so they record a temperature that is somewhat lower than their surroundings. This heat is transferred out of the thermocouples at the rear face and so they record a temperature that is somewhat higher than their surroundings. A simple thermal-resistance model of this behavior reveals that the temperature error associated with thermocouple wire is on the order of a few degrees Celsius, which agrees with the apparent bias shown in Fig. 3.18.

### **3.5 Conclusions**

The primary purpose of the FOB experiments was to facilitate the development of a predictive thermal model of the FOB. Experimental results were compared with 1-D model predictions in order to infer a characteristic length associated with light absorption in the FOB pores which is the key input required to generate a model of the thermal loading. Experiments done at ORNL were the predecessor to more refined experiments that were carried out at the University of

Wisconsin-Madison and ultimately led to a highly spatially resolved measurement of the temperature distribution within the FOB. The characteristic length associated with absorption of light in the pores inferred from this process becomes the basis for a thermal loading model that is used to energize a 2-D model which is described in Chapter 4; this predictive, 2-D model is a powerful tool that allows the evaluation and design of alternative thermal management strategies for the FOB.

## Chapter 4

### Two-Dimensional Model

#### 4.1 Introduction

This chapter discusses the two-dimensional (2-D) finite element (FE) model that represents the predictive simulation tool that results from this research. The 2-D FE model is a natural extension of the 1-D analytical model that has been previously described and uses thermal loading parameters that are based on the results of Chapter 3. The purpose of the 2-D FE model is to evaluate and design thermal management strategies for a fiber optic bundle (FOB); this process will be described in Chapter 5.

This chapter describes the additions and modifications to the 1-D model that are required. The 2-D model predictions for the experimental FOB, discussed in previous chapters, are presented and compared with experimental results. The 2-D model is then extrapolated to consider on-sun conditions. The relevant differences between on-sun and experimental conditions are discussed. Finally, the 2-D model predictions for an on-sun FOB are presented and placed into context relative to qualitative observations for an on-sun FOB installed at ORNL. The 2-D FE model is implemented using the commercial software ANSYS 8.0 (ANSYS, 2005).

## 4.2 Additions and Modifications to the 1-D Analytical Model

### 4.2.1 Porosity as a function of radial position for the experimental FOB

In order to develop a 2-D model, the radial dependence of various parameters must be considered; the 1-D model considered only axial variations in these quantities. The porosity of the FOB is a function of radius due to the loosening of the bundle that occurs at the outer edge. The porosity affects the heat generation within the FOB as well as both the axial and radial effective conductivity of the FOB composite, as described in a later section of this chapter.

The calculation of porosity as a function of radial position proceeds as follows. Figure 4.1(a) shows a digital image of the face of the experimental FOB. Figure 4.1(b) is the same digital image of the FOB face after it has been processed in order to delineate the area of the face occupied by pores (the region shown in black) from the area of the face occupied by polymethylmethacrylate (PMMA) fiber (the region shown in white). From the processed image, Fig. 4.1(b), it is possible to calculate porosity by defining an annulus of the FOB face, Fig. 4.2, of width  $\Delta r$  at some dimensionless radial location ( $\bar{r}$ , defined as the radial location normalized against the radius of the FOB face) and counting the number of black and white pixels within that annulus. The porosity within this annulus is the ratio of the number of black pixels (i.e., pores) to the total number of pixels within that segment.

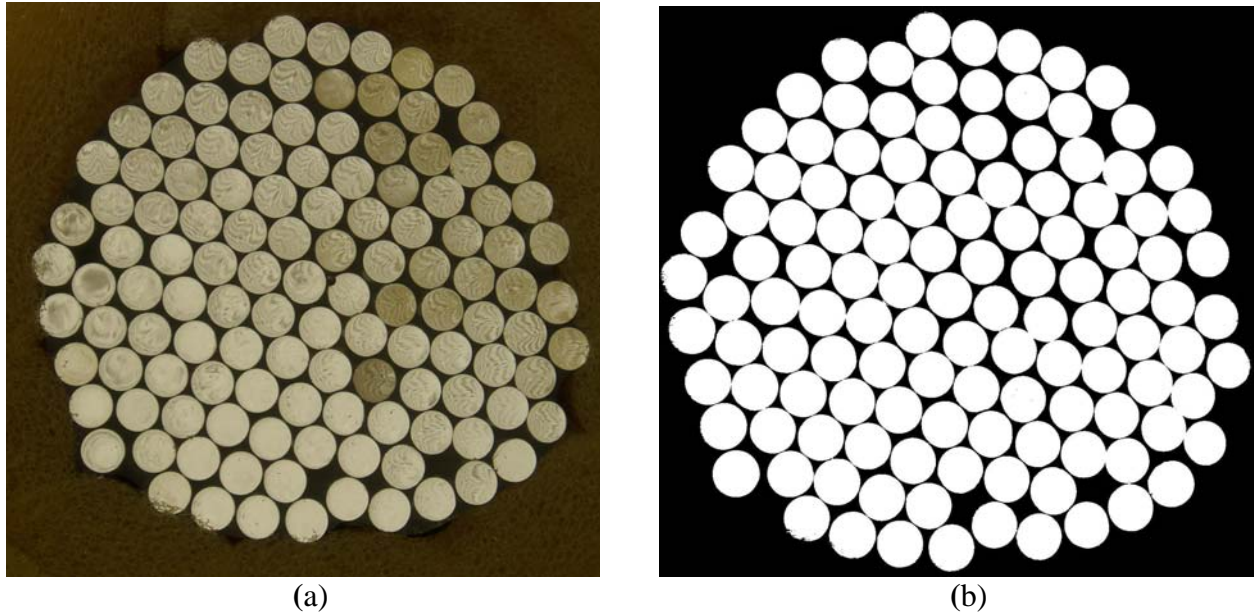


**Figure 4.1:** (a) Picture of the experimental FOB front face. (b) Picture delineating the gaps of the FOB face from the fibers.

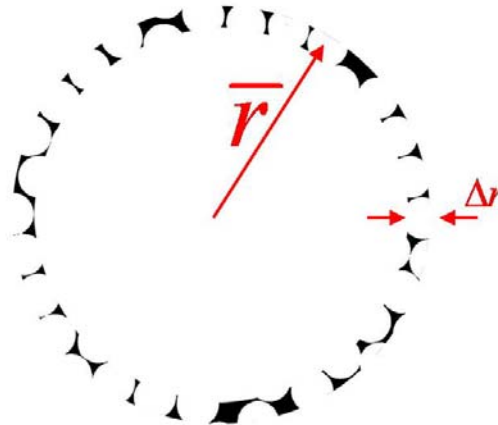


**Figure 4.2:** Arbitrary annulus of the face of the experimental FOB at position  $\bar{r}$  of width  $\Delta r$ .

The process for calculating the porosity of an annulus can be expedited using the MATLAB software to carry out the image processing. A MATLAB program (see Appendix B) was written in order to map the black and white image shown in Fig. 4.1(b) onto a 2-D array. The array is broken down into annular segments and the porosity within each segment is calculated. This process provides the porosity,  $\phi_{pore}$ , as a function of dimensionless radius, as shown in Fig. 4.3.

Note that at the center of the FOB, where a single fiber is located, the porosity is zero. One would expect that the porosity of the FOB would approach unity at the outer edge of the FOB where the fibers would just touch a round collet; Fig. 4.3 shows that the porosity does increase dramatically at the outer edge. However, the porosity does not reach unity because the experimental FOB is not perfectly circular. The outer edge is defined by an effective radius (see Eq. (2.39)) and therefore some few fibers will intersect that outer edge.

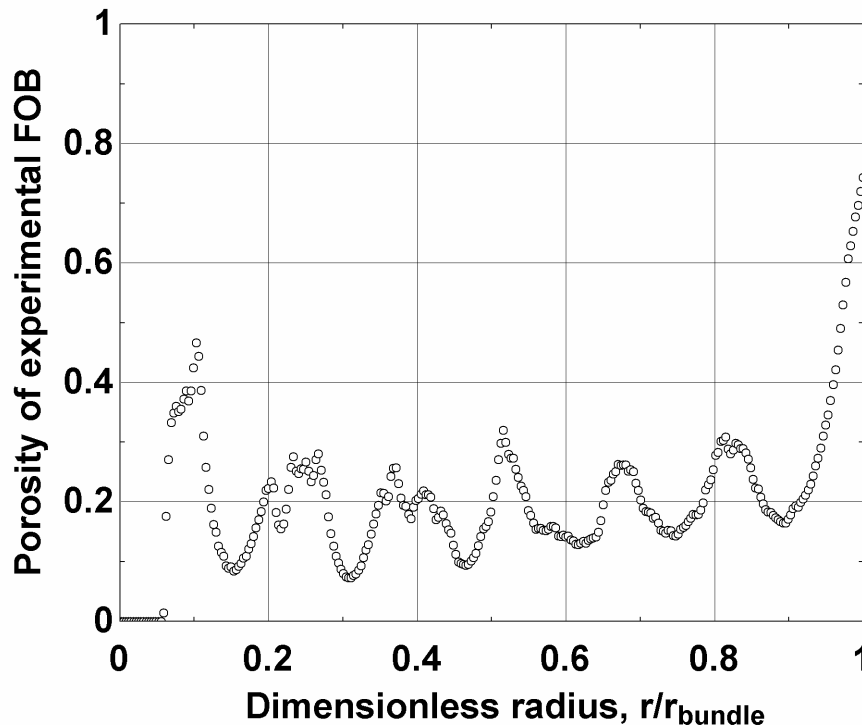


**Figure 4.3:** Porosity as a function of dimensionless radius for the experimental FOB shown in Fig. 4.1. Data are taken using MATLAB.

#### 4.2.2 Radially dependent heat generation for the experimental FOB

As with the 1-D model, the heat generation used to thermally load the 2-D model is assumed to be exponentially distributed with respect to axial position and characterized by some characteristic length that does not depend on radius; clearly, to the extent that the porosity affects the optical characteristics of the FOB, there may be some radial dependence to the characteristic

length but this is neglected. The volumetric heat generation, however, also depends on porosity and therefore on radial position as shown by Eq. (4.1), which is derived from Eqs. (2.14) and (2.15).

$$\dot{g}_{\alpha}''' = \frac{\phi_{pore}(\bar{r}) \dot{q}_{inc}''}{L_{ch,\alpha}} \exp\left(-\frac{x}{L_{ch,\alpha}}\right) \quad (4.1)$$

Eq. (4.1) predicts the rate of heat generated per unit volume within the FOB due to light absorption in the pores. A similar equation can be derived for the heat generation rate due to light absorption in the fibers, Eq. (4.2).

$$\dot{g}_{\tau}''' = \frac{\phi_{pore}(\bar{r}) \dot{q}_{inc}''}{L_{ch,\tau}} \exp\left(-\frac{x}{L_{ch,\tau}}\right) \quad (4.2)$$

The total volumetric generation rate imposed on the 2-D model is then given by Eq. (4.3), where the total heat generation rate is dependent on both the radial and axial position within the FOB.

$$\dot{g}_{tot}'''(\bar{r}, \bar{x}) = \dot{g}_{\alpha}'''(\bar{r}, \bar{x}) + \dot{g}_{\tau}'''(\bar{r}, \bar{x}) \quad (4.3)$$

The total volumetric heat generation was tabulated using the MATLAB porosity data of Fig. 4.3, Eqs. (4.1) through (4.3), and specified values of  $\dot{q}_{inc}''$ ,  $L_{ch,\alpha}$ , and  $L_{ch,\tau}$  which are consistent with the results described in Chapters 2 and 3. The tabular values were integrated with ANSYS and used to represent the volumetric generation rate through interpolation.

### 4.2.3 Radially dependent equivalent conductivities for the experimental FOB

The porosity affects the effective axial and radial conductivities of the FOB. The calculation of effective axial conductivity is described in Chapter 2 and is based on a parallel resistance network involving the core, cladding and air. The radial conductivity is calculated using the method described by Kanzaki, et al. (1990) which was developed to estimate the effective thermal conductivity of an electric coil but is generally applicable to any composite medium that has the closed-packed geometry shown in Fig. 4.4.

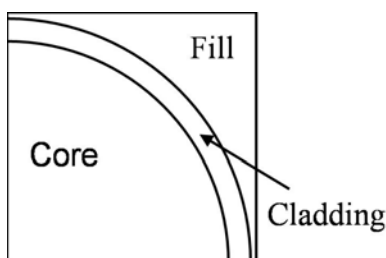


**Figure 4.4:** Unit cell geometry for the calculation of effective thermal conductivity.

For the case of the experimental FOB, the core is PMMA, the cladding is a fluorinated polymer and the fill material is air. The calculation of effective axial conductivity requires knowledge of the fraction of the total unit cell that is occupied by each of these three components as well as the conductivity of each component. Conductivity values for PMMA, air and cladding are summarized in Table 2.3. The fractions of the unit cell occupied by each component are determined from average porosity values calculated using Fig. 4.3. Because Fig. 4.1 (b) does not allow differentiation between the fiber cladding and the pore, the fraction of the unit cell occupied by cladding is assumed to be a constant value of 0.034 (see Chapter 2 section 2.5.2). The fractions of the unit cell occupied by the filling and core can then be calculated from Eq. (2.7).

Figure 4.5 shows the effective axial conductivity and effective radial conductivity as a function of dimensionless radius. ANSYS does not allow conductivity that depends upon position to be input as a function or table. Instead, individual areas must be defined, each of which can have a different value for conductivity. Due to this limitation conductivities were input into ANSYS by defining 11 equal width segments, each with its own radial and axial conductivity calculated from an average porosity using the MATLAB data shown in Fig. 4.3.

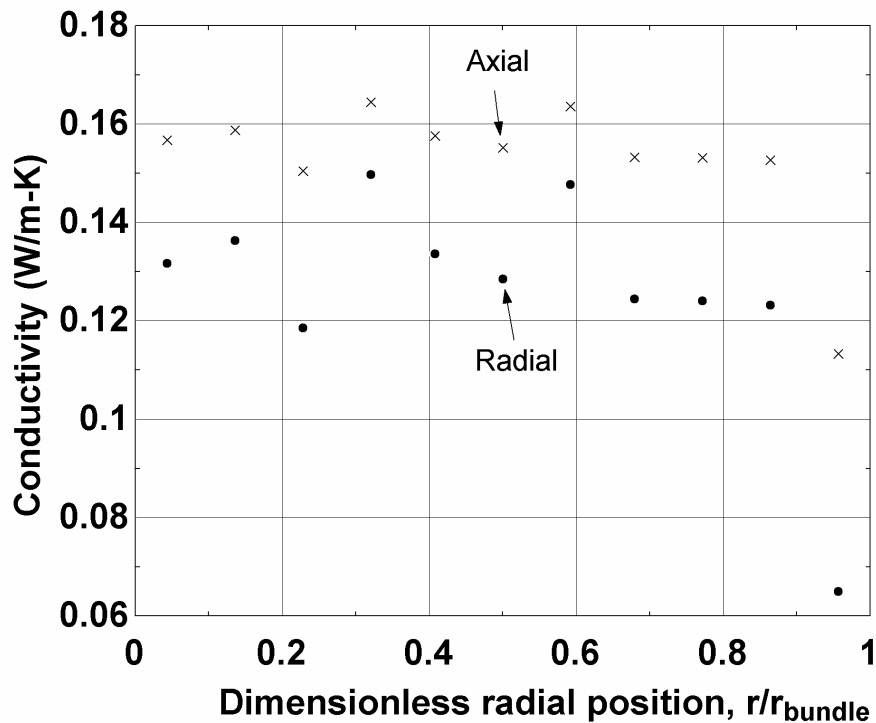


**Figure 4.5:** Axial and radial conductivity as a function of dimensionless radius for the 2-D model.

### 4.3 ANSYS Results for Experimental FOB

The variations in conductivity that are shown in Fig. 4.4 were integrated with the 2-D model together with the radial variations in the rate of heat generation represented by Eq. (4.3). Figure 4.6 illustrates a schematic of the FOB as it is modeled in ANSYS. It shows a 2-D, axisymmetric section of the FOB that is oriented so that the incident heat flux enters the front face at the

bottom. The 11 segments that are shown in Fig. 4.6 correspond to the 11 segments that were assigned unique values of radial and axial conductivity as shown in Fig. 4.4.

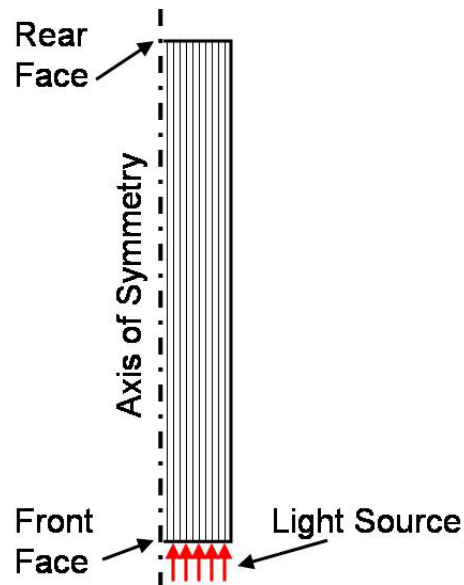


**Figure 4.6:** Schematic of the 2-D, axisymmetric model of the experimental FOB.

All parameters other than porosity, radial and axial conductivities, and heat generation were defined and estimated as described in the context of the 1-D model in Chapter 2. These parameters include the incident heat flux, all heat transfer coefficients, the characteristic length associated with the fibers, and the characteristic length associated with the pores which was inferred from experimental data and the 1-D model. The model is meshed and used to obtain predictions of temperature within the FOB; Figure 4.7(a) shows the predicted temperature distribution within the FOB as a function of dimensionless axial position for three radial positions. The dimensionless axial position is defined as the axial location normalized against the length of the FOB. The label ‘center’ describes the temperature distribution at the exact center of the FOB, along the axis of symmetry. The label ‘mid-radius’ describes the temperature distribution at a position halfway toward the outer edge of the FOB. The label ‘edge’ describes

the temperature distribution at the outer edge of the FOB. Figure 4.7(b) shows the temperature contour plot predicted by the 2-D model; note that only approximately the first third of the FOB is shown in Fig. 4.7(b).

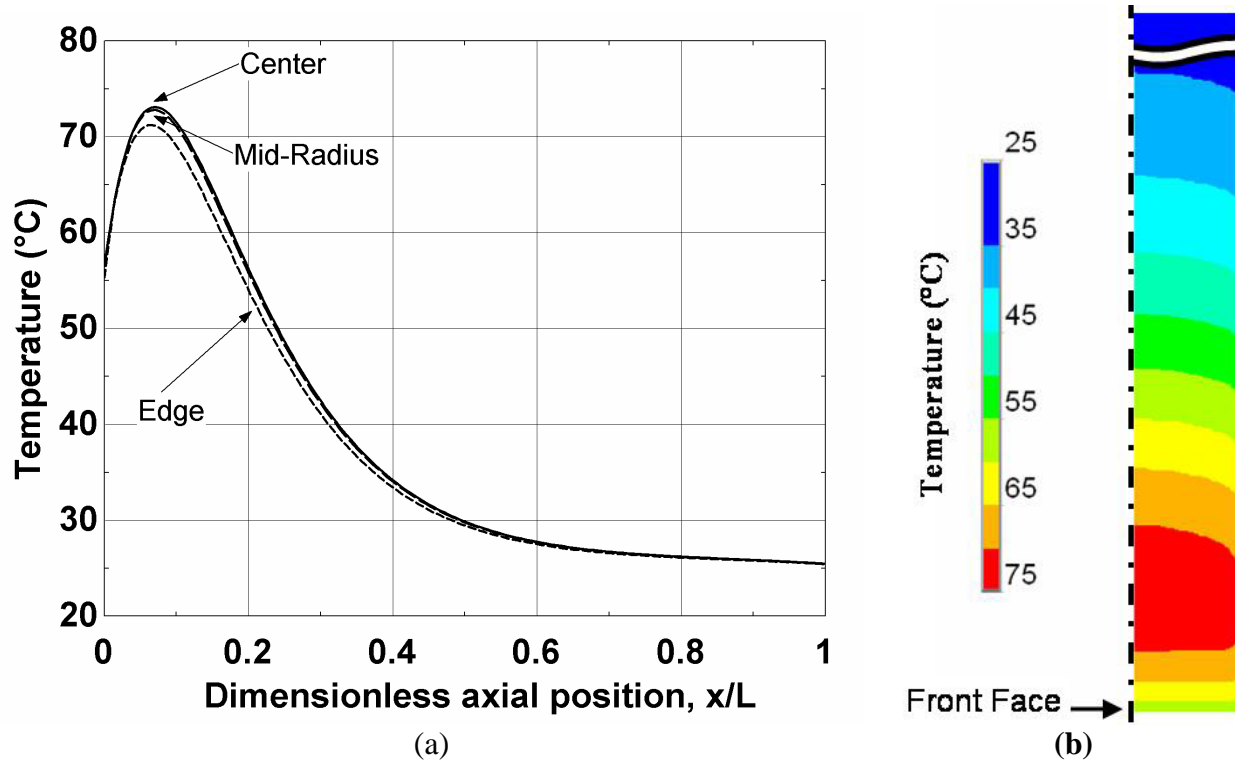


**Figure 4.7:** (a) Temperature as a function of dimensionless axial location for several radial locations, and (b) the temperature contour plot predicted by the 2-D model. Note that only approximately the first third of the experimental FOB in the axial direction is shown.

To be assured that the mesh used in the 2-D model was fine enough, the change in the maximum temperature within the FOB was recorded as the number of nodes was doubled. The mesh for the 2-D model was chosen such that the change in maximum temperature was reasonably low, at least less than 1.0 °C. For the mesh utilized in Fig. 4.7 the change in the maximum temperature when the number of nodes was doubled was .01 °C. The 2-D model was also verified by making sure that 2-D model results agreed with 1-D model results in the case of infinite thermal conductivity in the radial direction.

Figure 4.8 compares the 2-D model results with experimental data. Figures 4.8(a) and (b) show the measured and predicted temperature as a function of axial location at the center and mid-radius of the FOB, respectively. Figure 4.8 (a) and (b) both indicate that the 2-D model over-predicts temperatures at the front face of the FOB and under-predicts temperatures at the rear face. This same type of bias was encountered when comparing 1-D model predictions to the experimental results and is likely related to the transport of energy along the thermocouple wire down the length of the FOB. For a more detailed explanation, see the end of Chapter 3, Fig. 3.16.

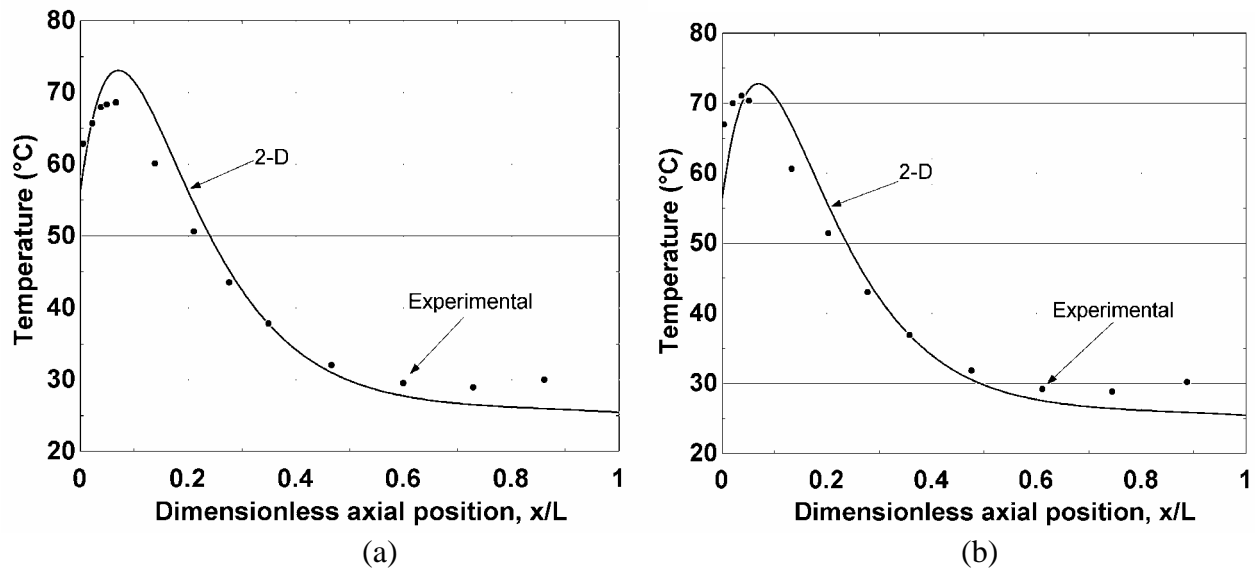


**Figure 4.8:** Measured and predicted temperature in FOB as a function of axial position (a) at the center and (b) at the mid-radius of the FOB.

#### 4.4 ANSYS Results for On-Sun FOB

Previous discussion of the FOB concerned the experimental FOB built at the UW-Madison, the front face of which is shown in Fig. 4.1. The experimental FOB differs from the FOB that is used in the Hybrid Solar Lighting (HSL) assembly. The front face of this FOB is shown in Fig. 4.9 and will subsequently be referred to as the on-sun FOB. The composite structure of the on-

sun FOB is similar to the experimental FOB and therefore the characteristic length associated with pores is assumed to be the same. However, the on-sun FOB differs from the experimental FOB in three important aspects: its porosity, the surrounding structure, and the incident heat flux.

The experimental FOB was composed of 120 fiber optic cables that were bundled together with several tie wraps. The on-sun FOB is made of 126 fiber optic cables that are thermally fused together; the effect of this process is to substantially reduce the porosity as can be seen in Fig. 4.9. The shapes of the individual fiber optic cables within the face of the on-sun FOB (Figure 4.9(a)) have been deformed by the thermal fusing process and this results in a substantially reduced porosity of the on-sun FOB face relative to the experimental FOB.

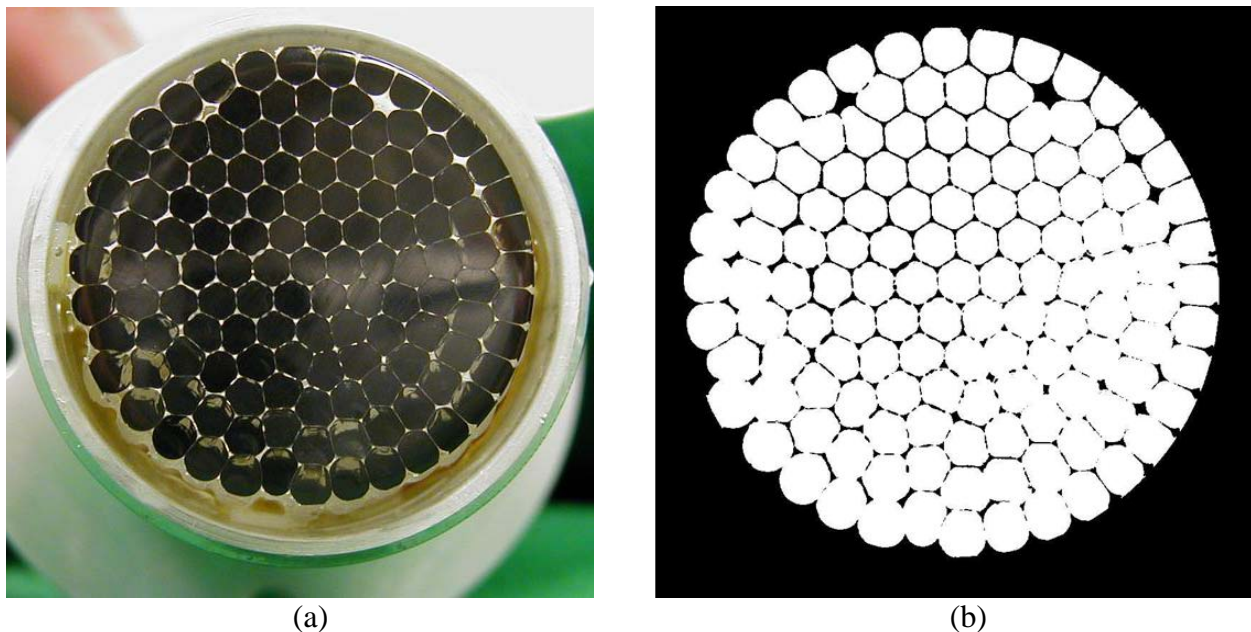


**Figure 4.9:** (a) Picture of a thermally fused FOB with 126 fibers. (b) Picture delineating the gaps of the FOB face from the fibers.

Figures 4.10(a) and (b) illustrate the porosity of the experimental FOB and on-sun FOB, respectively, as a function of radial position; the porosity was calculated using the image

processing technique described in section 4.2.1. The considerable reduction in porosity for the on-sun FOB is evident in Fig. 4.10.

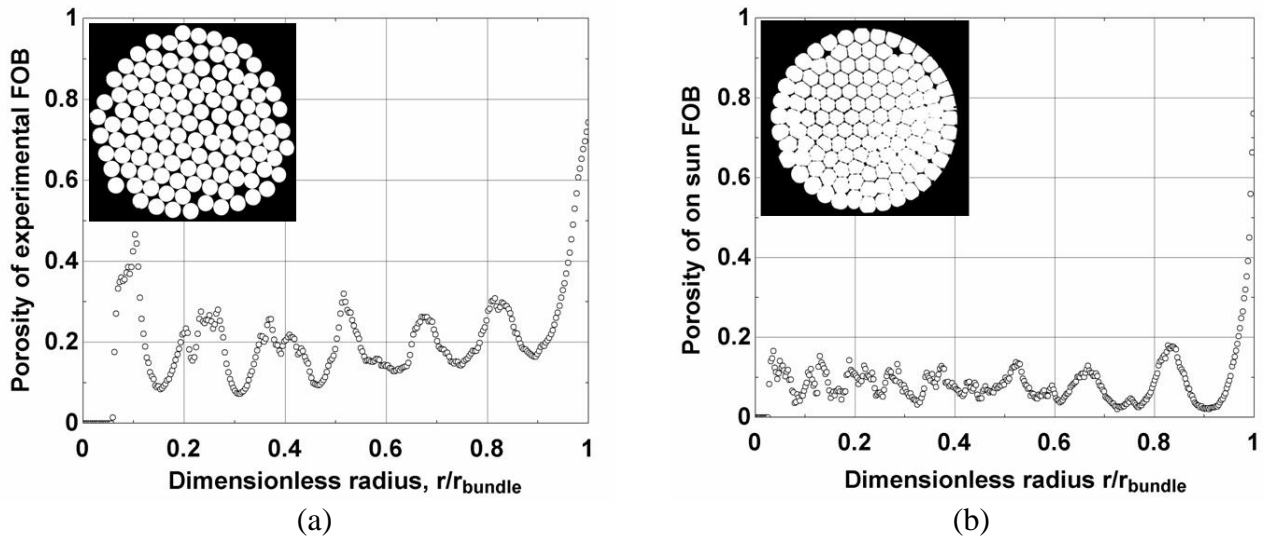


**Figure 4.10:** Porosity as function of dimensionless radius for the (a) the experimental FOB and (b) the on-sun FOB. The inset digital processed images are of the corresponding FOBs and delineate the pores of the FOB face from the fibers.

The structure of the assembly used to mount the on-sun FOB is shown in Fig. 4.11. Figure 4.11(a) shows the assembly in its entirety and (b) presents a close up of the region surrounding the on-sun FOB. The FOB is mounted in an aluminum collet that is installed in the assembly with an aluminum sleeve. The sleeve is held in an aluminum mount, which holds the primary mirror, as shown in Fig. 4.11. The aluminum mount also serves to support the secondary mirror; however, due to the small area associated with the connection between the secondary mirror and the mount, this component is neglected for 2-D model simulations. The incident radiation (not shown) strikes the front face of the on-sun FOB from the bottom. Before passing through the FOB, however, the incident radiation passes through a PMMA rod that sits flush against the front face of the FOB and filters any remaining infrared radiation out of the incident spectrum.

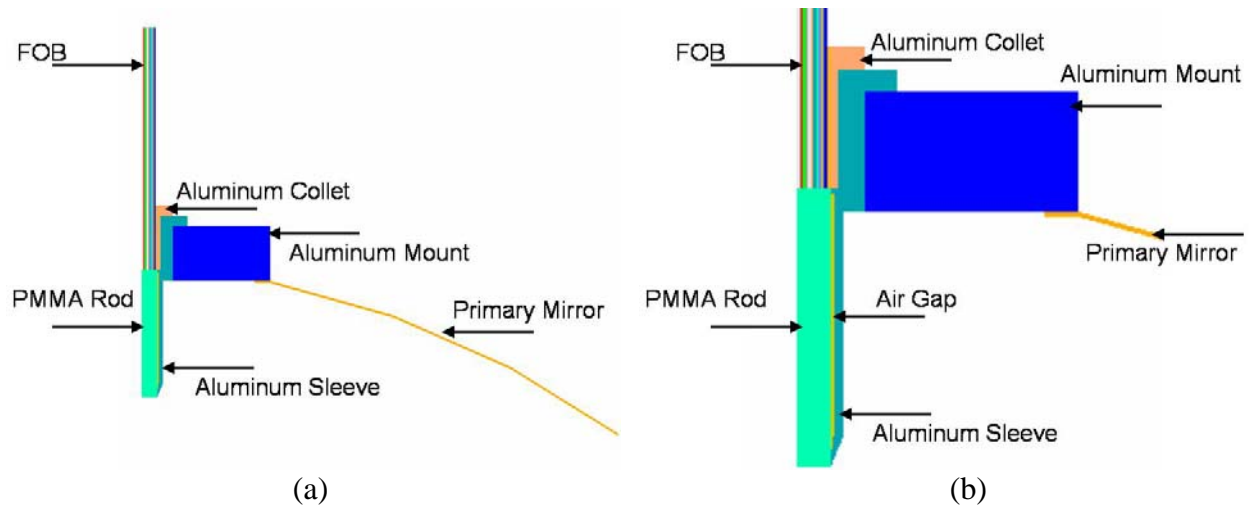


**Figure 4.11:** Schematic of the on-sun FOB and assembly showing (a) the FOB and assembly components in their entirety and (b) a close up of the region surrounding the FOB.

The incident heat flux onto the on-sun FOB face is substantially larger than could be obtained using the light source during testing of the experimental FOB. A schematic that illustrates the on-sun conditions is shown in Fig. 4.12. The on-sun FOB is installed in the HSL assembly and then the assembly tracks the motion of the sun in order to collect direct normal solar radiation. The collection process both concentrates and filters solar radiation. The direct normal solar radiation that is incident on the primary mirror is reflected to the ‘cold’ mirror with an average specular reflectance of 94%. The ‘cold’ mirror transmits unwanted infrared radiation and reflects visible radiation to the ‘hot’ mirror with an average specular reflectance of 97%. The ‘hot’ mirror reflects unwanted radiation and transmits visible radiation to the face of the on-sun FOB with an average transmittance of 89%. The concentrated and filtered radiation incident on the face of the FOB is then transmitted through the FOB to the interior of the building in order to provide lighting. The concentration process is quantified in Eq. (4.4) by the concentration ratio,  $C$ , which is defined as the area of the primary collecting surface,  $A_{primary}$ , divided by the area of the FOB face,  $A_{bundle}$ .

$$C = \frac{A_{primary}}{A_{bundle}} \quad (4.4)$$

For the nominal HSL design, the concentration ratio is 940. The product of the efficiencies of each individual stage results in an overall efficiency of 81%. Therefore, the intensity of the radiation that is incident on the face of the on-sun FOB will be approximately 761x the intensity of the direct normal solar radiation collected by the primary mirror.

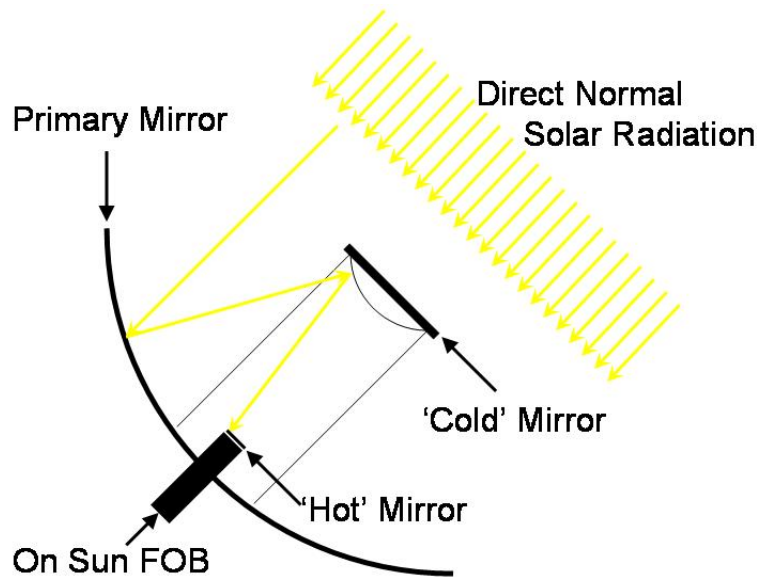


**Figure 4.12:** HSL assembly and its associated components.

The calculation of the radiation flux that is incident on the face of the on-sun FOB considers the intensity of the direct normal solar radiation that is incident on the primary mirror, the concentration ratio, and the overall efficiency of the filtration process. These calculations are carried out for a scenario that will result in the maximum temperature within the FOB and therefore represents the most demanding operating condition from a thermal management standpoint. The maximum direct normal radiation intensity is experienced on a clear summer day when the sun is at solar noon and the solar radiation passes through an air mass of 1.0. However, the sun is only at solar noon for a short period of time and there is a substantial

thermal time constant associated with the FOB; therefore, an effective air mass of 1.5 was used to represent a more realistic thermal loading.

The spectral power distribution associated with direct normal solar radiation traveling through an air mass of 1.5 is shown in Fig. 4.13 (Gueymard, 1995 and 2001). Also shown in Fig. 4.13 is the spectral power distribution of concentrated solar radiation after it has been filtered by all three mirrors. The integrated direct normal solar radiation falling on the primary mirror is approximately  $290 \text{ W/m}^2$ . After concentration and filtration, the integrated solar radiation falling on the face of the FOB is approximately  $221,000 \text{ W/m}^2$ .

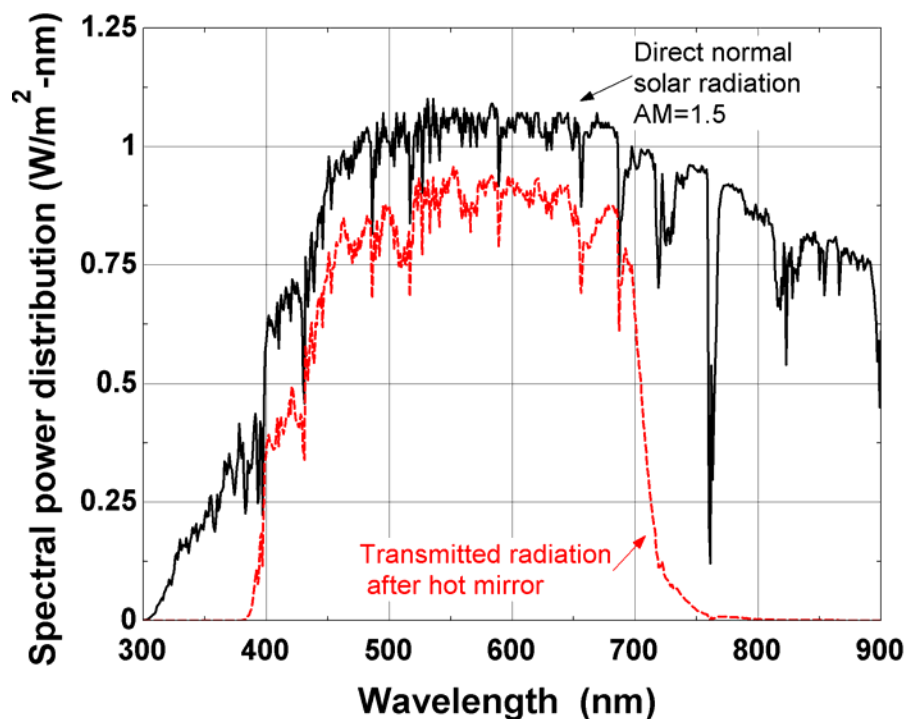


**Figure 4.13:** Spectral power distribution as a function of wavelength for direct normal solar radiation incident on the primary mirror and concentrated solar radiation after transmission through the hot mirror (Gueymard, 1995 and 2001).

The temperature distribution predicted by the 2-D model for the on-sun FOB is illustrated in Fig. 4.14. Figure 4.14(a) shows the predicted temperature as a function of dimensionless axial

position for two radial positions. The temperature distribution is also displayed in the form of the temperature contour plot, shown in Fig. 4.14(b).

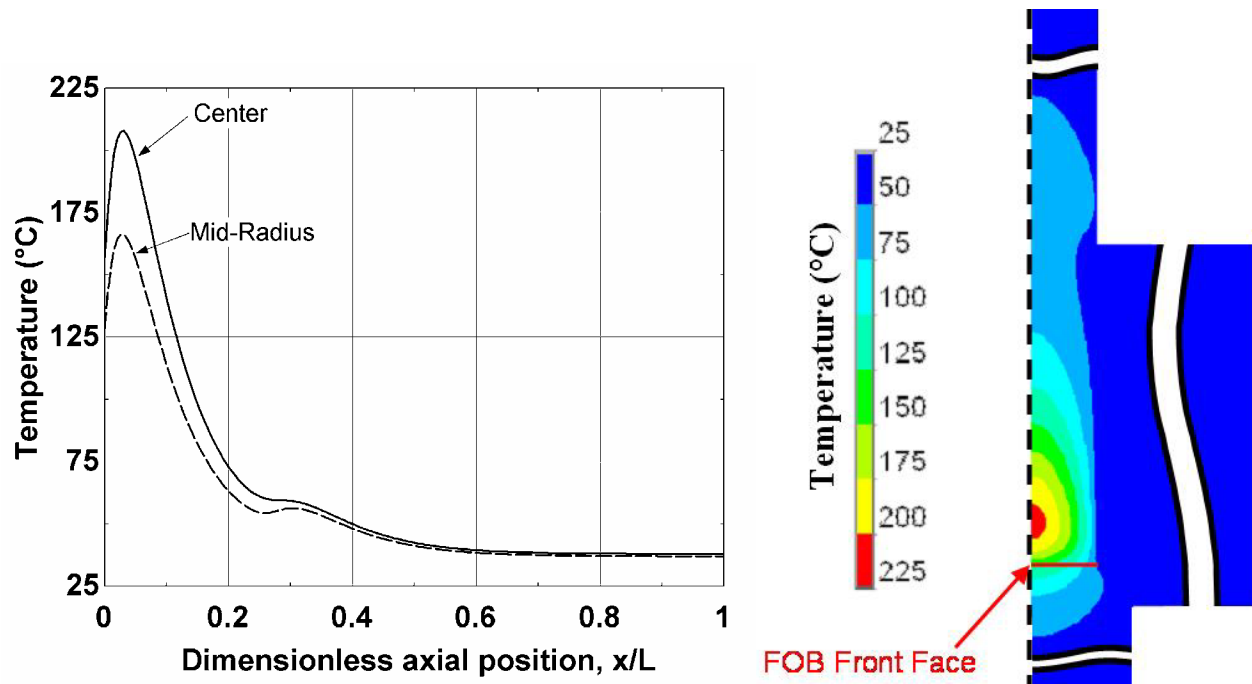


**Figure 4.14:** (a) Temperature as a function of dimensionless axial location for several radial locations, and (b) the temperature contour plot predicted by the 2-D model. Note that only approximately the first third of the on-sun FOB is shown.

The maximum temperatures within the FOB predicted by the 2-D model shown in Fig. 4.14 is nearly 225°C which is substantially above the melting point of the PMMA fibers (approximately 150°C), and are thus qualitatively in agreement with observed thermal failure of the on-sun FOB. The results of Fig. 4.14 provide a non-thermally managed baseline case that is used to evaluate alternative thermal management solutions in the next chapter.

## 4.5 Conclusions

The 1-D model and experimental results discussed in previous chapters provided the basis for the development of the 2-D FE model that was presented in this chapter. This 2-D model includes radially dependent effective conductivity (in both the axial and radial direction), porosity, and heat generation. The temperature distributions within the experimental FOB were predicted by the 2-D model and compared to the experimental results discussed in Chapter 3 in order to provide some verification. The 2-D model was then extended to include the more complicated geometry and reduced porosity of the on-sun FOB. The temperature distribution predicted for the on-sun FOB under a condition that corresponds to the maximum anticipated thermal load will be used as a baseline for the evaluation of various thermal management strategies in Chapter 5.

## Chapter 5

# Thermally Managed Fiber Optic Bundle Configurations

## 5.1 Introduction

The purpose of this chapter is to utilize the 2-D finite element (FE) model developed in Chapter 4 as a design tool in order to facilitate the development of thermally management strategies for an on-sun FOB. The chapter begins by considering the design constraints associated with a production on-sun FOB. Keeping these requirements in mind, several thermal management strategies are investigated using the 2-D FE model. The steady state temperature distribution predicted for each configuration is compared to the baseline, non-thermally managed on-sun FOB case that was described at the end of Chapter 4. The chapter concludes with some experimental results for a thermally managed experimental FOB.

## 5.2 Thermal Management Strategies

### 5.2.1 Design considerations

The thermal performance requirement of the on-sun FOB is simple; the maximum temperature rise within the FOB must be maintained at an acceptable level. According to manufacturer specifications, the maximum allowable operating temperature (i.e., the temperature at which no deterioration in optical properties will occur) is 70°C for polymethylmethacrylate (PMMA) fibers. In addition, there are several monetary and physical restrictions associated with a practical system. As discussed in Schlegel (2003), in order for a Hybrid Solar Lighting (HSL)

system to be economically viable in many regions of the country, the capital cost must be less than a few hundred dollars per HSL module. The HSL system must be particularly inexpensive in regions where the solar resource is limited and the utility rates are comparatively low; in Madison, Wisconsin for example, the 10 year break even capital cost per HSL module is estimated to be less than \$500 (Schlegel, 2004). Due to these economic restrictions, all components in the HSL, including the FOB, must be inexpensive. Further, the HSL, and therefore the thermal management system for the FOB, must be maintenance free and consume little to no power.

There are a few physical limitations associated with the design of the FOB. As shown in Fig. 4.11, the FOB sits snugly in an aluminum collet with its front face flush against a PMMA rod. Therefore, forced convection across the front face of the FOB is not practical without a significant alteration of the geometry.

Several thermal management strategies have been developed that satisfy these constraints. These strategies are discussed in subsequent sections; they are all inexpensive, maintenance free, and consume no power.

### **5.2.2 Single copper rod**

The first strategy replaces the center PMMA fiber of the FOB with a single copper rod. The rod is the same diameter as the fiber that it replaces, approximately 1.5 mm, and is approximately 8 cm in length. The advantage of this strategy are that copper rods are fairly inexpensive, approximately \$10-\$20 each (McMaster-Carr, 2005). This price, however, might reduce

considerably when purchased in bulk and alternate vendors are considered. Also, the configuration of the FOB is essentially unchanged. The minor disadvantage of this strategy is a slight reduction in transmitted radiation; note that there are 126 PMMA fibers and so the loss of one of these represents less than 1% reduction in FOB efficiency. The steady state temperature distribution predicted by the 2-D FE model for an on-sun FOB with a single copper rod at its center is shown in Fig. 5.1.

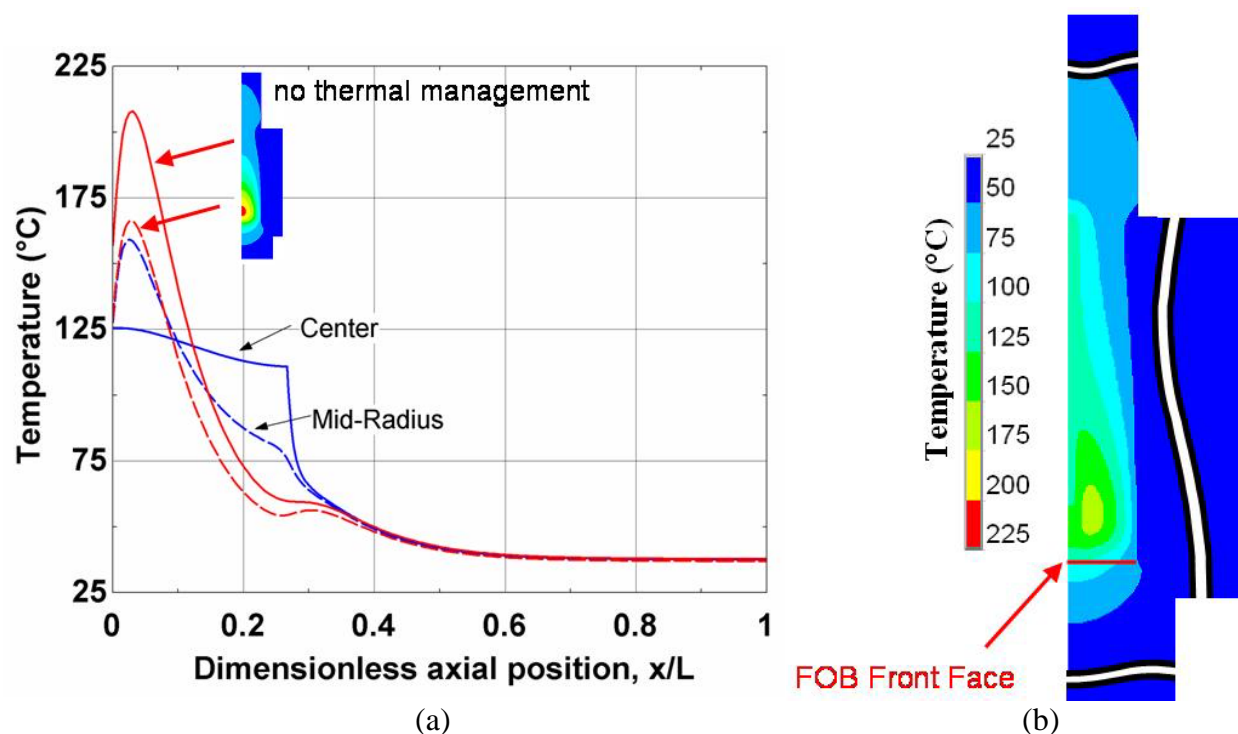


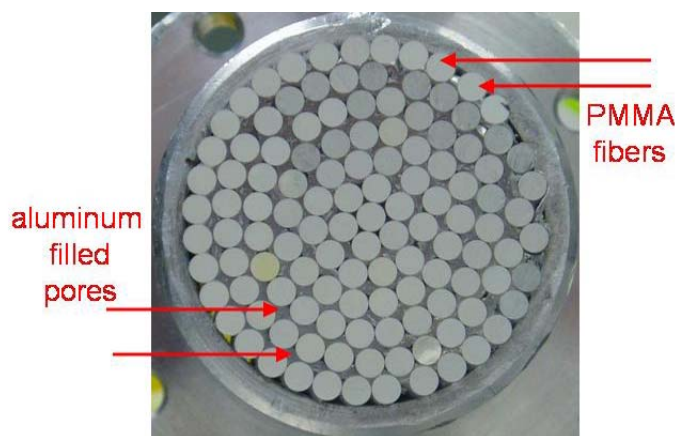
**Figure 5.1:** (a) Temperature as a function of dimensionless axial position within the on-sun FOB. Center (solid) and mid-radius (dashed) temperature distributions are plotted for both the non-thermally managed FOB and the FOB with a single copper rod at its center. Note that the inset image is a temperature contour plot of the non-thermally managed bundle for reference. The temperature scale associated with the inset image is the same as that shown in (b). (b) Temperature contour plot for the FOB with a single copper rod at its center.

The copper rod acts to efficiently transmit the energy that is deposited at the front face of the FOB down the length of the copper rod which tends to reduce the magnitude of the peak that had

occurred close to the front face. Because there is a single copper rod at the center, the maximum temperature inside the FOB is shifted from the center to a mid-radius location. The use of the copper rod considerably reduces the maximum temperature rise within the FOB.

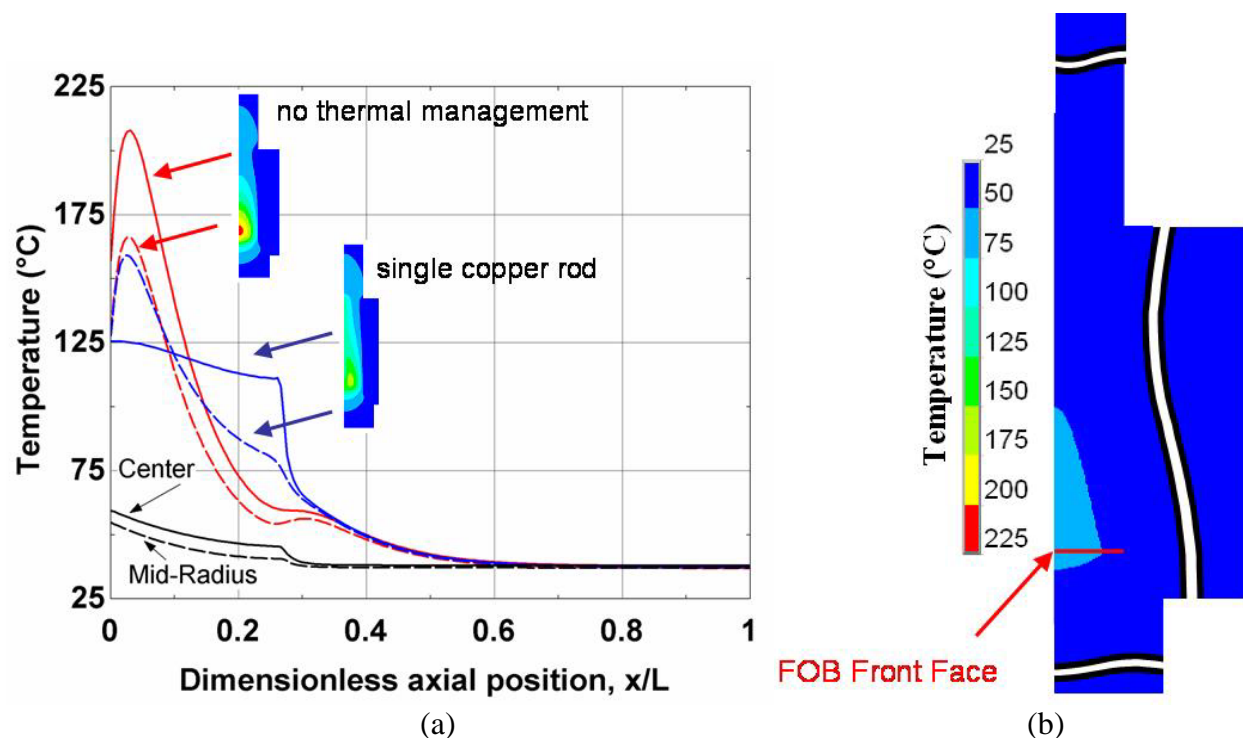
### 5.2.3 Aluminum filled pores

The second strategy replaces the air that currently occupies the pores of the on-sun FOB with aluminum. An obvious practical difficulty associated with this strategy is the development of a process that fills the pores with aluminum. Clearly, molten aluminum cannot be deposited into the pores without melting the fibers; however, there are a few other alternatives. One option is to use a commercially available aluminum epoxy or urethane to fill the pores after the FOB is built. Another, and perhaps simpler method, is to wrap an inexpensive aluminum foil around the fibers before the FOB is built. An experimental FOB built in this manner is shown in Fig. 5.2. The aluminum foil extends approximately 15 cm down the length of the FOB.



**Figure 5.2:** Experimental FOB with aluminum filled approximately 15 cm into the pores.

The FOB was not experimentally tested because it was not instrumented before it was built; however, the steady state temperature distribution predicted by the 2-D FE model for an on-sun FOB with pores filled approximately 8 cm deep with aluminum is shown in Fig. 5.3.



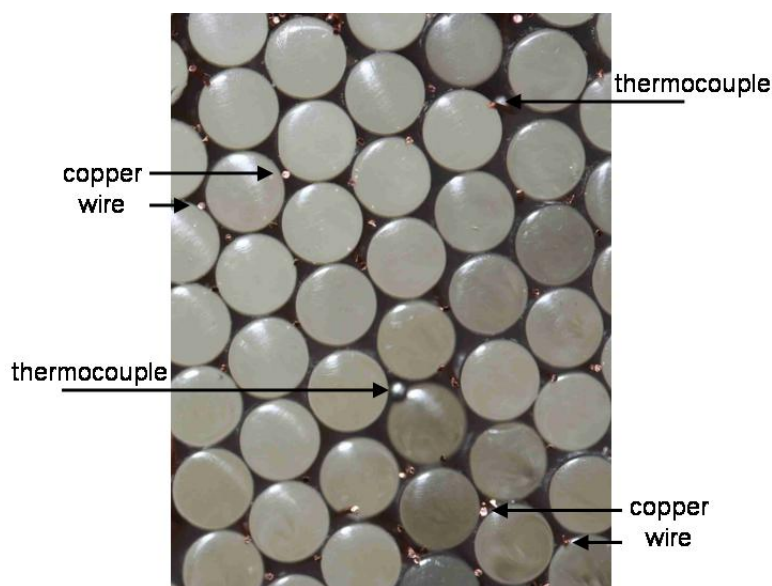
**Figure 5.3:** (a) Temperature as a function of dimensionless axial position within the on-sun FOB. Center (solid) and mid-radius (dashed) temperature distributions are plotted for the non-thermally managed FOB, the FOB with a single copper rod at its center, and the FOB with aluminum filled pores. Note that the inset images are temperature contour plots of the non-thermally managed and copper rod FOBs. The scale for both inset images is the same as that shown in (b). (b) Temperature contour plot for the FOB with aluminum filled pores.

Figure 5.3 shows that the aluminum filled pore strategy provides a dramatic reduction in the maximum temperature within the FOB. As with the single copper rod, the aluminum is conductive and therefore substantially improves the effective thermal conductivity of the composite in both the axial and radial directions. The result is that the peak at all radial locations is smoothed out. The additional advantage of the aluminum filled pore is that the aluminum will reflect a large percentage of incident radiation that would otherwise be absorbed in the pores and results in the primary source of thermal loading on the FOB. For the FOB shown in Fig. 5.3, the aluminum foil was assumed to reflect 86% of incident radiation (Duffie and Beckman, 1991).

By reflecting this portion of the radiation incident on the aluminum filled pores, the thermal load on the FOB is reduced; as a result, both the average and the peak temperature within the FOB decrease.

### 5.3 Experimental FOB with Copper Wire in Pores

An experiment was developed in order to compare the temperature rise within a non-thermally managed experimental FOB with a thermally managed experimental FOB. The non-thermally managed FOB is the same as that described in Chapter 3. An image of the thermally managed FOB face is shown in Fig. 5.4. Several of the interstitial spaces that make up the pores of the FOB were filled with hundreds of small gauge, approximately 30 AWG, copper wire. The depth of the copper wire is approximately 10 cm.



**Figure 5.4:** Digital image of the experimental FOB after several pieces of copper wire have been inserted into the interstitial gaps in the FOB face.

The analyses of the thermal management strategies in this chapter suggest that the wire will redistribute the energy absorbed in the FOB along the length of the copper wires. The steady

state temperature distribution predicted by the 2-D model for the thermally managed FOB of Fig. 5.4 is shown in Fig. 5.5. For these predictions, only the axially conductivity is changed to reflect the added copper within the FOB. All other parameters, including heat generation and radial conductivity remain the same. The non-thermally managed experimental FOB described in Chapter 4 is plotted for reference. Note that the model does predict a redistribution of the energy deposited within the FOB along the length of the copper wires.

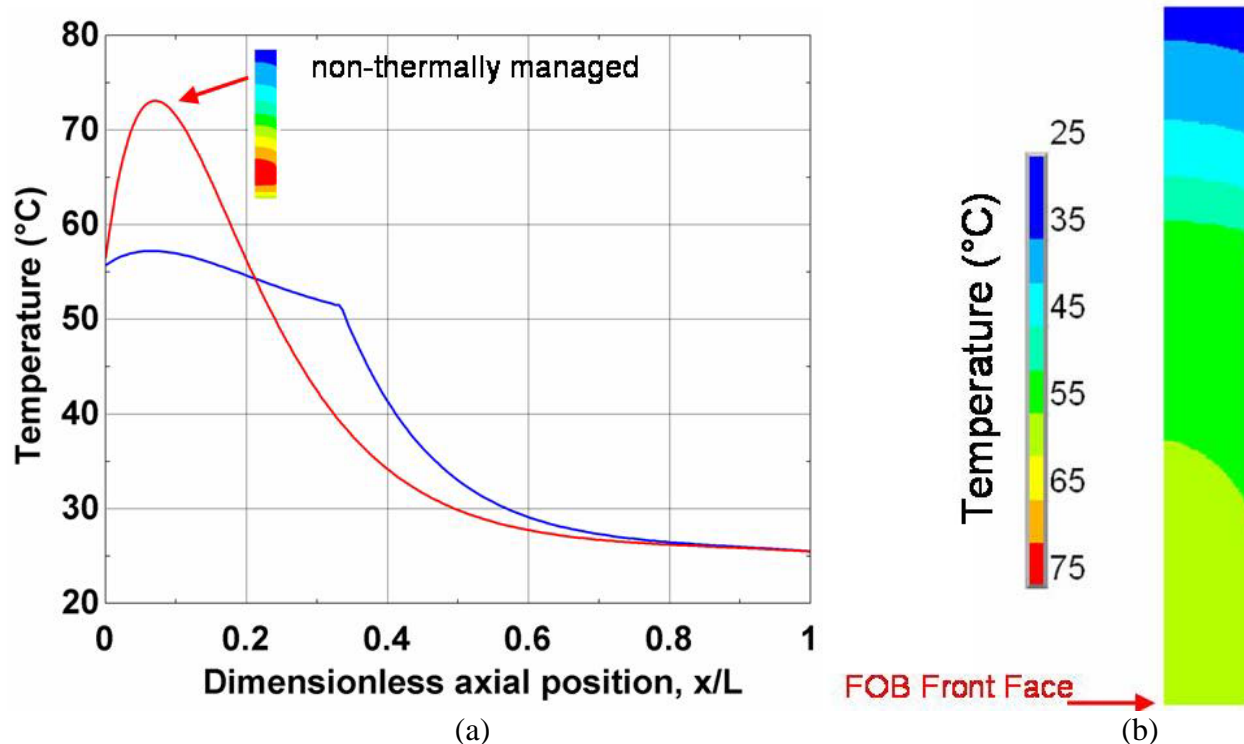


**Figure 5.5:** (a) Temperature as a function of dimensionless axial position within the experimental FOB. Temperature distributions are plotted for the non-thermally managed FOB and the thermally managed FOB of Fig. 5.4. Note that the inset image is a temperature contour plot of the non-thermally managed FOB. The temperature scale is the same as that shown in (b). (b) Temperature contour plot for the FOB with copper wire in pores.

Results of the experiment are shown in Fig. 5.6. The temperature rise from ambient is plotted as a function of dimensionless axial position within the FOB for two sets of experimental data. Both sets of experimental data were taken on the same day. The first set is for the FOB with no

thermal management. The second set is for the FOB shown in Fig. 5.4. The thermally managed FOB redistributes the energy down the length of the copper wire and reduces the maximum temperature in the FOB by approximately 5°C.

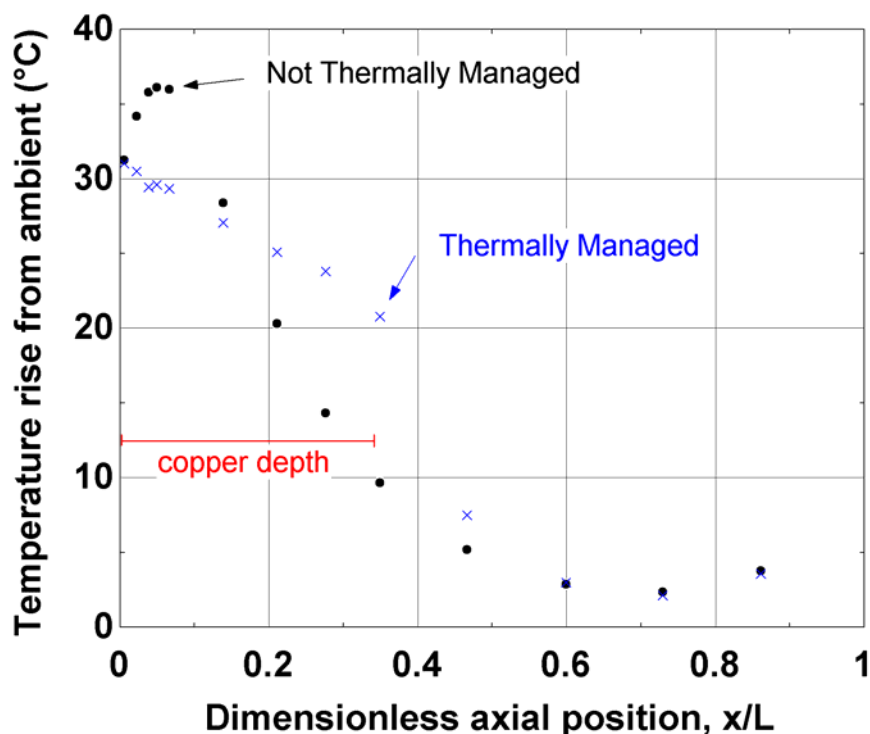


**Figure 5.6:** Temperature rise from ambient as a function of dimensionless axial position within the experimental FOB for a non-thermally managed FOB and a thermally managed FOB.

The energy provided by the light source had changed relative to its carefully measured value described in Chapter 2. Rather than measure the magnitude of the incident energy for these tests, the non-thermally managed and thermally managed experiments were carried out sequentially so that a direct comparison could be made. The reduction in the temperature rise from ambient relative to the non-thermally managed case was the most important parameter and can be compared with the 2-D FE model predictions even in the absence of accurate knowledge of the incident energy flux. Figure 5.7 shows the relative temperature rise measured by the experiment and predicted by the 2-D FE model; the relative temperature rise is defined as:

$$\text{relative temperature rise} = \frac{T_{tm} - T_a}{T_{ntm} - T_a} \quad (5.1)$$

where  $T_{tm}$  and  $T_{ntm}$  are the thermally managed and non-thermally managed temperature and  $T_a$  is the ambient temperature. By comparing the experimental and predicted results in this manner the effect of the unknown magnitude of the incident heat flux is removed; note that the predicted and measured relative temperature rise agree reasonably well.

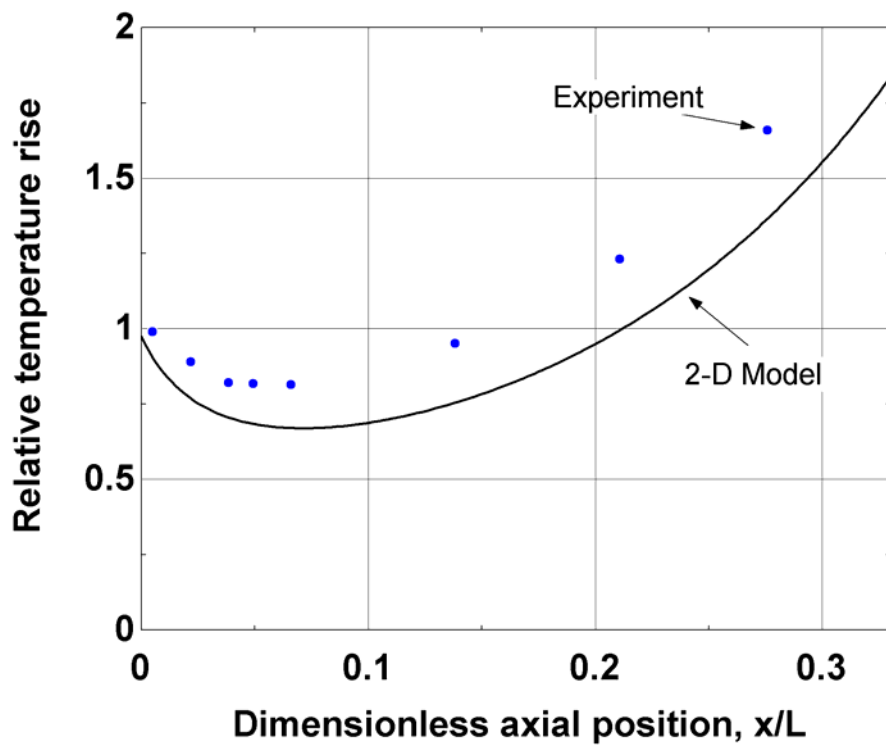


**Figure 5.7:** Relative temperature rise for the thermally managed vs. non-thermally managed FOB as a function of dimensionless axial position measured experimentally and predicted with the 2-D FE model. The presentation of the results of Figures 5.5 and 5.6 in this form removes the effect of the unknown incident energy.

## 5.4 Conclusions

Several thermal management strategies for an on-sun FOB were evaluated in this chapter; these strategies were passive and inexpensive as required by the economic constraints associated with an HSL system. The two thermal management designs that were considered included: 1) replacing a single fiber optic cable with a single copper rod and 2) displacing the air in the pores of the FOB with aluminum. Both strategies successfully reduced the maximum temperature rise within the FOB; however the FOB with the aluminum filled pores provided the most dramatic reduction in temperature and is therefore recommended as the most attractive option. An experiment was run in order to demonstrate the fidelity of the 2-D FE model for a thermally managed condition.

## Chapter 6

# Recommendations and Conclusions

### 6.1 Recommendations for future work

The primary focus of future work with the on-sun FOB should be the development of a thermally managed prototype. The development process should start with a non-thermally managed FOB that is thoroughly instrumented with thermocouples, similar to the instrumentation that was integrated with the experimental FOB described in Chapter 3. In addition, the assembly that houses the FOB should be instrumented with thermocouples. Temperatures should be measured at least at every interface (e.g. the interface of the FOB with the collet, the interface of the collet with the sleeve, etc.) so that experimental data can be compared with 2-D model predictions. These measurements should provide important data that would allow the 2-D model to be validated and refined. Also, both thermally managed configurations explored in Chapter 5, the single copper rod FOB and the aluminum filled pores FOB, should be built and similarly instrumented. The ambient temperature must be measured. The temperature data gathered from these experiments placed on-sun, when coupled with some measure of the incident flux, could be compared with the 2-D model predictions.

In order to be useful, the detailed temperature measurements must be accompanied by a measurement of the direct normal solar radiation; this could be accomplished using a pyrheliometer. Because the solar resource varies throughout the day, as well as from day to day, understanding how it varies provides an important parameter as to why the temperatures within the FOB vary from day to day. A direct measurement of the radiation flux incident on the face of the FOB would provide a useful comparison with the theoretical calculation given in Chapter 4. However, this measurement might prove to be more difficult due to the high level of heat flux imposed on the FOB face; possibly a pyrheliometer could be used in conjunction with a series of filters whose properties are well defined.

The on-sun experimental data described above are a function of time of day; however the 2-D model developed in Chapter 4 only predicts steady state temperature distributions. If the primary concern of model simulations is the prediction of maximum temperatures then the 2-D steady state model might be sufficient. However, the development of a 2-D transient model will likely be required to completely match the unsteady temperature data that will be collected from any real on-sun FOB system. Also, the transient thermal behavior of the FOB may be important relative to understanding the cyclic thermal stresses that are seen by this component.

## **6.2 Summary**

HSL systems designed to collect visible solar radiation for use as indoor lighting rely on a plastic FOB to transmit collected solar radiation to the interior of commercial buildings. The thermal failure of these FOBs due to the high thermal loads caused by very concentrated solar radiation has motivated the development of the 2-D FE model described in Chapter 4. An analytical 1-D

model and an experiment both were used to develop this 2-D FE model. The power of the 2-D FE model is its ability to evaluate arbitrary thermal management strategies. The ultimate objective of this project was the development of an FOB design that is capable of surviving indefinitely under the conditions associated with continuous on-sun loading. The on-sun FOB with aluminum filled pores appears to fulfill this requirement without resulting in a substantial increase in HSL cost or complexity; however, additional experimental work should be carried out on a prototype system in order to verify this design.

## References

- Aleksic, R.R., Jancic, R.M., “Coherent Optical Fiber Bundles Production,” *Materials Science Forum*, Vol. 214, 1996, pp. 73-80
- ANSYS Inc., Southpointe 275 Technology Drive Canonsburg, PA ([www.ANSYS.com](http://www.ANSYS.com)), 2005.
- Burkholder, Frank. *TRNSYS Modeling of a Hybrid Lighting System: Energy Savings and Colorimetry Analysis*, Solar Energy Laboratory, University of Wisconsin – Madison, USA, June 2004
- Department of Energy, Energy Information Administration, available at <http://www.eia.doe.gov>, 2005.
- Duffie, J.A. and Beckman, W.A., *Solar Engineering of Thermal Processes*, 2<sup>nd</sup> Ed., John Wiley and Sons, 1991.
- Earl, D.D., Maxey, C.L., Muhs, J.D., “Performance of New Hybrid Solar Lighting Luminaire Design,” International Solar Energy Conference, Kohala Coast, Hawaii Island, March 15-18, 2003.
- Fraas, L.M., Daniels, W.E., Muhs, J.D., “Infrared Photovoltaics for Combined Solar Lighting and Electricity for Buildings,” Proceedings of the 17th European Photovoltaic Solar Energy Conference, Munich, Germany, October 22-26, 2001.
- Fraas, L.M., Avery, J.E., Nakamura, T., “Electricity from Concentrated Solar IR in Solar Lighting Applications,” 29<sup>th</sup> IEEE Photovoltaic Specialists Conference, May 20-24, 2002.
- Gueymard, C., *SMARTS, A Simple Model of the Atmospheric Radiative Transfer of Sunshine: Algorithms and Performance Assessment*, Professional Paper FSEC-PF-270-95. Florida Solar Energy Center, 1679 Clearlake Road, Cocoa, FL 32922, 1995
- Gueymard, C., *Parameterized Transmittance Model for Direct Beam and Circumsolar Spectral Irradiance*, *Solar Energy*, Vol. 71, No. 5, pp. 325-346, 2001
- Huber, N., Heitz, J., Bäuerle, D., *Pulsed-Laser Ablation of Polytetrafluoroethylene (PTFE) at Various Wavelengths*, *Applied Physics*, Vol. 25, 2004, pg. 33-38.
- Illuminating Engineering Society of North America (IESNA), *The IESNA Lighting Handbook: Reference and Application*, Illuminating Engineering Society of North America, New York, N.Y., 2000.
- Kanzaki, H., Sato, K., and Kumagai, M., *A Study of an Estimation Method for Predicting the Equivalent Thermal Conductivity of an Electric Coil*, *JSME*, 56 (526), 1990, 1752-1758.

- Klein, S.A., et al., *EES, Engineering Equation Solver*, Solar Energy Laboratory, University of Wisconsin – Madison, USA, 2005.
- Klein, S.A., et al., *TRNSYS, A Transient Simulation Program*, Solar Energy Laboratory, University of Wisconsin – Madison, USA, 2000.
- Maxey, L.D., Cates, M.R., Jaiswal, S.L., *Efficient Optical Couplings for Fiber Distributed Solar Lighting*, International Solar Energy Conference, Kohala Coast, Hawaii Island, March 15-18, 2003.
- Muhs, J.D., *Design and Analysis of Hybrid Solar Lighting and Full Spectrum Solar Energy Systems*, Proceedings of the American Solar Energy Society, Solar 2000, June 16-21, 2000a.
- Muhs, J.D., *Hybrid Lighting Doubles the Efficiency and Affordability of Solar Energy in Commercial Buildings*, CADDET- Energy Efficient News Letter, No. 4, 2000b, 6 - 9.
- Muhs, J.D., Earl, D.D., Beshears, D., Maxey, L.D. *Results from an Experimental Hybrid Solar Lighting System Installed in a Commercial Building* International Solar Energy Conference, Kohala Coast, Hawaii Island, March 15-18, 2003.
- McMaster-Carr, available at <http://www.mcmaster.gov>, 2005.
- Mitsubishi Rayon Co., LTD. ESKA Optical Fiber Division. *Specification Sheet CK-120*, 2001.
- Oak Ridge National Laboratory, available at <http://www.ornl.gov>, 2005.
- Oriel Instruments Catalog. *The Big Book of Photon Tools*, 2004.
- Osswald, T.A., *Polymer Processing Fundamentals*, Carl Hanser Verlag, Munich 1998.
- Riedel, D., Castex, M.C., *Effective Absorption Coefficient Measurements in PMMA and PTFE by Clean Ablation Process with a Coherent VUV source at 125 nm*, Applied Physics, Vol. 69, 1999, pg. 375-380.
- Schlegel, G.O., *A TRNSYS Model of a Hybrid Lighting System*, Solar Energy Laboratory, University of Wisconsin – Madison, USA, June 2003
- Schlegel, G., Burkholder, F., et al., *Analysis of a Full Spectrum Hybrid Lighting System*, Solar Energy, Vol. 76, 2004, pp. 359-368
- Siegel, R., and Howell, J., *Thermal Radiation Heat Transfer*, 4<sup>th</sup> Ed., Taylor and Francis, 2002.
- Tekelioglu, M., Wood, B.D., *Thermal Management of the Polymethylmethacrylate (PMMA) Core Optical Fiber for use in Hybrid Solar Lighting*, International Solar Energy Conference, Kohala Coast, Hawaii Island, March 15-18, 2003.

## Appendix

### EES Code

#### Calculation of Effective Axial Conductivity

```

phi_core=1-phi_pore"Fraction of FOB face that is PMMA"
phi_clad=ratio*phi_core"Fraction of FOB face that is cladding. Always a fraction of how much PMMA
there is."
phi_fill=1-phi_core-phi_clad"Fraction of FOB face that is filling material (air).
ratio=.03454

k_core=.18 [W/m-K]"Conductivity of PMMA"
k_clad=.23 [W/m-K]"Conductivity of cladding"
k_fill=.027"Conductivity of filling material (air)."

k_eff=phi_core*k_core+phi_clad*k_clad+phi_fill*k_fill"Effective axial conductivity"

```

#### Calculation of Effective Radial Conductivity

```

Lambda_bar_x= 2 * SQRT(3) * ( INT_1 + INT_2)

INT_1= INTEGRAL(((lambda_1 * lambda_2) / ((lambda_2 - lambda_1) * SQRT(ABS(F^2-y^2)) +
SQRT(3) * lambda_1)),y,0,1-F)
INT_2=INTEGRAL(((lambda_1 * lambda_2) / (( lambda_1 - lambda_2) * (SQRT(3) - SQRT(ABS(F^2-
y1^2)) - SQRT(ABS(F^2-(y1-1)^2)))) + SQRT(3) * lambda_2)),y1,1-F,0.5)

Lambda_bar_y= 2 / SQRT(3) * ( INT_3 + INT_4)

INT_3= INTEGRAL(((lambda_1 * lambda_2) / ((lambda_2 - lambda_1) * SQRT(ABS(F^2-x^2)) +
lambda_1)),x,0,SQRT(3)-F)
INT_4=INTEGRAL(((lambda_1 * lambda_2) / ((lambda_1 - lambda_2) * (1 - SQRT(ABS(F^2- x1^2)) -
SQRT(ABS(F^2-(x1- SQRT(3))^2)))) + lambda_2)),x1,SQRT(3)-F,(SQRT(3))/2)

Lambda_bar=(Lambda_bar_x + Lambda_bar_y)/2

phi_1=1-(phi_23)"PMMA only"
phi_2 =.03454*phi_1"CLAD only"
phi_12= phi_1+phi_2"PMMA and CLAD"
phi_23=phi_2+phi_3"GAPS and CLAD"

F= SQRT( (2 * SQRT(3) * phi_1 )/ PI)

lambda_1=.18"Conductivity of PMMA"

lambda_2=.23"Conductivity of Cladding"

lambda_3=.027"Conductivity of Air"

lambda_2=(phi_2 * lambda_2 + phi_3 * lambda_3)/(phi_2 + phi_3)

```

## Calculation of Front, Rear Face and Edge Heat Transfer Coefficients

```
"===Churchill and Chu Correlations for 1D Model==="
```

```
"=====
```

```
"---Churchill and Chu Correlation For Flat Plate. pg546 I&D.---"
```

```
FUNCTION NuL(Ra_L,Pr)
NuL:=.68+(.67*Ra_L^(.25))/(1+(.492/Pr)^(9/16))^(4/9)
END
```

```
"---Average Nusselt# for Cylinder Laminar flow. pg410 I&D.---"
```

```
FUNCTION NuD_bar(Re_D,Pr)
C:=.193
m:=.618
NuD_bar:=C*Re_D^m*Pr^(1/3)
END
```

```
"=====
```

```
"=====
```

```
"===Calculating Natural Convection Coefficient for 1D Model==="
```

```
"<<<Front and back face of FOB assumed to be square with some L_char based on
A_circle=A_square>>>"
"<<<Laminar flow assumed unless otherwise noted.>>>"
```

```
"=====
```

```
"<<NATURAL CONVECTION from face>>"
```

```
procedure h_nat(T_s,T_surr:h)
```

```
"---Constants and Miscellaneous---"
```

```
g=g#"gravitational constant"
sigma=sigma#"Boltzman's constant"
P1=101.3 [kPa]"Atmospheric pressure"
epsilon_ins=.8"emissivity of insulation"
epsilon_PMMA=.8"emissivity of PMMA"
k_ins=.026[W/m-K]"conductivity of insulation"
```

```
"---Geometry of fibers, FOB and Insulation---"
```

```
N=120"Number of fibers"
r_fiber=.0015[m]"Radius of single fiber"
r_bundle=.01849[m]"Outer radius of FOB"
r_ins=.04109"Outer radius of insulation"
L=.3[m]"Length of FOB"
D_ins=r_ins*2"Diameter of Insulation"
A_s=2*pi*r_ins*L"Surface area of insulation"
A_FOB=2*pi*r_bundle*L"Surface area of FOB"
A_face=r_bundle^2*pi"Area of FOB face, not including insulation"
A_fibers=N*pi*r_fiber^2
A_bundle=pi*r_bundle^2
```

```
T_f=(T_s+T_surr)/2"Film temperature [C]"
```

```
T_f_K=convertTemp(C,K,T_f)"Film temperature [K]"
```

```
T_surr_K=convertTemp(C,K,T_surr)
```

```

T_s_K=convertTemp(C,K,T_s)
beta=1/T_f_K"Beta for natural convection calculation"

"---Parameters of Air at T_f---"
rho=DENSITY(Air,T=T_f,P=P1)"Density of air at P1"
Cp=CP(Air,T=T_f)*convert(kJ,J)"Specific heat of air at T1"
nu=VISCOSITY(Air,T=T_f)/DENSITY(Air,T=T_f,P=P1)"kinematic viscosity of air at T1 and P1"
Pr=PRANDTL(Air,T=T_f)"Prandtl number of air at T1"
k_air=CONDUCTIVITY(Air,T=T_f)"Conductivity of air"
alpha_air=k_air/(rho*Cp)"thermal diffusivity of air at T1 and P1"

"---Characteristic length of FOB face. Assumed to be square, not circle---"
L_char=sqrt(A_face)

"---Natural Convection Across FOB face---"
Ra_L=(g*beta*(T_s-T_surr)*L_char^3)/(nu*alpha_air)
NuL_bar=NuL(Ra_L,Pr)
h_bar_L=NuL_bar*k_air/L_char

"---Radiation From FOB Face---"
h_r=epsilon_PMMA*sigma*(T_s_K+T_surr_K)*(T_s_K^2+T_surr_K^2)"Radiation convection coefficient
across FOB face"

"---Total HT Coefficient For Front Face of FOB---"
h1=h_r+h_bar_L
h=h1*A_fibers/A_bundle
end
=====
=====
"
"=====
"
"<h effective>>"
procedure h_eff(T_s,T_surr:heff)

"---Constants and Miscellaneous---"
g=g#"gravitational constant"
sigma=sigma#"Boltzman's constant"
P1=101.3 [kPa]"Atmospheric pressure"
epsilon_ins=.8"emissivity of insulation"
epsilon_PMMA=.8"emissivity of PMMA"
k_ins=.026[W/m-K]"conductivity of insulation"

"---Geometry of fibers, FOB and Insulation---"
N=120"Number of fibers"
r_fiber=.0015[m]"Radius of single fiber"
r_bundle=.01849[m]"Outer radius of FOB"
r_ins=.04109"Outer radius of insulation"
L=.3[m]"Length of FOB"
D_ins=r_ins*2"Diameter of Insulation"
A_s=2*pi*r_ins*L"Surface area of insulation"
A_FOB=2*pi*r_bundle*L"Surface area of FOB"
A_face=r_bundle^2*pi"Area of FOB face, not including insulation"
A_fibers=N*pi*r_fiber^2

T_f=(T_s+T_surr)/2"Film temperature [C]"

```

```

T_f_K=convertTemp(C,K,T_f)"Film temperature [K]"
T_surr_K=convertTemp(C,K,T_surr)
T_s_K=convertTemp(C,K,T_s)
beta=1/T_f_K"Beta for convection calculation"

"---Parameters of Air and Insulation at T_f---"
rho=DENSITY(Air,T=T_f,P=P1)"Density of air at P1"
Cp=CP(Air,T=T_f)*convert(kJ,J)"Specific heat of air at T1"
nu=VISCOSITY(Air,T=T_f)/DENSITY(Air,T=T_f,P=P1)"kinematic viscosity of air at T1 and P1"
Pr=PRANDTL(Air,T=T_f)"Prandtl number of air at T1"
k_air=CONDUCTIVITY(Air,T=T_f)"Conductivity of air"
alpha_air=k_air/(rho*Cp)"thermal diffusivity of air at T1 and P1"

"---Convection Across Insulation---"
Ra_D=(g*beta*(T_s-T_surr)*D_ins^3)/(nu*alpha_air)
NuD_bar=NuD(Ra_D,Pr)
h_bar_D=NuD_bar*k_air/D_ins

"---Radiation From Insulation---"
h_r=epsilon_ins*sigma*(T_s_K+T_surr_K)*(T_s_K^2+T_surr_K^2)"Radiation convection coefficient
across Collet"

"---Resistance to Convection and Radiation at Surface of Insulation--"
R_rad=1/(h_r*A_s)
R_conv=1/(h_bar_D*A_s)
R_cr=1/(1/R_rad+1/R_conv)

"---Resistance to Conductive HT in Insulation---"
R_cond=ln(r_ins/r_bundle)/(2*pi*L*k_ins)

"---Effective Resistance to Conductive, Convective and Radiation Resistances---"
R_eff=R_cr+R_cond
heff=1/(R_eff*A_FOB)
end
"=====
=====

```

## Calculation of the Characteristic Length Associated with the Pores

```

"---Characteristics of Incident Light---"
f=f_max*(1-theta_entrance/theta_final)
theta_final=30
$IFNOT MINMAX
f_max=.06667
$ENDIF
f_minimize=abs(f_sum-1)
f_sum=integral(f,theta_entrance,0,theta_final)
$integralTable theta_entrance:.1 f,beta,beta_f,beta_eff

"===Program To Calculate Beta for Heat Generation===
"---General Parameters---"
delta_core=1.5[mm]"radius of core"
delta_fill=.25[mm]"width of filling"
delta_cladding=.025[mm]"width of cladding"

```

n\_core=1.49"index of refraction for core"  
 n\_fill=1"index of refraction for filler"  
 n\_cladding=1.4"index of refraction for cladding"

"---Refraction Angles and Indices---"

theta\_fill=90[deg]-theta\_entrance"angle of light (from normal) entering into cladding"  
 x\_fill=(delta\_fill)\*tan(theta\_fill)"distance traveled in x direction as ray passes through the filling"

n\_fill\*sin(theta\_fill)=n\_cladding\*sin(theta\_clad)"Snell's law for filling to cladding interface. Angle of light (from normal) entering into core"  
 x\_cladding=(delta\_cladding)\*tan(theta\_clad)"distance traveled in x direction as ray passes through the cladding"

n\_cladding\*sin(theta\_clad)=n\_core\*sin(theta\_core)"Snell's law for cladding to core interface"  
 x\_core=(delta\_core)\*tan(theta\_core)"distance traveled in x direction as ray passes through the core"

"---Path Lengths per Unit z\_travel---"

s\_clad=x\_cladding/sin(theta\_clad)"distance traveled through the cladding"  
 x\_o=x\_fill+x\_cladding+x\_core"total distance traveled in the x direction"  
 beta=s\_clad/x\_o"ratio of distance traveled through the cladding to the distance traveled total in the x direction"  
 beta\_f=beta\*f"product beta\*f\_percent"

"---Effective Beta---"

beta\_eff=integral(beta\_f,theta\_entrance,0,theta\_final)"effective beta"  
 alpha=15[1/cm]\*convert(1/cm,1/m)"absorption coefficient"  
 L\_ch\_alpha=1/(alpha\*beta\_eff+1E-10[1/m])\*convert(m,mm)"characteristic length"

## 1-D Model Temperature Predictions within the Experimental FOB

"---Given Information---"

q\_dot\_flux\_inc=3000[W/m^2] "energy flux incident on face"  
 {nominal is 3000 W/m^2 error is near 20%. 2400W/m^2 - 3600W/m^2}  
 L\_ch\_f=22.2[m]"characteristic length for absorption of energy in fibers"  
 L\_ch\_alpha=.026"characteristic length for absorption of energy in the gaps"  
 k\_eff\_ax=.15[W/m-C]"effective conductivity for bundle in axial direction"  
 k\_eff\_r=.1148[W/m-C]"effective conductivity for bundle in radial direction"  
 N=120"number of fibers in the bundle"  
 r\_bundle = 0.0184[m]"radius of the bundle"  
 L=0.3[m]"length of bundle"  
 p=2\*pi\*r\_bundle"perimeter of bundle"  
 T\_a=25[C]"ambient temp"  
 eps=.24"fraction of bundle that is air gap"  
 m=sqrt((2\*h\_edge)/(k\_eff\_ax\*r\_bundle))"fin constant for bundle"  
 Biot=h\_edge\*r\_bundle/k\_eff\_r"Biot number for bundle"

"---Constnats Relating to Particular Solution of Governing Equation (solved explicitly)---"

C\_3=q\_dot\_flux\_inc\*(1-eps)/(L\_ch\_f\*k\_eff\_ax)/(m^2-1/L\_ch\_f^2)  
 C\_4=q\_dot\_flux\_inc\*eps/(L\_ch\_alpha\*k\_eff\_ax)/(m^2-1/L\_ch\_alpha^2)

"---Boundary Conditions Applied to Governing Equation---"

h\_front\_face\*(C\_1+C\_2+C\_3+C\_4)=k\_eff\_ax\*(C\_1\*m-C\_2\*m-C\_3/L\_ch\_f-C\_4/L\_ch\_alpha)  
 h\_rear\_face\*(C\_1\*exp(m\*L)+C\_2\*exp(-m\*L)+C\_3\*exp(-L/L\_ch\_f)+C\_4\*exp(-L/L\_ch\_alpha))=  
 k\_eff\_ax\*(C\_1\*m\*exp(m\*L)-C\_2\*m\*exp(-m\*L)-C\_3\*exp(-L/L\_ch\_f)/L\_ch\_f-C\_4\*exp(-  
 L/L\_ch\_alpha)/L\_ch\_alpha)

```

Nodes=200
Dx=L/Nodes
duplicate i=0,Nodes
    x[i]=i*Dx
    X_bar[i]=x[i]/.3
    Theta[i]=C_1*exp(m*x[i])+C_2*exp(-m*x[i])+C_3*exp(-x[i]/L_ch_f)+C_4*exp(-x[i]/L_ch_alpha)
end

h_edge=1.1[W/m^2-C]
call h_nat(Theta[1]+T_a+1E-10[C],T_a:h_front_face)
call h_nat(Theta[Nodes]+T_a+1E-10[C],T_a:h_rear_face)

```

## MATLAB Code

### Calculation of Porosity and Heat Generation

```

w=imread('FOBface1.jpg');
select_exp;

for x=1:1311
for y=1:1257
p(y,x)=w((x-1)*1257+y);
end
end

for x=1:1311
for y=1:1257
    if p(y,x)>=128
        q(y,x)=255;
    else
        q(y,x)=0;
    end
end
end

y0=640; %center of FOB
x0=652; %center of FOB
r0=629; %outer radius of FOB
N=300; %number of annuli
Dr=r0/N;%width of radial annuli

%Loop to calculate the porosity of N annuli
for i=1:N

r_inner(i)=(i-1)*Dr;%inner radius of annulus i
r_outer(i)=i*Dr;%outer radius of annulus i

```

```

r_ave(i)=(r_outer(i)-r_inner(i))/2+r_inner(i);%average radius of annulus i

black(i)=0;%# of black pixels at start of count
white(i)=0;%# of white pixels at start of count
gray(i)=0; %# of gray pixels at start of count

%Loop for calculating radius of pixel (y,x)
%And for selecting if it is within r_inner and r_outer
for x=1:1311
for y=1:1257
    r(y,x)=sqrt((y-y0)^2+(x-x0)^2);%radius of pixel (y,x)
    if (r(y,x)>r_inner(i)&(r(y,x)<=r_outer(i))
        a(y,x)=q(y,x);%new array 'a' delimits the pixels within the annulus i
    else
        a(y,x)=200;%all other values of 'a' are made gray
    end
end
end

%Loop for counting the number of black, white and gray pixels
for x=1:1311
for y=1:1257
    if a(y,x)==255
        white(i)=white(i)+1;%number of white pixels in annulus i
    elseif a(y,x)==0
        black(i)=black(i)+1;%number of black pixels in annulus i
    else
        gray(i)=gray(i)+1;%number of gray pixels in annulus i
    end
end
end

overall(i)=black(i)+white(i)+gray(i);%total number of pixels in annulus i and surrounding
check(i)=1311*1257;%total number of pixels in picture
total(i)=black(i)+white(i);%total number of pixels in annulus i
por(i)=black(i)/total(i);%porosity of annulus i

end
bl=sum(black);%total number of black pixels in r0
wh=sum(white);%total number of white pixels in r0
to=sum(total);%total number of pixels in r0

M=100; %number of axial segments
L=.3; %length of FOB
Dy=L/M; %width of axial segment

```

```

for i=1:M+1
    y(i)=Dy*(i-1);% axial position at node i
end

q_inc=3000; %incident heat flux
L_ch_tau=22.2; %characteristic length of fibers
L_ch_alpha=.026;%characteristic length of gaps

for i=1:M+1% axial (column)
    for j=1:N%radial (row)
gen(j,i)=(q_inc/L_ch_tau)*(1-por(j))*exp(-y(i)/L_ch_tau)+(q_inc/L_ch_alpha)*por(j)*exp(-
y(i)/L_ch_alpha);
        end
    end

r_ave_t=transpose(r_ave);
por_t=transpose(por);
r_m=r_ave_t*.0184/629;

```

## ANSYS Code

### 2-D Model Temperature Predictions within the Experimental FOB

```

abbres,new,mybuttons_INF

/prep7

*DIM,HGEN,TABLE,300,101,1,x,y,,
*TREAD,HGEN,'C:\Documents and
Settings\mchadle.000\Desktop\ANSYS\Tables\ExpHGEN','txt', , ,

*DIM,CON,TABLE,2000,1,1,TEMP,,,
*TREAD,CON,'C:\Documents and
Settings\mchadle.000\Desktop\ANSYS\Tables\hFace','txt', , ,

!set CS to cylindrical
csys,5

!create geometry
!for cylindrical coordinates
!k,p#,radius,theta,length
k,1,0,0,0
k,2,0.0017,0,0
k,3,0.0033,0,0
k,4,0.005,0,0

```

k,5,0.0067,0,0  
k,6,0.0084,0,0  
k,7,0.01,0,0  
k,8,0.0117,0,0  
k,9,0.0134,0,0  
k,10,0.0151,0,0  
k,11,0.0167,0,0  
k,12,0.0184,0,0

k,13,0,0,0.3  
k,14,0.0017,0,0.3  
k,15,0.0033,0,0.3  
k,16,0.005,0,0.3  
k,17,0.0067,0,0.3  
k,18,0.0084,0,0.3  
k,19,0.01,0,0.3  
k,20,0.0117,0,0.3  
k,21,0.0134,0,0.3  
k,22,0.0151,0,0.3  
k,23,0.0167,0,0.3  
k,24,0.0184,0,0.3

l,1,2  
l,2,3  
l,3,4  
l,4,5  
l,5,6  
l,6,7  
l,7,8  
l,8,9  
l,9,10  
l,10,11  
l,11,12

l,13,14  
l,14,15  
l,15,16  
l,16,17  
l,17,18  
l,18,19  
l,19,20  
l,20,21  
l,21,22  
l,22,23  
l,23,24

1,1,13  
1,2,14  
1,3,15  
1,4,16  
1,5,17  
1,6,18  
1,7,19  
1,8,20  
1,9,21  
1,10,22  
1,11,23  
1,12,24

al,1,12,23,24  
al,2,13,24,25  
al,3,14,25,26  
al,4,15,26,27  
al,5,16,27,28  
al,6,17,28,29  
al,7,18,29,30  
al,8,19,30,31  
al,9,20,31,32  
al,10,21,32,33  
al,11,22,33,34

!define material paramters  
!material 1, hex packed equivalent properties  
!Equivalence Calculated in EES  
!phi\_1=  
mp,kxx,1,.1317  
mp,kyy,1,.1567

!phi\_1=  
mp,kxx,2,.1364  
mp,kyy,2,.1588

!phi\_1=  
mp,kxx,3,.1186  
mp,kyy,3,.1505

!phi\_1=  
mp,kxx,4,.1498  
mp,kyy,4,.1645

```
!phi_1=  
mp,kxx,5,.1337  
mp,kyy,5,.1576
```

```
!phi_1=  
mp,kxx,6,.1285  
mp,kyy,6,.1552
```

```
!phi_1=  
mp,kxx,7,.1478  
mp,kyy,7,.1636
```

```
!phi_1=  
mp,kxx,8,.1245  
mp,kyy,8,.1533
```

```
!phi_1=  
mp,kxx,9,.1241  
mp,kyy,9,.1532
```

```
!phi_1=  
mp,kxx,10,.1232  
mp,kyy,10,.1527
```

```
!phi_1=  
mp,kxx,11,.06502  
mp,kyy,11,.1133
```

```
!element type
```

```
et,1,plane77  
keyopt,1,3,1
```

```
!mesh
```

```
esize,.001  
mat,1  
amesh,1,1,1
```

```
mat,2  
amesh,2,2,1
```

```
mat,3  
amesh,3,3,1
```

mat,4  
amesh,4,4,1

mat,5  
amesh,5,5,1

mat,6  
amesh,6,6,1

mat,7  
amesh,7,7,1

mat,8  
amesh,8,8,1

mat,9  
amesh,9,9,1

mat,10  
amesh,10,10,1

mat,11  
amesh,11,11,1

!apply loads and IC

!FOB face lines  
!due to convection and radiation  
lsel,all  
lsel,s,line,,1,22,1  
sfl,all,conv,%CON%,,25

!edge coefficient  
!due to convection and radiation  
!from insulation surface and  
!conduction through insulation  
!average coefficient  
lsel,all  
sfl,34,conv,1.1,,25

!set initial conditions  
nset,all  
ic,all,temp,25

!HGEN\_3000

```
asel,all
BFA,all,hgen,%hgen%
```

```
!Solve current LS
```

```
/solu
solve
```

```
!General Post Processor
```

```
/post1
```

```
/graphics,full
/triad,off
/plopts,leg1,0
/plopts,date,0
/plopts,minm,0
/plopts,frame,0
/udoc,1,cntr,left
/contour,all,10,25,5
```

```
plnsol,temp
```

## 2-D Model Temperature Predictions within the On-Sun FOB

```
abbres,new,mybuttons_INF
```

```
/prep7
```

```
*DIM,HGEN, TABLE,374,101,1,x,y,,
*TREAD,HGEN,'C:\Documents and
Settings\mcheadle.000\Desktop\ANSYS\Tables\OnSunHGEN','txt', , ,
```

```
*DIM,CONFACE, TABLE,2000,1,1,TEMP,,
*TREAD,CONFACE,'C:\Documents and
Settings\mcheadle.000\Desktop\ANSYS\Tables\hFace','txt', , ,
```

```
*DIM,CONEDGE, TABLE,2000,1,1,TEMP,,
*TREAD,CONEDGE,'C:\Documents and
Settings\mcheadle.000\Desktop\ANSYS\Tables\hEdge','txt', , ,
```

```
!csys,5
et,1,plane77
keyopt,1,3,1
```

```

!define FOB perimeter
k,1,0,0.50402,0
k,2,0.0166,0.50402,0
k,3,0.0185547,0.20402,0
k,4,0,0.20402,0
k,5,.0185547,0.28403,0
k,30,0.001509,0.50402,0!!!!!!!!!!!!!!!!!!!!!!!!!!!!!!
k,51,0.0166,0.20402,0
k,40,0.0166,0.28403,0

```

```

l,1,30
l,2,40
l,5,3
l,3,51

```

```

!define collet perimeter
k,6,0.037973,0.28403,0
k,7,0.037973,0.27133,0
k,8,0.0231267,0.27133,0
k,9,0.0231267,0.20402,0

```

```

l,5,6
l,6,7
l,7,8
l,8,9
l,9,3

```

```

!define sleeve preimeter
k,10,0.055753,0.27133,0
k,11,0.055753,0.25863,0
k,12,0.037973,0.25863,0
k,13,0.037973,0.19132,0
k,14,0.026162,0.19132,0
k,15,0.026162,0.06559,0
k,16,0.018554700,0.047175,0
k,17,0.018554700,0.05289,0
k,18,0.02032,0.06559,0
k,19,0.02032,0.20148,0
k,20,0.018554700,0.20148,0

```

```

l,7,10
l,10,11
l,11,12
l,12,13
l,13,14
l,14,15

```

l,15,16

l,16,17

l,17,18

l,18,19

l,19,20

l,20,3

!define PMMA perimeter

k,21,0,0.05289,0

l,20,17

l,17,21

l,21,4

!define Glass cover perimeter

k,22,0,0.047175,0

l,16,22

l,22,21

!define Collar perimeter

k,23,0.15875,0.25863,0

k,24,0.15875,0.19132,0

k,25,0.13875,0.19132,0

l,11,23

l,23,24

l,24,25

l,25,13

!define dish perimeter

k,26,.58875,0.003,0

larc,24,26,16,1.118915

k,27,.58875,0.0,0

l,26,27

k,28,0.15875,0.18832,0

larc,27,28,16,1.118915

k,29,0.13875,0.18832,0

l,28,29

l,29,25

!define edge

l,40,51

!define FOB Guts!!

k,31,0.003018,0.50402,0  
k,32,0.004527,0.50402,0  
k,33,0.006036,0.50402,0  
k,34,0.007545,0.50402,0  
k,35,0.009055,0.50402,0  
k,36,0.01056,0.50402,0  
k,37,0.01207,0.50402,0  
k,38,0.01358,0.50402,0  
k,39,0.01509,0.50402,0

k,41,0.001509,0.20402,0  
k,42,0.003018,0.20402,0  
k,43,0.004527,0.20402,0  
k,44,0.006036,0.20402,0  
k,45,0.007545,0.20402,0  
k,46,0.009055,0.20402,0  
k,47,0.01056,0.20402,0  
k,48,0.01207,0.20402,0  
k,49,0.01358,0.20402,0  
k,50,0.01509,0.20402,0

l,30,31  
l,31,32  
l,32,33  
l,33,34  
l,34,35  
l,35,36  
l,36,37  
l,37,38  
l,38,39  
l,39,2  
l,40,5

l,51,50  
l,50,49  
l,49,48  
l,48,47  
l,47,46  
l,46,45  
l,45,44  
l,44,43

1,43,42  
1,42,41  
1,41,4

k,52,0,.28403,0  
k,53,0.001509,0.28403,0  
k,54,0.003018,0.28403,0  
k,55,0.004527,0.28403,0  
k,56,0.006036,0.28403,0  
k,57,0.007545,0.28403,0  
k,58,0.009055,0.28403,0  
k,59,0.01056,0.28403,0  
k,60,0.01207,0.28403,0  
k,61,0.01358,0.28403,0  
k,62,0.01509,0.28403,0

1,4,52  
1,52,1

1,52,53  
1,53,54  
1,54,55  
1,55,56  
1,56,57  
1,57,58  
1,58,59  
1,59,60  
1,60,61  
1,61,62  
1,62,40

1,30,53  
1,31,54  
1,32,55  
1,33,56  
1,34,57  
1,35,58  
1,36,59  
1,37,60  
1,38,61  
1,39,62

1,53,41  
1,54,42  
1,55,43  
1,56,44

1,57,45  
1,58,46  
1,59,47  
1,60,48  
1,61,49  
1,62,50

!define areas  
!FOB  
al,61,59,58,82  
!collet  
al,3,5,6,7,8,9  
!sleeve  
lsl,s,,7,21,1  
al,all,11  
lsl,all  
!PMMA rod  
lsl,s,,48,58,1  
lsl,a,,4,4,1  
lsl,a,,21,24,1  
al,all,48  
lsl,all  
!Glass cover  
al,23,17,25,26  
!Air gap  
al,19,18,22,20  
!Collar  
al,12,27,28,29,30,13  
!dish  
al,29,31,32,33,34,35  
!FOB Slices  
al,62,57,83,82  
al,63,56,84,83  
al,64,55,85,84  
al,65,54,86,85  
al,66,53,87,86  
al,67,52,88,87  
al,68,51,89,88  
al,69,50,90,89  
al,70,49,91,90  
al,71,48,36,91  
  
!edge  
al,47,3,4,36

!FOB tail  
al,61,60,72,1  
al,62,72,73,37  
al,63,73,74,38  
al,64,74,75,39  
al,65,75,76,40  
al,66,76,77,41  
al,67,77,78,42  
al,68,78,79,43  
al,69,79,80,44  
al,70,80,81,45  
al,71,81,2,46

!collet props  
esize,.0016  
mp,kxx,2,237  
mat,2  
amesh,2

!sleeve props  
mp,kxx,3,237  
mat,3  
amesh,3

!PMMA props  
mp,kxx,4,.18  
mat,4  
amesh,4

!glass props  
mp,kxx,5,1.4  
amesh,5

!air props  
mp,kxx,6,.027  
mat,6  
amesh,6

!collar props  
mp,kxx,7,237  
mat,7  
amesh,7

!dish props  
mp,kxx,8,.18  
mat,8

amesh,8

!FOB props  
!esize,.0005  
mp,kxx,1,.1707  
mp,kyy,1,.1739  
mat,1  
amesh,1  
amesh,20

!FOB Slices  
mp,kxx,9,.1706  
mp,kyy,9,.1738  
mat,9  
amesh,9  
amesh,21

mp,kxx,10,.1664  
mp,kyy,10,.1718  
mat,10  
amesh,10  
amesh,22

mp,kxx,11,.1725  
mp,kyy,11,.1748  
mat,11  
amesh,11  
amesh,23

mp,kxx,12,.1717  
mp,kyy,12,.1744  
mat,12  
amesh,12  
amesh,24

mp,kxx,13,.1674  
mp,kyy,13,.1722  
mat,13  
amesh,13  
amesh,25

mp,kxx,14,.1772  
mp,kyy,14,.1777  
mat,14  
amesh,14  
amesh,26

mp,kxx,15,.1712  
mp,kyy,15,.1741  
mat,15  
amesh,15  
amesh,27

mp,kxx,16,.1771  
mp,kyy,16,.1776  
mat,16  
amesh,16  
amesh,28

mp,kxx,17,.1671  
mp,kyy,17,.1721  
mat,17  
amesh,17  
amesh,29

mp,kxx,18,.1315  
mp,kyy,18,.1566  
mat,18  
amesh,18  
amesh,30

!!Boundary to collet  
mp,kxx,19,1  
mat,19  
amesh,19

!apply loads and IC

!set initial conditions  
nset,all  
ic,all,temp,25

!Edge cylinder convection  
!5,25,27 adiabatic  
lset,all  
lset,s,line,,2,2,1  
lset,a,line,,6,6,1  
lset,a,line,,11,11,1  
lset,a,line,,28,28,1  
lset,a,line,,32,32,1  
lset,a,line,,35,35,1  
lset,a,line,,15,15,1

```
lsel,a,line,,16,16,1
sfl,all,conv,%CONEDGE%,,25
```

```
!Flat plate convection
```

```
lsel,all
lsel,s,line,,5,5,1
lsel,a,line,,10,10,1
lsel,a,line,,27,27,1
lsel,a,line,,33,33,1
lsel,a,line,,31,31,1
lsel,a,line,,34,34,1
lsel,a,line,,30,30,1
lsel,a,line,,14,14,1
lsel,a,line,,25,25,1
lsel,a,line,,47,47,1
sfl,all,conv,%CONFACE%,,25
lsel,all
```

```
!HGEN_CF_HiINT_MLI_2900
```

```
!asel,s,,,1,1,1
!asel,a,,,9,18,1
```

```
asel,s,,,1,1,1
!BFA,all,hgen,2762500
!lsel,all
asel,a,,,9,18,1
asel,a,,,20,30,1
BFA,all,hgen,%hgen%
asel,all
```

```
!!Solve current LS
```

```
/solu
solve
```

```
!General Post Processor
```

```
/post1
```

```
/graphics,full
/triad,off
/plopts,leg1,0
/plopts,date,0
/plopts,minm,0
/plopts,frame,0
/udoc,1,cntr,left
```

```
/plopts,minm,0
/contour,all,8,25,25,225
```

```
plnsol,temp
```

## 2-D Model Temperature Predictions within the Copper Rod FOB

```
abbres,new,mybuttons_INF
```

```
/prep7
```

```
*DIM,HGEN, TABLE,374,101,1,x,y,,
*TREAD,HGEN,'C:\Documents and
Settings\mcheadle.000\Desktop\ANSYS\Tables\OnSunHGEN','txt', , ,
```

```
*DIM,CONFACE, TABLE,2000,1,1,TEMP,,
*TREAD,CONFACE,'C:\Documents and
Settings\mcheadle.000\Desktop\ANSYS\Tables\hFace','txt', , ,
```

```
*DIM,CONEDGE, TABLE,2000,1,1,TEMP,,
*TREAD,CONEDGE,'C:\Documents and
Settings\mcheadle.000\Desktop\ANSYS\Tables\hEdge','txt', , ,
```

```
!csys,5
et,1,plane77
keyopt,1,3,1
```

```
!define FOB perimeter
k,1,0,0.50402,0
k,2,0.0166,0.50402,0
k,3,0.0185547,0.20402,0
k,4,0,0.20402,0
k,5,.0185547,0.28403,0
k,30,0.001509,0.50402,0!!!!!!!!!!!!!!!!!!!!!!!!!!!!!!
k,51,0.0166,0.20402,0
k,40,0.0166,0.28403,0
```

```
l,1,30
l,2,40
l,5,3
l,3,51
```

```
!define collet perimeter
k,6,0.037973,0.28403,0
```

k,7,0.037973,0.27133,0  
k,8,0.0231267,0.27133,0  
k,9,0.0231267,0.20402,0

l,5,6  
l,6,7  
l,7,8  
l,8,9  
l,9,3

!define sleeve perimeter  
k,10,0.055753,0.27133,0  
k,11,0.055753,0.25863,0  
k,12,0.037973,0.25863,0  
k,13,0.037973,0.19132,0  
k,14,0.026162,0.19132,0  
k,15,0.026162,0.06559,0  
k,16,0.018554700,0.047175,0  
k,17,0.018554700,0.05289,0  
k,18,0.02032,0.06559,0  
k,19,0.02032,0.20148,0  
k,20,0.018554700,0.20148,0

l,7,10  
l,10,11  
l,11,12  
l,12,13  
l,13,14  
l,14,15  
l,15,16  
l,16,17  
l,17,18  
l,18,19  
l,19,20  
l,20,3

!define PMMA perimeter  
k,21,0,0.05289,0

l,20,17  
l,17,21  
l,21,4

!define Glass cover perimeter  
k,22,0,0.047175,0

l,16,22  
l,22,21

!define Collar perimeter  
k,23,0.15875,0.25863,0  
k,24,0.15875,0.19132,0  
k,25,0.13875,0.19132,0

l,11,23  
l,23,24  
l,24,25  
l,25,13

!define dish perimeter  
k,26,.58875,0.003,0  
larc,24,26,16,1.118915

k,27,.58875,0.0,0  
l,26,27

k,28,0.15875,0.18832,0  
larc,27,28,16,1.118915

k,29,0.13875,0.18832,0  
l,28,29  
l,29,25

!define edge

l,40,51

!define FOB Guts!!

k,31,0.003018,0.50402,0  
k,32,0.004527,0.50402,0  
k,33,0.006036,0.50402,0  
k,34,0.007545,0.50402,0  
k,35,0.009055,0.50402,0  
k,36,0.01056,0.50402,0  
k,37,0.01207,0.50402,0  
k,38,0.01358,0.50402,0  
k,39,0.01509,0.50402,0

k,41,0.001509,0.20402,0  
k,42,0.003018,0.20402,0

k,43,0.004527,0.20402,0  
k,44,0.006036,0.20402,0  
k,45,0.007545,0.20402,0  
k,46,0.009055,0.20402,0  
k,47,0.01056,0.20402,0  
k,48,0.01207,0.20402,0  
k,49,0.01358,0.20402,0  
k,50,0.01509,0.20402,0

1,30,31  
1,31,32  
1,32,33  
1,33,34  
1,34,35  
1,35,36  
1,36,37  
1,37,38  
1,38,39  
1,39,2  
1,40,5

1,51,50  
1,50,49  
1,49,48  
1,48,47  
1,47,46  
1,46,45  
1,45,44  
1,44,43  
1,43,42  
1,42,41  
1,41,4

k,52,0,.28403,0  
k,53,0.001509,0.28403,0  
k,54,0.003018,0.28403,0  
k,55,0.004527,0.28403,0  
k,56,0.006036,0.28403,0  
k,57,0.007545,0.28403,0  
k,58,0.009055,0.28403,0  
k,59,0.01056,0.28403,0  
k,60,0.01207,0.28403,0  
k,61,0.01358,0.28403,0  
k,62,0.01509,0.28403,0

1,4,52

1,52,1

1,52,53

1,53,54

1,54,55

1,55,56

1,56,57

1,57,58

1,58,59

1,59,60

1,60,61

1,61,62

1,62,40

1,30,53

1,31,54

1,32,55

1,33,56

1,34,57

1,35,58

1,36,59

1,37,60

1,38,61

1,39,62

1,53,41

1,54,42

1,55,43

1,56,44

1,57,45

1,58,46

1,59,47

1,60,48

1,61,49

1,62,50

!define areas

!FOB

al,61,59,58,82

!collet

al,3,5,6,7,8,9

!sleeve

lsl,s,,7,21,1

al,all,11

lsl,all

!PMMA rod  
lsel,s,,48,58,1  
lsel,a,,4,4,1  
lsel,a,,21,24,1  
al,all,48  
lsel,all  
!Glass cover  
al,23,17,25,26  
!Air gap  
al,19,18,22,20  
!Collar  
al,12,27,28,29,30,13  
!dish  
al,29,31,32,33,34,35  
!FOB Slices  
al,62,57,83,82  
al,63,56,84,83  
al,64,55,85,84  
al,65,54,86,85  
al,66,53,87,86  
al,67,52,88,87  
al,68,51,89,88  
al,69,50,90,89  
al,70,49,91,90  
al,71,48,36,91  
  
!edge  
al,47,3,4,36  
  
!FOB tail  
al,61,60,72,1  
al,62,72,73,37  
al,63,73,74,38  
al,64,74,75,39  
al,65,75,76,40  
al,66,76,77,41  
al,67,77,78,42  
al,68,78,79,43  
al,69,79,80,44  
al,70,80,81,45  
al,71,81,2,46  
  
!collet props  
esize,.0016  
mp,kxx,2,237  
mat,2

amesh,2

!sleeve props  
mp,kxx,3,237  
mat,3  
amesh,3

!PMMA props  
mp,kxx,4,.18  
mat,4  
amesh,4

!glass props  
mp,kxx,5,1.4  
amesh,5

!air props  
mp,kxx,6,.027  
mat,6  
amesh,6

!collar props  
mp,kxx,7,237  
mat,7  
amesh,7

!dish props  
mp,kxx,8,.18  
mat,8  
amesh,8

!FOB props  
!esize,.0005  
mp,kxx,1,.1707  
mp,kyy,1,.1739  
mat,1  
amesh,1  
amesh,20

!FOB Slices  
mp,kxx,9,.1706  
mp,kyy,9,.1738  
mat,9  
amesh,9  
amesh,21

mp,kxx,10,.1664  
mp,kyy,10,.1718  
mat,10  
amesh,10  
amesh,22

mp,kxx,11,.1725  
mp,kyy,11,.1748  
mat,11  
amesh,11  
amesh,23

mp,kxx,12,.1717  
mp,kyy,12,.1744  
mat,12  
amesh,12  
amesh,24

mp,kxx,13,.1674  
mp,kyy,13,.1722  
mat,13  
amesh,13  
amesh,25

mp,kxx,14,.1772  
mp,kyy,14,.1777  
mat,14  
amesh,14  
amesh,26

mp,kxx,15,.1712  
mp,kyy,15,.1741  
mat,15  
amesh,15  
amesh,27

mp,kxx,16,.1771  
mp,kyy,16,.1776  
mat,16  
amesh,16  
amesh,28

mp,kxx,17,.1671  
mp,kyy,17,.1721  
mat,17  
amesh,17

amesh,29

mp,kxx,18,.1315

mp,kyy,18,.1566

mat,18

amesh,18

amesh,30

!!Boundary to collet

mp,kxx,19,1

mat,19

amesh,19

!apply loads and IC

!set initial conditions

nset,all

ic,all,temp,25

!Edge cylinder convection

!5,25,27 adiabatic

lsel,all

lsel,s,line,,2,2,1

lsel,a,line,,6,6,1

lsel,a,line,,11,11,1

lsel,a,line,,28,28,1

lsel,a,line,,32,32,1

lsel,a,line,,35,35,1

lsel,a,line,,15,15,1

lsel,a,line,,16,16,1

sfl,all,conv,%CONEDGE%,,25

!Flat plate convection

lsel,all

lsel,s,line,,5,5,1

lsel,a,line,,10,10,1

lsel,a,line,,27,27,1

lsel,a,line,,33,33,1

lsel,a,line,,31,31,1

lsel,a,line,,34,34,1

lsel,a,line,,30,30,1

lsel,a,line,,14,14,1

lsel,a,line,,25,25,1

lsel,a,line,,47,47,1

sfl,all,conv,%CONFACE%,,25

lsel,all

```
!HGEN_CF_HiINT_MLI_2900
```

```
!asel,s,,1,1,1
```

```
!asel,a,,9,18,1
```

```
asel,s,,1,1,1
```

```
!BFA,all,hgen,2762500
```

```
!lsel,all
```

```
asel,a,,9,18,1
```

```
asel,a,,20,30,1
```

```
BFA,all,hgen,%hgen%
```

```
asel,all
```

```
!!Solve current LS
```

```
/solu
```

```
solve
```

```
!General Post Processor
```

```
/post1
```

```
/graphics,full
```

```
/triad,off
```

```
/plopts,leg1,0
```

```
/plopts,date,0
```

```
/plopts,minm,0
```

```
/plopts,frame,0
```

```
/udoc,1,cntr,left
```

```
/plopts,minm,0
```

```
/contour,all,8,25,25,225
```

```
plnsol,temp
```

## **2-D Model Temperature Predictions within the Aluminum Filled FOB**

```
abbres,new,mybuttons_INF
```

```
/prep7
```

```
*DIM,HGEN,TABLE,374,101,1,x,y,,
```

```
*TREAD,HGEN,'C:\Documents and
```

```
Settings\mcheadle.000\Desktop\ANSYS\Tables\OnSunHGENPores','txt', , ,
```

```
*DIM,HFLUX,TABLE,374,1,1,x,y,,
*TREAD,HFLUX,'C:\Documents and
Settings\mcheadle.000\Desktop\ANSYS\Tables\OnSunHFLUX','txt', , ,
```

```
*DIM,CONFACE,TABLE,2000,1,1,TEMP,,,
*TREAD,CONFACE,'C:\Documents and
Settings\mcheadle.000\Desktop\ANSYS\Tables\hFace','txt', , ,
```

```
*DIM,CONEDGE,TABLE,2000,1,1,TEMP,,,
*TREAD,CONEDGE,'C:\Documents and
Settings\mcheadle.000\Desktop\ANSYS\Tables\hEdge','txt', , ,
```

```
!csys,5
et,1,plane77
keyopt,1,3,1
```

```
!define FOB perimeter
k,1,0,0.50402,0
k,2,0.0166,0.50402,0
k,3,0.0185547,0.20402,0
k,4,0,0.20402,0
k,5,.0185547,0.28403,0
k,30,0.001509,0.50402,0!!!!!!!!!!!!!!!!!!!!!!!!!!!!!!
k,51,0.0166,0.20402,0
k,40,0.0166,0.28403,0
```

```
l,1,30
l,2,40
l,5,3
l,3,51
```

```
!define collet perimeter
k,6,0.037973,0.28403,0
k,7,0.037973,0.27133,0
k,8,0.0231267,0.27133,0
k,9,0.0231267,0.20402,0
```

```
l,5,6
l,6,7
l,7,8
l,8,9
l,9,3
```

```
!define sleeve preimeter
k,10,0.055753,0.27133,0
k,11,0.055753,0.25863,0
```

k,12,0.037973,0.25863,0  
k,13,0.037973,0.19132,0  
k,14,0.026162,0.19132,0  
k,15,0.026162,0.06559,0  
k,16,0.018554700,0.047175,0  
k,17,0.018554700,0.05289,0  
k,18,0.02032,0.06559,0  
k,19,0.02032,0.20148,0  
k,20,0.018554700,0.20148,0

l,7,10  
l,10,11  
l,11,12  
l,12,13  
l,13,14  
l,14,15  
l,15,16  
l,16,17  
l,17,18  
l,18,19  
l,19,20  
l,20,3

!define PMMA perimeter  
k,21,0,0.05289,0

l,20,17  
l,17,21  
l,21,4

!define Glass cover perimeter  
k,22,0,0.047175,0

l,16,22  
l,22,21

!define Collar perimeter  
k,23,0.15875,0.25863,0  
k,24,0.15875,0.19132,0  
k,25,0.13875,0.19132,0

l,11,23  
l,23,24  
l,24,25  
l,25,13

```
!define dish perimeter
k,26,.58875,0.003,0
larc,24,26,16,1.118915
```

```
k,27,.58875,0.0,0
l,26,27
```

```
k,28,0.15875,0.18832,0
larc,27,28,16,1.118915
```

```
k,29,0.13875,0.18832,0
l,28,29
l,29,25
```

```
!define edge
```

```
l,40,51
```

```
!define FOB Guts!!!!!!!!!!!!!!!!!!!!!!!!!!!!!!!!!!!!!!!!!!!!!!
```

```
k,31,0.003018,0.50402,0
k,32,0.004527,0.50402,0
k,33,0.006036,0.50402,0
k,34,0.007545,0.50402,0
k,35,0.009055,0.50402,0
k,36,0.01056,0.50402,0
k,37,0.01207,0.50402,0
k,38,0.01358,0.50402,0
k,39,0.01509,0.50402,0
```

```
k,41,0.001509,0.20402,0
k,42,0.003018,0.20402,0
k,43,0.004527,0.20402,0
k,44,0.006036,0.20402,0
k,45,0.007545,0.20402,0
k,46,0.009055,0.20402,0
k,47,0.01056,0.20402,0
k,48,0.01207,0.20402,0
k,49,0.01358,0.20402,0
k,50,0.01509,0.20402,0
```

```
l,30,31
l,31,32
l,32,33
l,33,34
```

1,34,35  
1,35,36  
1,36,37  
1,37,38  
1,38,39  
1,39,2  
1,40,5

1,51,50  
1,50,49  
1,49,48  
1,48,47  
1,47,46  
1,46,45  
1,45,44  
1,44,43  
1,43,42  
1,42,41  
1,41,4

k,52,0,.28403,0  
k,53,0.001509,0.28403,0  
k,54,0.003018,0.28403,0  
k,55,0.004527,0.28403,0  
k,56,0.006036,0.28403,0  
k,57,0.007545,0.28403,0  
k,58,0.009055,0.28403,0  
k,59,0.01056,0.28403,0  
k,60,0.01207,0.28403,0  
k,61,0.01358,0.28403,0  
k,62,0.01509,0.28403,0

1,4,52  
1,52,1

1,52,53  
1,53,54  
1,54,55  
1,55,56  
1,56,57  
1,57,58  
1,58,59  
1,59,60  
1,60,61  
1,61,62  
1,62,40

1,30,53  
1,31,54  
1,32,55  
1,33,56  
1,34,57  
1,35,58  
1,36,59  
1,37,60  
1,38,61  
1,39,62

1,53,41  
1,54,42  
1,55,43  
1,56,44  
1,57,45  
1,58,46  
1,59,47  
1,60,48  
1,61,49  
1,62,50

!define areas  
!FOB  
al,61,59,58,82  
!collet  
al,3,5,6,7,8,9  
!sleeve  
lsl,s,,7,21,1  
al,all,11  
lsl,all  
!PMMA rod  
lsl,s,,48,58,1  
lsl,a,,4,4,1  
lsl,a,,21,24,1  
al,all,48  
lsl,all  
!Glass cover  
al,23,17,25,26  
!Air gap  
al,19,18,22,20  
!Collar  
al,12,27,28,29,30,13  
!dish

al,29,31,32,33,34,35

!FOB Slices

al,62,57,83,82

al,63,56,84,83

al,64,55,85,84

al,65,54,86,85

al,66,53,87,86

al,67,52,88,87

al,68,51,89,88

al,69,50,90,89

al,70,49,91,90

al,71,48,36,91

!edge

al,47,3,4,36

!FOB tail

al,61,60,72,1

al,62,72,73,37

al,63,73,74,38

al,64,74,75,39

al,65,75,76,40

al,66,76,77,41

al,67,77,78,42

al,68,78,79,43

al,69,79,80,44

al,70,80,81,45

al,71,81,2,46

!glass props

esize,.003

mp,kxx,5,1.4

amesh,5

!air props

esize,.003

mp,kxx,6,.027

mat,6

amesh,6

!dish props

esize,.003

mp,kxx,8,.18

mat,8

amesh,8

!FOB props  
esize,.0006  
mp,kxx,20,.1982  
mp,kyy,20,12.15  
mat,20  
amesh,1

esize,.0012  
mp,kxx,1,.1707  
mp,kyy,1,.1739  
mat,1  
amesh,20

!FOB Slices  
esize,.0006  
mp,kxx,21,.1982  
mp,kyy,21,12.18  
mat,21  
amesh,9

esize,.0012  
mp,kxx,9,.1706  
mp,kyy,9,.1738  
mat,9  
amesh,21

esize,.0006  
mp,kxx,22,.2013  
mp,kyy,22,15.32  
mat,22  
amesh,10

esize,.0012  
mp,kxx,10,.1664  
mp,kyy,10,.1718  
mat,10  
amesh,22

esize,.0006  
mp,kxx,23,.1967  
mp,kyy,23,10.68  
mat,23  
amesh,11

esize,.0012  
mp,kxx,11,.1725

mp,kyy,11,.1748  
mat,11  
amesh,23

esize,.0006  
mp,kxx,24,.1974  
mp,kyy,24,11.31  
mat,24  
amesh,12

esize,.0012  
mp,kxx,12,.1717  
mp,kyy,12,.1744  
mat,12  
amesh,24

esize,.0006  
mp,kxx,25,.2007  
mp,kyy,25,14.65  
mat,25  
amesh,13

esize,.0012  
mp,kxx,13,.1674  
mp,kyy,13,.1722  
mat,13  
amesh,25

esize,.0006  
mp,kxx,26,.1925  
mp,kyy,26,6.263  
mat,26  
amesh,14

esize,.0012  
mp,kxx,14,.1772  
mp,kyy,14,.1777  
mat,14  
amesh,26

esize,.0006  
mp,kxx,27,.1978  
mp,kyy,27,11.73  
mat,27  
amesh,15

esize,.0012  
mp,kxx,15,.1712  
mp,kyy,15,.1741  
mat,15  
amesh,27

esize,.0006  
mp,kxx,28,.1927  
mp,kyy,28,6.394  
mat,28  
amesh,16

esize,.0012  
mp,kxx,16,.1771  
mp,kyy,16,.1776  
mat,16  
amesh,28

esize,.0006  
mp,kxx,29,.2009  
mp,kyy,29,14.84  
mat,29  
amesh,17

esize,.0012  
mp,kxx,17,.1671  
mp,kyy,17,.1721  
mat,17  
amesh,29

esize,.0006  
mp,kxx,30,.2282  
mp,kyy,30,38.59  
mat,30  
amesh,18

esize,.0012  
mp,kxx,18,.1315  
mp,kyy,18,.1566  
mat,18  
amesh,30

!!Boundary to collet  
esize,.0006  
mp,kxx,19,1  
mat,19

amesh,19

!sleeve props  
esize,.003  
mp,kxx,3,237  
mat,3  
amesh,3

!collet props  
esize,.003  
mp,kxx,2,237  
mat,2  
amesh,2

!PMMA props  
esize,.003  
mp,kxx,4,.18  
mat,4  
amesh,4

!collar props  
esize,.005  
mp,kxx,7,237  
mat,7  
amesh,7

!apply loads and IC

!set initial conditions  
nset,all  
ic,all,temp,25

!Edge cylinder convection  
!,, adiabatic  
lset,all  
lset,s,line,,2,2,1  
lset,a,line,,6,6,1  
lset,a,line,,11,11,1  
lset,a,line,,28,28,1  
lset,a,line,,32,32,1  
lset,a,line,,35,35,1  
lset,a,line,,15,15,1  
lset,a,line,,16,16,1  
sfl,all,conv,%CONEDGE%,,25

!Flat plate convection

```
lsel,all
lsel,s,line,,5,5,1
lsel,a,line,,10,10,1
lsel,a,line,,27,27,1
lsel,a,line,,33,33,1
lsel,a,line,,31,31,1
lsel,a,line,,34,34,1
lsel,a,line,,30,30,1
lsel,a,line,,14,14,1
lsel,a,line,,25,25,1
lsel,a,line,,47,47,1
sfl,all,conv,%CONFACE%,,25
lsel,all

!HGEN_CF_HiINT_MLI_2900
lsel,s,line,,48,58,1
sfl,all,hflux,%HFLUX%
lsel,all

asel,s,,,1,1,1
asel,a,,,9,18,1
asel,a,,,20,30,1
BFA,all,hgen,%hgen%
asel,all

!Solve current LS

/solu
solve

!General Post Processor

/post1

/graphics,full
/triad,off
/plopts,leg1,0
/plopts,date,0
/plopts,minm,0
/plopts,frame,0
/udoc,1,cntr,left
/plopts,minm,0
/contour,all,8,25,25

plnsol,temp
```